Spectral Flow Cytometry:
Expanding Your Research Spectrum

Article Collection

WILEY

CURRENT PROTOCOLS
A Wiley Brand

Cytometry PART A
ISAC
Journal of Quantitative Cell Science

Sponsored by:
ThermoFisher SCIENTIFIC
The world leader in serving science

The Bigfoot Spectral Cell Sorter

Get reproducible results up to 100x faster

The cutting-edge Invitrogen™ Bigfoot Spectral Cell Sorter is now part of the product family at Thermo Fisher Scientific and is designed for high performance, flexibility, safety, and scalability to meet laboratory needs—today and in the future.

- **Rapid**—higher throughput
- **High parameter**—spectral unmixing for up to 60 colors
- **Safety**—biocontainment is built in
- **Ease of use**—Sasquatch Software allows for rapid adoption

Learn more at **thermofisher.com/spectral**

invitrogen

Contents

Introduction

BY JEREMY PETRAVICZ, PH.D., EDITOR, *CURRENT PROTOCOLS*

Flow cytometry analysis is one of the foundational technologies in phenotyping of cell types, particularly in the field of immunology and oncology. Conventional flow cytometry relies on clear delineation between the emission spectra of fluorochromes to maximize the resolution of labelled cells to segment them into identified populations. This requirement for clear separation of spectra however imposes constraints on panel design that can limit the number of cell types that can be identified in single flow cytometry session.

To overcome this barrier, technology and reagents that allow for the collection and analysis of the full spectral emission of a fluorescent molecule have been developed. Termed spectral flow cytometry, this advancement allows for increased flexibility and resolution in flow cytometry panel design. In conventional flow cytometry, dichroic mirrors and band-pass filters allow wavelengths of light to pass through to the photomultiplier tubes for detection. This configuration can also be employed for spectral flow cytometry, with the addition of an expanded range of detectors to fully capture the spectrum of reflected and/or emitted light. By detecting the full spectrum of emitted light and with the use of computational methods to "unmix" the spectra of fluorophores with similar excitation range (for example two different, red-shifted dyes), this greatly increase the range of fluorophores that can be incorporated into panel design. The expanded set of markers allows for finer resolution of cell populations in a single flow cytometry assay, and increased ability to recognize and separate hard-to-identify cell populations in a mixed sample.

In this article collection, we will introduce the underlying concepts and present examples of panels developed for spectral flow cytometry. The research article collection opens with Ferrer-Font et al. (2020) which provides an overview of panel design protocols for spectral flow cytometry. While similar in many ways to conventional flow cytometry, spectral flow requires certain considerations as to the biological question being addressed and the hardware parameters of the machine (such as the Thermo Fisher Scientific Bigfoot™). The research article collection then highlights spectral flow cytometry panels designed for applications ranging from immune cell monitoring to drug discovery for ion channels.

Jensen and Wnek (2020) details the design and validation of a 25 biomarker panel for monitoring immune cells over time from human blood samples. This article illustrates the power of spectral flow cytometry for resolving high-parameter assays with high precision and reproducibility across replicates, making it suitable for translational research. Next Solomon et al. (2020) describes the design and use of a 15-fluorochrome panel for the phenotyping of hematopoietic stem and progenitor cells. The panel design incorporates several previously separate characterization paradigms into one assay to elucidate the progression of hematopoietic stem and progenitor cells into mature cell types. The precision and resolution of spectral flow cytometry enabled a deep phenotyping of the hematopoietic compartment at a level not achievable before. Lastly, Barczyk et al. (2020) details the development of P2X purinergic receptor 7 (P2XR7) activity assays using three different modes of flow cytometry (conventional, imaging, and spectral) for the purpose of screening channel modulators. The authors used spectral flow to distinguish individual measurement of P2XR7 activity by allowing separation of overlapping fluorescent dyes and autofluorescent compounds, leading to increased accuracy in their assay. Spectral flow cytometry screening panels open the ability to accurately measure the potency of novel compounds (even if they exhibit autofluorescence) using multiple readouts simultaneously.

Through the concepts and applications presented in this research article collection we hope to educate scientists on how spectral flow cytometry can empower their research and open new avenues of exploration. For more information regarding spectral flow cytometry, we encourage you to visit the Thermo Fisher Scientific Spectral Flow Cytometry Learning Center and explore the possibilities presented there for your research.

References

Ferrer-Font, L., Small, S. J., Lewer, B., Pilkington, K. R., Johnston, L. K., Park, L. M., Lannigan, J., Jaimes, M. C., & Price, K. M. (2021). Panel optimization for high-dimensional immunophenotyping assays using full-spectrum flow cytometry. *Current Protocols,* 1, e222. https://doi.org/10.1002/cpz1.222

Jensen, HA, Wnek, R. Analytical performance of a 25-marker spectral cytometry immune monitoring assay in peripheral blood. Cytometry. 2021; 99: 180– 193. https://doi.org/10.1002/cyto.a.24290

Solomon, M., DeLay, M. and Reynaud, D. (2020), Phenotypic Analysis of the Mouse Hematopoietic Hierarchy Using Spectral Cytometry: From Stem Cell Subsets to Early Progenitor Compartments. Cytometry, 97: 1057-1065. https://doi.org/10.1002/cyto.a.24041

Barczyk, A, Bauderlique-Le Roy, H, Jouy, N, et al. Flow cytometry: An accurate tool for screening P2RX7 modulators. Cytometry. 2021; 99: 793–806. https://doi.org/10.1002/cyto.a.24287

Panel Optimization for High-Dimensional Immunophenotyping Assays Using Full-Spectrum Flow Cytometry

Laura Ferrer-Font,[1,2,6,7] Sam J. Small,[1,6] Brittany Lewer,[1] Katherine R. Pilkington,[3] Laura K. Johnston,[4] Lily M. Park,[3] Joanne Lannigan,[5] Maria C. Jaimes,[3,6] and Kylie M. Price[1,6]

[1]Malaghan Institute of Medical Research, Wellington, New Zealand
[2]Maurice Wilkins Centre for Molecular Biodiscovery, Auckland, New Zealand
[3]Cytek Biosciences, Fremont, California
[4]University of Chicago, Chicago, Illinois
[5]Flow Cytometry Support Services, LLC, Alexandria, Virginia
[6]These authors contributed equally to this work.
[7]Corresponding author: *lferrer@malaghan.org.nz*

Technological advancements in fluorescence flow cytometry and an ever-expanding understanding of the complexity of the immune system have led to the development of large flow cytometry panels reaching up to 43 colors at the single-cell level. However, as panel size and complexity increase, so too does the detail involved in designing and optimizing successful high-quality panels fit for downstream high-dimensional data analysis. In contrast to conventional flow cytometers, full-spectrum flow cytometers measure the entire emission spectrum of each fluorophore across all lasers. This allows for fluorophores with very similar emission maxima but unique overall spectral fingerprints to be used in conjunction, enabling relatively straightforward design of larger panels. Although a protocol for best practices in full-spectrum flow cytometry panel design has been published, there is still a knowledge gap in going from the theoretically designed panel to the necessary steps required for panel optimization. Here, we aim to guide users through the theory of optimizing a high-dimensional full-spectrum flow cytometry panel for immunophenotyping using comprehensive step-by-step protocols. These protocols can also be used to troubleshoot panels when issues arise. A practical application of this approach is exemplified with a 24-color panel designed for identification of conventional T-cell subsets in human peripheral blood. © 2021 Malaghan Institute of Medical Research, Cytek Biosciences. Current Protocols published by Wiley Periodicals LLC.

Keywords: assay optimization and troubleshooting • full-spectrum flow cytometry • high-dimensional flow cytometry panel

CURRENT PROTOCOLS
A Wiley Brand

Current Protocols e222, Volume 1
Published in Wiley Online Library (wileyonlinelibrary.com).
doi: 10.1002/cpz1.222

How to cite this article:
Ferrer-Font, L., Small, S. J., Lewer, B., Pilkington, K. R., Johnston, L. K., Park, L. M., Lannigan, J., Jaimes, M. C., & Price, K. M. (2021). Panel optimization for high-dimensional immunophenotyping assays using full-spectrum flow cytometry. *Current Protocols*, *1*, e222. doi: 10.1002/cpz1.222

INTRODUCTION

Technological advancements in fluorescence flow cytometry and an ever-expanding understanding of the complexity of the immune system have led to the development of large panels reaching 40 fluorophores in the Optimized Multicolor Immunofluorescence Panel (OMIP; Park, Lannigan, & Jaimes, 2020) and 43 colors in a technical note (Sahir, Mateo, Steinhoff, & Siveen, 2020). In contrast to conventional flow cytometry, which primarily measures the peak emission of each fluorophore in a target detector, full-spectrum flow cytometry uses a larger number of detectors with narrow band-pass filters. This allows the entire emission spectrum for every fluorophore to be captured across all laser lines, creating a detailed signature of each fluorophore. This makes it possible to distinguish fluorophores with very similar emission maxima but unique overall spectral fingerprints, increasing the flexibility in fluorophore selection. This feature, coupled with an instrument designed to maximize the detection of emitted light and highly efficient avalanche photodiodes, provides improved detection efficiencies that translate to better detection limits and higher signal resolution (Feher et al., 2016). While these features, unique to full-spectrum flow cytometry, provide the high-quality signals and low noise needed for successful high-dimensional panels, many of the same panel design considerations from conventional flow cytometry still apply. Common characteristics, together with those specific to full-spectrum flow cytometry, have been previously described (Ferrer-Font, Pellefigues, et al., 2020; Park et al., 2020). Now that hardware limitations hindering the use of highly overlapping dyes have been overcome, the main limitations for successful large panel design are the spillover-spreading error inherent to the use of fluorescence and the number of fluorophores available with unique spectral signatures. Many companies have recently begun developing spectrally distinct fluorophores, thus advancing the number of markers available to be analyzed in a single experiment.

Increasing the number of markers in a panel consequently increases the probability of compromising the resolution of the markers and populations of interest. The theoretical approach to panel design aims to avoid issues would that prevent resolution of every marker in the panel; however, in practice it is challenging to perfectly predict the impact of co-expression, variations in marker expression levels, and the performance of each specific reagent. Furthermore, it is difficult to anticipate the accuracy of reference controls for optimal unmixing results. For example, certain fluorophores emit slightly different spectra when bound to compensation beads or in the presence of different buffers.

One obstacle that has always impacted panel design and performance is the unique autofluorescence (AF) signatures of different sample and cell types. Cellular AF levels can vary depending on the type and metabolic state of cells (Mayeno, Hamann, & Gleich, 1992; Roederer, 2016; Shi et al., 2017) as well as sample preparation and staining procedures. This translates into different AF brightness levels and distinct spectral signatures in the samples being analyzed. Full-spectrum flow cytometry can resolve cellular AF signatures and ensure that they are not attributed to any of the fluorophores used. This can improve the signal-to-noise ratio and resolution of markers attached to fluorophores that emit closest to AF maxima (Ferrer-Font, Pellefigues, et al., 2020) in highly

autofluorescent tissues such as brain, lung, skin, intestine, and tumor (Schmutz, Valente, Cumano, & Novault, 2016). It is therefore highly recommended to characterize the AF spectrum of an unstained sample from the tissue or cell type of interest prior to panel design. This will provide useful information during fluorophore selection, ensuring that fluorophores are not allocated to areas of the spectrum where AF dominates.

STRATEGIC PLANNING

Once a high-dimensional full-spectrum flow cytometry panel has been optimally designed (Ferrer-Font, Pellefigues, et al., 2020), the step-by-step protocols presented here provide a series of practical steps for full and successful optimization. As outlined in Figure 1, the main procedures include evaluation of spectral reference controls (SRCs; see Basic Protocol 1), evaluation of unmixing of the fully stained (FS) sample (see Basic Protocol 2), evaluation of marker resolution (see Basic Protocol 3), and assessment of data quality (see Basic Protocol 4). Before any of these methods are performed, it is essential to titrate the antibodies used as well as any viability dye used. This is described in Support Protocol 1. An additional protocol describes changes that can be made to the instrument settings (see Support Protocol 2). Methods for evaluating and mitigating autofluorescence are included in Basic Protocol 3 and Support Protocol 3. Together, these protocols can also be used when troubleshooting a panel to identify sources of problems and provide insights into fixing them.

A 24-color panel optimization for identification of conventional T-cell subsets in human peripheral blood is provided to illustrate these procedures. The protocols were developed using the five-laser (5L) Cytek Aurora (Cytek Biosciences), but should be adaptable to any spectral flow cytometer. The protocols were designed for new full-spectrum flow cytometry users. Once familiarity and experience with specific tissue types is achieved, it is possible to modify the steps and order of the protocols to reduce the overall time

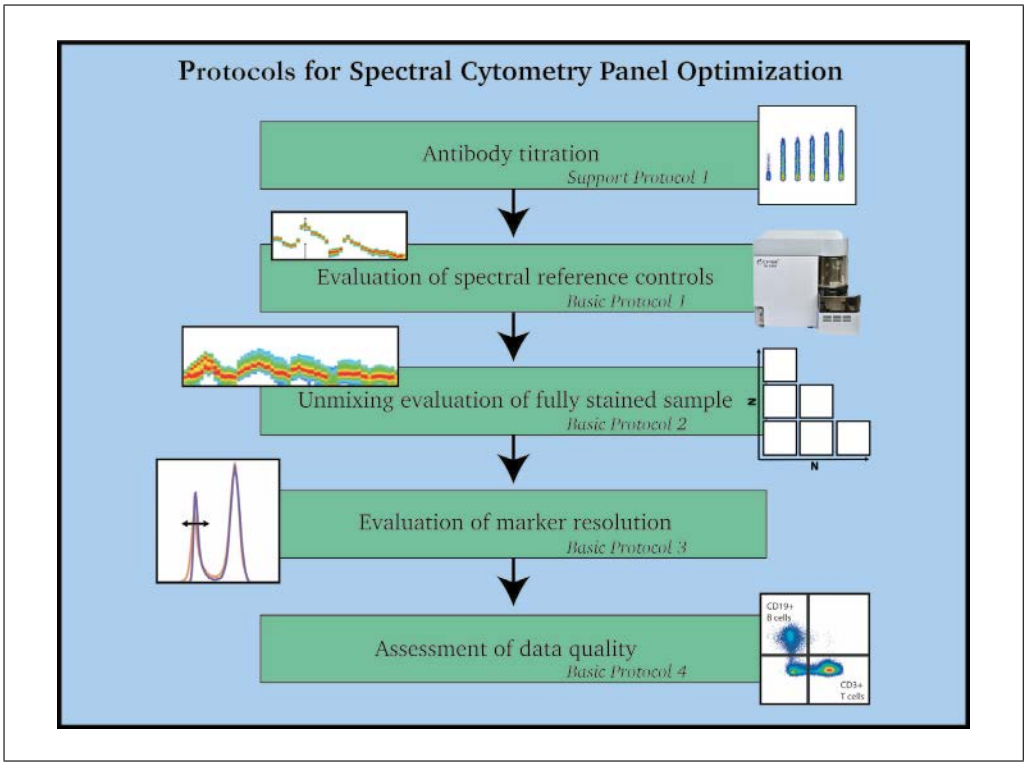

Figure 1 Overview of protocols for successful optimization of a high-dimensional spectral flow cytometry panel.

spent evaluating the panel. If a modified approach is taken, it is recommended that all the overall goals of the protocols (as outlined in Fig. 1) still be carried out.

BASIC PROTOCOL 1

PREPARATION AND EVALUATION OF OPTIMAL SPECTRAL REFERENCE CONTROLS

This protocol is divided in two sections. The first is for preparation of SRCs and ensures generation of the high-quality controls required for accurate unmixing. The steps describe the staining of polystyrene compensation beads and cryopreserved PBMCs with surface-labeling antibodies. They can be adapted for other tissues or staining procedures such as intracellular staining. It is important to mention that the preparation procedure will also guide users to prepare a fully stained (FS) sample and fluorescence minus one (FMO) controls as the protocols are very similar; these will be used later for evaluating the unmixing of the FS sample (see Basic Protocol 2). If preferred, FS and FMO samples can be stained separately, but treatment of samples should be kept identical. Importantly, to successfully complete this protocol, SS and FS cells should also be treated the same (antibody concentration, incubation time/temperature, fixed/unfixed, etc.).

The second section of the protocol is for evaluation. This aims first to check the quality of the acquired SRCs and then to evaluate whether there are any spectral mismatches between beads and cells for each fluorophore, which is accomplished by assessing how well the beads unmix the cells using N $\times$ N plots for all markers. Unmixing accuracy must be assessed on the actual sample (cells) to be used in the assay. In some cases beads will be acceptable as SRCs and in other cases it may be necessary to use cells. When this protocol is completed, the optimum SRCs (cells or beads) will be determined for future unmixing. If desired, well-characterized and high-quality controls can be stored for future use.

Materials

Cryopreserved PBMCs
Phosphate-buffered saline (PBS; Gibco, cat. no. 14190-250)
Fetal bovine serum (FBS; Gibco, cat. no. 10091-148)
Polystyrene compensation beads (e.g., UltraComp eBeads, Life Technologies, cat. no. 01-222-42)
FACS staining buffer: PBS with 2% bovine serum albumin (BSA; MP Biochemicals, CAS no. 9048-46-8) and 0.2% sodium azide (Sigma-Aldrich, cat. no. S8032)
Zombie NIR Fixable Viability Kit (BioLegend, cat. no. 423106)
Human TruStain FcX (Fc Receptor Blocking Solution; BioLegend, cat. no. 422301)
Antibodies (see Table 1 for list; see Support Protocol 1 for titration)
Brilliant Stain Buffer Plus (BD Biosciences, cat. no. 566385)

37°C water bath (e.g., Julabo Ecotemp TW12)
Hemocytometer (e.g., Hawksley Counting Chamber) and coverslips
96-well U-bottom plate (In Vitro Technologies, cat. no. 353077)
Filters with 0.65-μm or smaller pore size (*optional*)
Spectral cytometer (e.g., Cytek Aurora)
5-ml polypropylene round-bottom flow tubes (In Vitro Technologies, cat. no. 352008)
Cytek SpectroFlo software
Data analysis software for analyzing FCS files (e.g., FlowJo or FCS Express)

Prepare and acquire samples

1. Thaw PBMCs quickly in a 37°C water bath and add to 5 ml PBS with 2% FBS.

Table 1 Antibodies Used in Example Spectral Flow Cytometry Panel

Fluorophore	Marker	Supplier	Clone	Catalog number	Concentration (mg/ml)
BUV395	HLA-DR	BD Biosciences	G46-6	564040	1
BUV496	CD3	BD Biosciences	UCHT1	612940	1
BUV563	CD27	BD Biosciences	M-T271	741336	1
BUV737	CD45RA	BD Biosciences	HI100	612846	1.25
BV421	CD28	BioLegend	CD28.2	302930	2
Pacific Blue	CRTH2 (CD294)	BioLegend	BM16	350130	8
BV480	CD127	BD Biosciences	HIL-7R-M21	566101	2
BV510	TCRgd	BioLegend	B1	331220	15
BV570	CD4	BioLegend	RPA-T4	300534	1
BV605	CCR4 (CD194)	BioLegend	L291H4	359418	0.6
BV650	CCR6 (CD196)	BD Biosciences	11A9	563922	1
BV785	CD45RO	BioLegend	UCHL1	304234	1
BB515	CD25	BD Biosciences	2A3	564467	8.3
AF488	CCR10	R&D Systems	314305	RDSFAB3478G 0100	0.13
AF532	CD8	Thermo Fisher Scientific	RPA-T8	58-0088-42	0.25
PerCP-Cy5.5	CCR7	BioLegend	G043H7	353220	4
PE	Hu CD1d tetramer	NIH Tetramer Core Facility	PBS-57 loaded		0.81
PE-CF594	PLZF	BD Biosciences	R17-809	565738	0.63
PE-Cy7	CTLA4	eBioscience (TFS)	14D3	25-1529-42	0.2
APC	Hu MR1 tetramer	NIH Tetramer Core Facility	5-OP-RU loaded		0.18
AF647	FoxP3	BioLegend	259D	320214	0.6
APC-Cy7	CXCR3 (CD183)	Biolegend	49801.111	353722	0.13
BV711	CD19	BD Biosciences	SJ25C1	563036	0.25

As the thawing procedure can be critical, we recommend user-specific optimizations to ensure high sample viability (>80%) (Disis, dela Rosa, Goodell, & Ling-Yu, 2006).

CAUTION: *Steps 1-2 should be performed in a biosafety hood.*

2. Centrifuge 5 min at 500 × *g*, room temperature, and carefully flick off the supernatant.
3. Resuspend cells in PBS with 2% FBS and count viable cells on a hemocytometer.
4. Centrifuge as before and carefully flick off the supernatant.

5. Resuspend cells in PBS with 2% FBS to a concentration of 5×10^6 viable cells/ml.

6. Distribute 100 µl suspension per well of a 96-well U-bottom plate, allocating one well per fluorophore in the panel and one well for an unstained sample.

   A FS sample and appropriate FMO controls can be added but are not required for assessing the SRCs at this point. They will be used for assessing unmixing in Basic Protocol 2.

   The number of cells required will differ by tissue type; for PBMCs, ~5×10^5 cells is sufficient.

7. Add one drop of vortexed compensation beads plus 150 µl FACs staining buffer to a second set of wells, allocating one well per fluorophore in the panel except the viability dye.

   Figure 2A shows a typical plate layout. At this stage, the plate should contain unstained and FS sample wells (fully stained beads are not needed) plus two wells per fluorophore in the panel: one with cells and the other with compensation beads (except for the live/dead reagent, which is typically only used on cells). FMO controls should also be included for fluorophores where marker expression is very low or where the positive population is dim and gate placement would be subjective.

8. Centrifuge plate 5 min at 500 × *g*, 4°C, and flick off the supernatant.

   It is recommended to centrifuge samples at 4°C to maintain high viability, but room temperature is acceptable if a refrigerated centrifuge is not available.

9. Prepare viability stain in PBS according to the titration result (see Support Protocol 1) and add 100 µl to the live/dead cell control and FS sample, if included. Resuspend remaining wells with 100 µl PBS. Incubate for 15-30 min at room temperature, protected from light.

10. Centrifuge as above and flick off the supernatant.

11. Block Fc receptors of the cell samples using 100 µl of 1:40 Fc block in FACS staining buffer. Add an equal volume of FACS staining buffer to the beads. Incubate for 10 min at 4°C.

    Fc block should not be used on compensation beads, as all antibody binding sites will become occupied.

12. Centrifuge as above and flick off the supernatant.

13. Remove aggregates from antibody stocks by centrifuging 5 min at 16,000-18,000 × *g*, 4°C (Aass et al., 2011; Ayers et al., 2011; van der Vlist, Nolte-'t Hoen, Stoorvogel, Arkesteijn, & Wauben, 2012) and/or by filtering using a pore size of 0.1-0.65 µm (Inglis et al., 2015).

14. Prepare SS, FS, and FMO control antibody mixes by diluting stocks in FACS staining buffer according to titration results (see Support Protocol 1). Be sure to pipette from the top of the liquid to avoid centrifuged aggregates.

    Prepare enough volume of each antibody mix that two samples can be stained from the same mix. This will reduce differences due to antibody preparation when comparing bead versus cell SRCs. Allow for pipetting errors by making excess antibody mix (e.g., n + 1). Additionally, when more than one Brilliant polymer dye is used at the same time (FS and FMOs), Brilliant Stain Buffer Plus (or equivalent) should be added per manufacturer's instructions to decrease interaction between the dyes. Do not add Brilliant Stain Buffer Plus to compensation beads, as it is known to alter the spectral profile of some beads (Ferrer-Font, Pellefigues, et al., 2020).

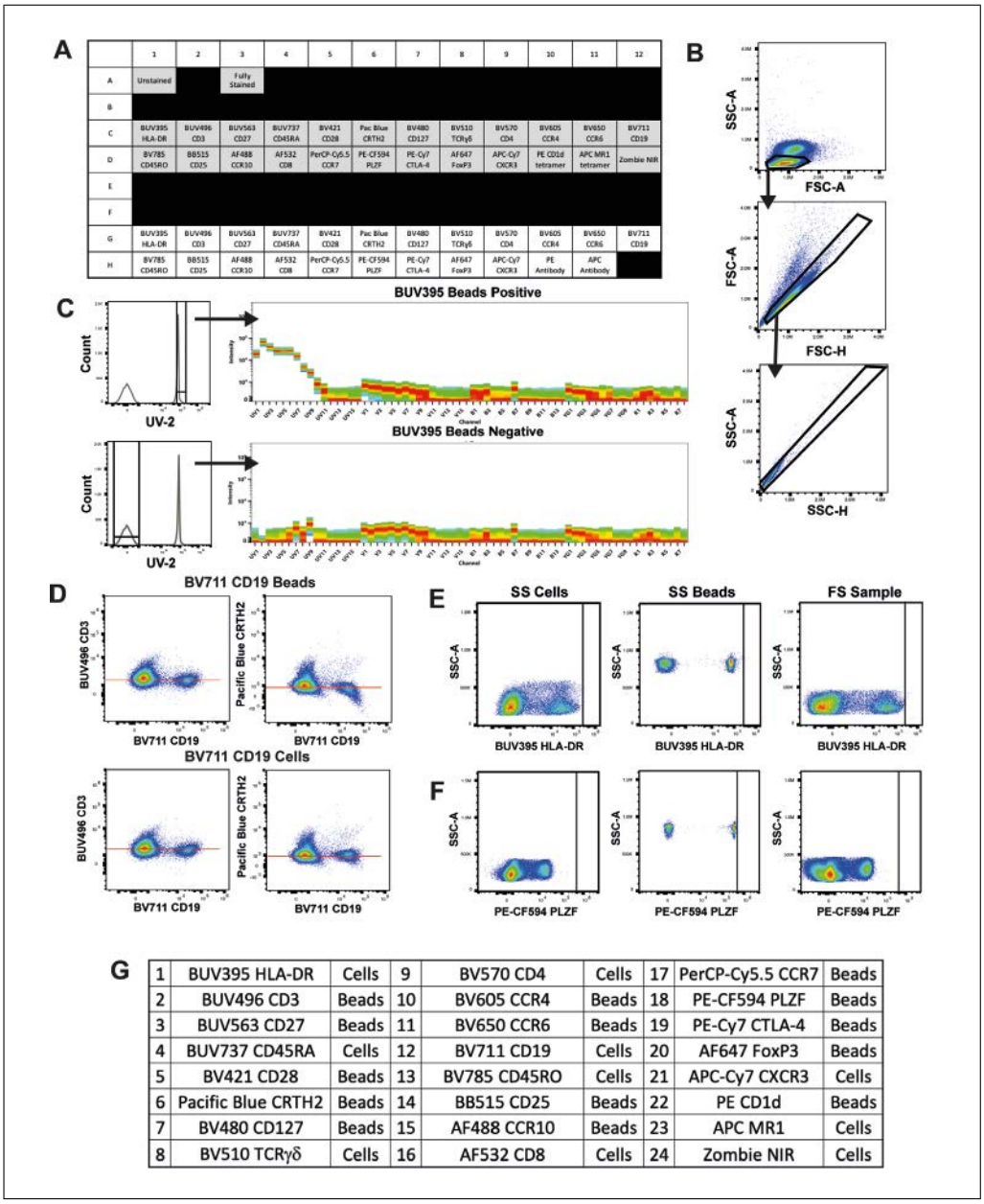

1	BUV395 HLA-DR	Cells	9	BV570 CD4	Cells	17	PerCP-Cy5.5 CCR7	Beads
2	BUV496 CD3	Beads	10	BV605 CCR4	Beads	18	PE-CF594 PLZF	Beads
3	BUV563 CD27	Beads	11	BV650 CCR6	Beads	19	PE-Cy7 CTLA-4	Beads
4	BUV737 CD45RA	Cells	12	BV711 CD19	Cells	20	AF647 FoxP3	Beads
5	BV421 CD28	Beads	13	BV785 CD45RO	Cells	21	APC-Cy7 CXCR3	Cells
6	Pacific Blue CRTH2	Beads	14	BB515 CD25	Beads	22	PE CD1d	Beads
7	BV480 CD127	Beads	15	AF488 CCR10	Beads	23	APC MR1	Cells
8	BV510 TCRγδ	Cells	16	AF532 CD8	Cells	24	Zombie NIR	Cells

Figure 2 Evaluation of SRCs and selection of optimal control type. (**A**) Example plate plan. Shaded wells contain cells and unshaded wells contain compensation beads. (**B**) Expert gating of cells of interest and doublet exclusion plots. A well-optimized ASF can be visualized in the second pseudoplot. (**C**) BUV395 bead SRC gating of positive and negative populations and spectral signatures of gated events showing clear positive and negative signals. (**D**) SS cells unmixed with either BV711 CD19-stained compensation beads (top) or cells (bottom). Unmixing of BV711 CD19 is incorrect against certain parameters (e.g., Pacific Blue CRTH2) but not others (e.g., BUV496 CD3) when beads are used. This error is corrected through unmixing with cells with no negative impact to the plot with previously correct unmixing. Red line indicates equal median fluorescence intensity (MdFI) between positive and negative populations. (**E**) Comparison of brightness achieved using SS cells versus beads and the FS sample for BUV395 HLA-DR. Black line shows the maximum fluorescence of positive stained cells. In this example, cells should be used for unmixing as they are brighter than the beads. (**F**) Comparison of brightness achieved using SS cells versus beads as compared to the FS sample for PE-CF594 PLZF. In this example, beads are brighter than cells and should be used for unmixing. Black line shows the maximum fluorescence of positive stained beads is brighter than the FS sample. (**G**) Final decision of optimal SRCs (cells or beads) used for unmixing the panel.

15. Stain all cells and beads with 100 µl of the appropriate antibody mix and incubate in the dark using the incubation time and temperature that will be used in the final assay.

16. Centrifuge as above and flick off the supernatant.

17. Wash twice with 200 µl FACS staining buffer, centrifuging again after each wash.

    At this stage, cells may be fixed (e.g., 1% paraformaldehyde) if required for biosafety or sample longevity. If cells are fixed, beads must also be fixed to ensure equal treatment of fluorophores and to mimic any change to the spectral signature caused by fixation. The fixative must be removed by washing twice with FACS staining buffer before acquisition.

18. Resuspend in 200 µl FACS staining buffer.

19. Acquire on a Cytek Aurora, taking care to meet the following acquisition criteria:

    a. Cytek assay settings are used as a starting point for instrument setup.
    b. The scatter profiles of cells and beads are on scale and the FSC area scaling factor (ASF) is optimized (see example in Fig. 2B).
    c. All fluorescence signals are on scale ($<4 \times 10^6$). This can be assessed in the full-spectrum plot or in individual plots for every detector.
    d. All tubes are recorded with the same fluorescence gain settings for each detector.
    e. Sufficient events are recorded to find a clear positive signal.

    A minimum of 300 events is needed for each positive and negative population. A good starting point is 5000 total events for beads and 30,000-50,000 total events for cell controls, although it may be necessary to record >50,000 cells to get at least 300 positive events of similar fluorescence intensity for rare markers.

Evaluate results (see Video 1)

20. In the SpectroFlo software, check the raw reference control data and verify that the acquisition criteria in the previous steps have been met:

    a. The scatter profiles of the cells and beads are on-scale, clean, and easily gated, and the FSC ASF has been optimized (Fig. 2B).
    b. Cytek assay settings or a close alteration (also see Critical Parameters discussion of Complex Samples and see Support Protocol 2) have been used, and all tubes have been recorded with the same settings.

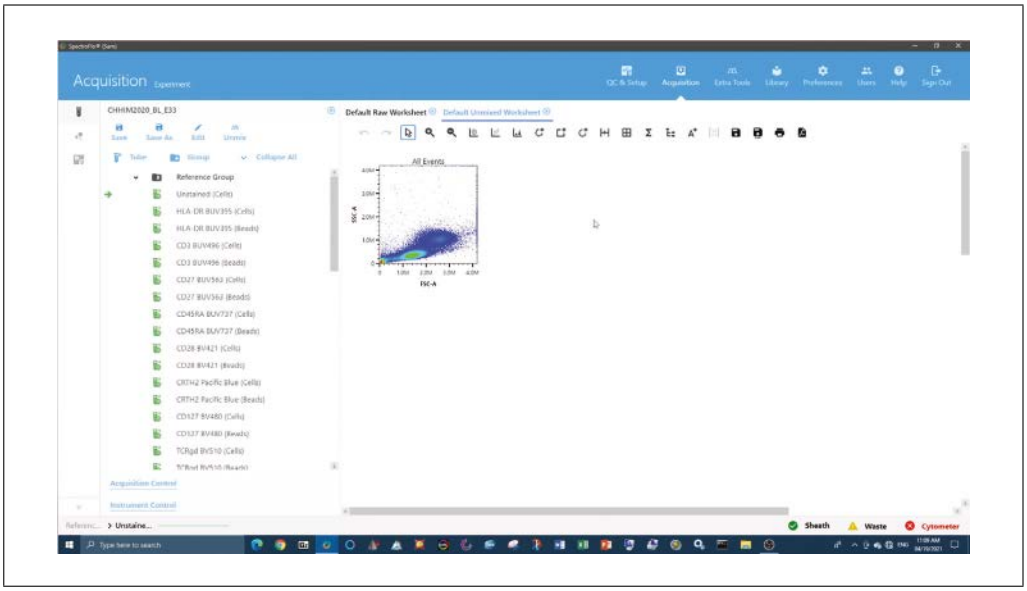

Video 1 Evaluation of optimal spectral reference controls (Basic Protocol 1).

21. Ensure that the unstained sample has no contamination from other fluorophores.

    Unstained cells often have AF signal in the detectors off the UV and violet lasers, which should not be mistaken for contamination.

22. In the SpectroFlo software, step through the Unmixing Wizard and select beads for all SRCs except for unstained and viability controls.

23. Accurately place positive and negative gates for unmixing.

    When setting scatter gates on bead SRCs, it is common to see singlet and doublet populations. Set the scatter gate on the smaller-sized (lower FSC) or more abundant singlet population. Beads should show little variability in staining level when prepared as described above, and thus the positive gate may include the complete positive bead population. If multiple peaks are seen, verify that they are not contaminating fluorophores or sample carryover, and optimize the staining procedure where needed to achieve homogenous staining intensity across all positive beads.

24. Perform quality control (QC) of all spectral signatures by verifying the following criteria:

    a. The peak channel matches that defined in Cytek's Full Spectrum Viewer (*spectrum.cytekbio.com*).
    b. The spectral signature appears as expected based on Cytek's Full Spectrum Viewer, published Cytek fluorophore guidelines, or historical data.
    c. Each channel contains a tight population of events.
    d. All fluorescent signals are on-scale ($<4 \times 10^6$). This can be assessed in the full-spectrum plot or in individual plots for every detector.
    e. Sufficient events have been recorded to find a clear positive signal.

25. Iterating through each fluorophore, place the positive gate over the negative population to verify that there is no fluorophore contamination (Fig. 2C).

26. Under the QC Controls tab, check Similarity Indices to ensure all spectral signatures are unique (i.e., all values within the matrix are ≤ 0.98).

27. Select the Live Unmix button to generate unmixed FCS files.

28. Create N × N plots on an unmixed worksheet (e.g., using software such as FlowJo or FCS Express).

    a. Create as many pseudocolor or dot plots as there are fluorophores in the panel.
    b. Ensure all *x* axes are set to the same fluorophore.
    c. Set each *y* axis to a different fluorophore in the panel.
    d. Change the *x* and *y* axes from manual scaling to autoscaling in the plot properties.
    e. Save this workspace as a template for use in later protocol steps.

29. Select the first SS cell sample.

30. Select all N × N plots. Then, in the Plot Properties window, change the *x*-axis option to the fluorophore matching the selected sample so all plots change simultaneously.

31. Evaluate the unmixing accuracy of the marker on the *x* axis by visually inspecting whether the positive and negative populations are well aligned horizontally along the *x* axis. If unmixing errors are seen in the N × N matrix plots (Fig. 2D, top), make a note of which control was being viewed.

32. Repeat steps 29-31 until the unmixing of all fluorophores has been evaluated.

33. Note which fluorophores require cells to be used for the SRC (i.e., those with identified unmixing errors in step 31). All other controls can remain as beads.

The most likely explanation for bead SRCs not unmixing the cell SRCs correctly is that the signature of the fluorophore on the beads did not match that of the cells. This phenomenon is known to happen but cannot be easily predicted. Another possible cause is that the bead SRC is dimmer than the cell SRC (Fig. 2E,F). If all recommendations for treatment of SS cells have been followed (i.e., identical treatment to FS cells, use of the same number of cells), then the cell SRC should have identical brightness to the FS cells and thus be an appropriate control.

34. Go through the Unmixing Wizard a second time using the controls identified in step 33 as the optimal controls. Unmix again using live unmixing.

35. Follow steps 23-26 for the modified controls to ensure the best unmixing outcome is achieved.

    When setting gates using cells as SRCs, the scatter gate should be placed only on the cells expressing the marker of interest for each control. In cases where there is no negative staining in this population, a universal negative may be used as a surrogate. To ensure the observed negative signal is due to AF rather than contamination, compare it to the matching unstained tube.

36. Repeat steps 29-32 to evaluate the new unmixing for the fluorophores that did not unmix optimally before (Fig. 2D, bottom) and note which fluorophores require cells or beads to be used for the SRC (Fig. 2G).

    Even with high-quality reference controls, unmixing errors may arise if incorrect gates are used in the Unmixing Wizard or if the spectral signatures have mismatches (see troubleshooting Tables 2-5 for more potential issues and how to fix them).

SUPPORT PROTOCOL 1

ANTIBODY TITRATION

Antibody titration is the crucial first step in developing high-dimensional flow cytometry panels. Using the incorrect antibody concentration can increase spread, decrease resolution, increase aggregation of reagents, and give rise to nonspecific binding (Stewart & Stewart, 1997), all of which result in poor panel performance and/or inaccurate results. Ideally, titrations should be carried out in the tissue that will be used in the assay. This is not always feasible, however, if the tissue in question is rare or difficult to work with, or the cells of interest are found at low frequencies within the tissue. In such cases, it is suggested to first add a lineage marker to the mix to help identify the cells that express the rarer marker or to use a surrogate tissue in which the marker is more abundant and simpler to process. Results from this type of titration should always be validated using the tissue of interest.

It is important that readout functional markers are titrated under the maximally activated conditions that will be used in the assay. Staining conditions should also be identical between titration and experiment to prevent spectral pattern mismatches and poor unmixing results.

This protocol describes the preparation of cryopreserved peripheral blood mononuclear cells (PBMCs) for titration of extracellular antibodies. It can be easily adapted and used as a general guideline for antibody titration using other tissues or staining procedures.

Materials

Cryopreserved PBMCs
Phosphate-buffered saline (PBS; Gibco, cat. no. 14190-250)
Fetal bovine serum (FBS; Gibco, cat. no. 10091-148)
Zombie NIR Fixable Viability Kit (BioLegend, cat. no. 423106)
Human TruStain FcX (Fc Receptor Blocking Solution; BioLegend, cat. no. 422301)

Polystyrene compensation beads (e.g., UltraComp eBeads, Life Technologies, cat. no. 01-222-42)
Antibodies (see Table 1)
FACS staining buffer: PBS with 2% bovine serum albumin (BSA; MP Biochemicals, CAS no. 9048-46-8) and 0.2% sodium azide (Sigma-Aldrich, cat. no. S8032)

37°C water bath (e.g., Julabo Ecotemp TW12)
Hemocytometer (e.g., Hawksley Counting Chamber) and coverslips
96-well U-bottom plate (In Vitro Technologies, cat. no. 353077)
Filters with 0.65-μm or smaller pore size (*optional*)
Spectral cytometer (e.g., Cytek Aurora)
5-ml polypropylene round-bottom flow tubes (In Vitro Technologies, cat. no. 352008)
Data analysis software for analyzing FCS files (e.g., FlowJo or FCS Express)

Prepare and acquire samples

1. Thaw PBMCs quickly in a 37°C water bath and add to 5 ml PBS with 2% FBS.

   CAUTION: Steps 1-2 should be performed in a biosafety hood.

2. Centrifuge 5 min at 500 × *g*, room temperature, and carefully flick off the supernatant.

3. Resuspend cells in PBS with 2% FBS and count on a hemocytometer.

4. Centrifuge as before and carefully flick off the supernatant.

5. Resuspend cells in PBS with 2% FBS to a concentration of 5×10^6 cells/ml.

6. Distribute 100 μl suspension per well of a 96-well U-bottom plate, allocating six wells to each antibody being titrated. Include additional wells for unstained and live/dead controls (see example plate plan in Fig. 3A).

   The number of titer points is based on the range of concentrations being tested. The number of cells required will differ by tissue type; for PBMCs, ~5×10^5 cells is sufficient.

7. Centrifuge plate 5 min at 500 × *g*, 4°C, and flick off the supernatant.

8. Stain titration samples and live/dead controls with a viability dye that will not cause significant spillover into the fluorophore being titrated.

   Viability dyes should also be titrated for use in high-dimensional spectral cytometry panels. When titrating a viability dye, skip steps 8-12 for that sample only (adding PBS instead if other samples are being processed simultaneously). If the viability dye has not yet been titrated, follow manufacturer guidelines for concentration and incubation procedures.

9. Centrifuge as above and flick off the supernatant.

10. Block Fc receptors by applying 100 μl of a 1:40 dilution of Human TruStain FcX and incubating 10 min at 4°C.

11. Add one drop of vortexed compensation beads per well for the appropriate single stain (SS) controls.

12. Centrifuge as above and flick off the supernatant.

13. Remove aggregates from antibody stocks by centrifuging the vials 5 min at 16,000-18,000 × *g*, 4°C, or by filtering using a pore size of 0.65 μm or smaller.

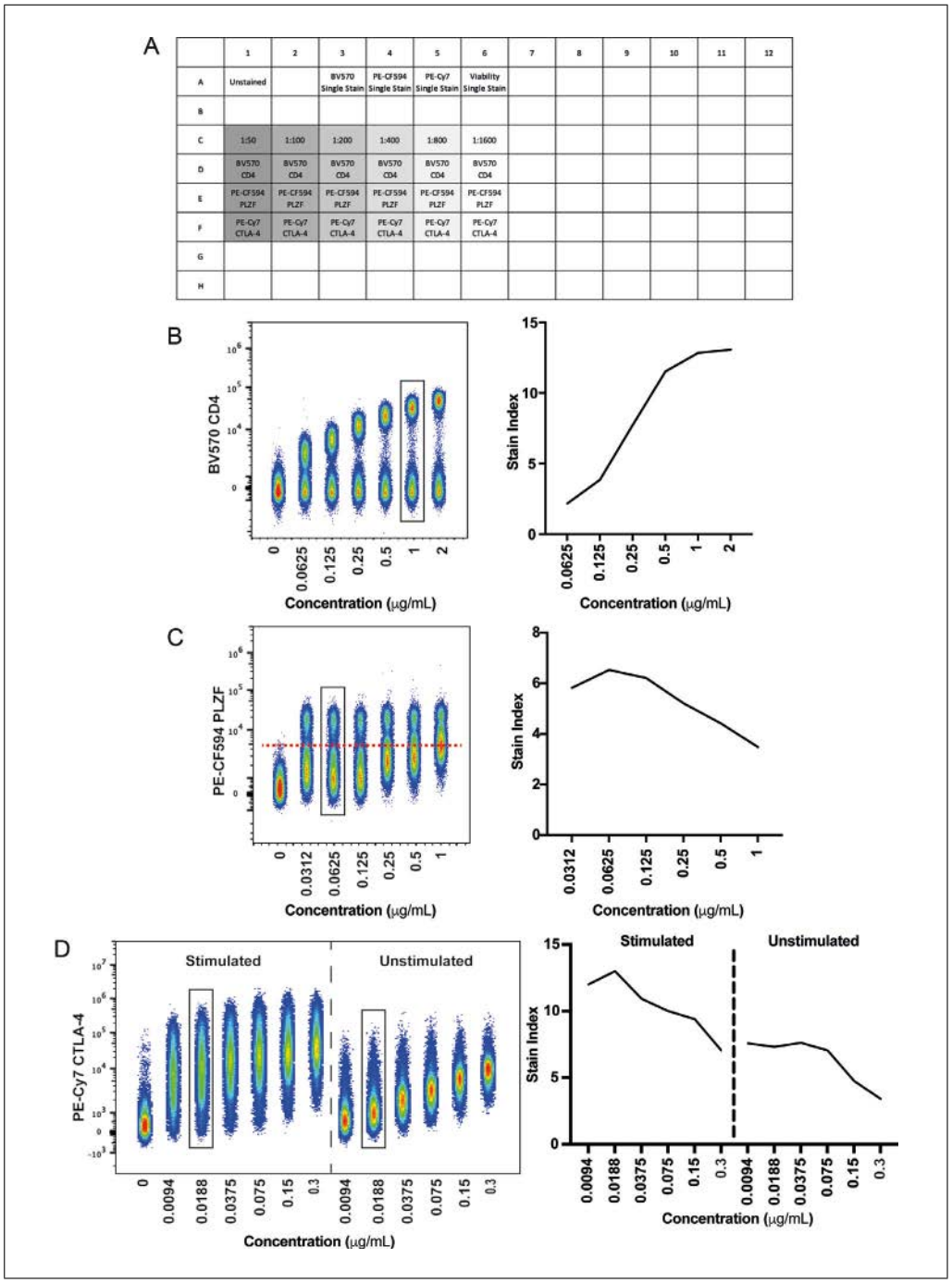

Figure 3 Antibody titration. Example titration of 1:2 serial dilutions for a range of marker subtypes, showing both concatenated flow cytometry data files and the calculated SI. The final dilution selected for the panel is indicated by black boxes. (**A**) Example plate layout. (**B**) T-cell co-receptor CD4 conjugated to BV570. (**C**) Transcription factor PLZF conjugated to PE-CF594. (**D**) Activation marker CTLA-4 conjugated to PE-Cy7 on cells with and without PHA stimulation (5 μg/ml, 2 days).

14. Create a dilution series for each antibody being titrated by diluting stock solutions in FACS staining buffer. Be sure to pipette from the top of the liquid to avoid the spun-down aggregates.

    A suggested dilution series is 1:50, 1:100, 1:200, 1:400, 1:800, 1:1600. This series is broad enough to ensure the likelihood of finding the optimal titer for a range of antibodies. For ease of preparation, concentrations are listed here only in terms of their dilution from stock; actual concentrations (in mg/ml) should be calculated once a titer is selected.

15. Add 100 µl of each antibody dilution to the corresponding sample in the plate. Add FACS staining buffer to unstained and live/dead controls. For compensation beads, use 100 µl of the 1:100 dilution.

    The dilution used for compensation beads should not fall off-scale when using Cytek assay settings, but should be brighter than the samples. A 1:100 dilution is a good starting point, but a lower dilution can be used if some antibodies are too bright.

16. Incubate using the time and temperature that will be used in the final assay.

17. Centrifuge as above and flick off the supernatant.

18. Wash twice with 200 µl FACS staining buffer.

    If fixation will be used for the final samples, titrations should also be determined using fixed samples. For additional details, see Basic Protocol 1, step 17.

19. Resuspend in 200 µl FACS staining buffer and acquire on a Cytek Aurora using Cytek assay settings.

Analyze data

20. Open titration samples in a data analysis software used for analyzing FCS files.

21. Generate median fluorescence intensity (MdFI) values for the positive and negative populations for each concentration.

22. Generate standard deviation (SD) values for the negative population for each concentration.

23. Calculate the stain index (SI) using the equation SI = (MdnFI*pos* – MdnFI*neg*) / (2 × SD*neg*).

    The stain index is a very useful metric of resolution, with a higher value indicating greater resolution. If a lower concentration of antibody produces a reduced positive population MdnFI compared to a higher concentration with no change to the negative population, its stain index is going to decrease, as the separation between the positive and negative populations will be reduced (see example in Fig. 3B). If a higher concentration of antibody gives rise to a similar positive population MdnFI compared to a lower concentration, but has a larger SD of the negative population, its stain index is going to be decreased, as spreading of the negative population reduces the resolution from the positive (see example in Fig. 3C).

24. Select the concentration that gives rise to the best stain index without giving rise to a positive shift of the negative population.

    Such a shift is best visualized by concatenating all FCS files and displaying them on a single plot (as shown in in Fig. 3B-D).

CHANGING INSTRUMENT SETTINGS

SUPPORT PROTOCOL 2

In some cases an adjustment of fluorescent gain settings away from the optimized settings cannot be avoided, for instance, if a bright reporter protein (e.g., eGFP) is off-scale. Such adjustments must be carried out carefully to minimize impact on all spectral signatures within the panel. Adjustments can be made detector by detector or to a whole detector array at one time, where all detectors of a given laser line are changed simultaneously. Reduction of the whole array is the recommended approach, as manual alteration of single detectors is prone to distortion of spectral signatures, where the ratio of brightness from detector to detector is not maintained. Regardless, reducing whole detector arrays can lead to peak emissions of spectral signatures being shifted to an incorrect detector (potentially on a different laser line). Therefore, all changes must be checked to ensure

that signatures remain as expected based on Cytek's Full Spectrum Viewer, published fluorophore guidelines, or historical data.

1. Observe which fluorescent channel(s) has an off-scale signal.
2. Use trial and error to determine the gain setting that is appropriate to bring the emission peak on-scale (i.e., $<4 \times 10^6$ on the Aurora).

   Remember that gain and fluorescence have a linear relationship, so that a 50% reduction in gain will give rise to a 50% reduction in fluorescence signal.

3. Reduce secondary detector arrays with off-scale signals by the same percentage as the reduction made in step 2.
4. Use Cytek's Full Spectrum Viewer, published fluorophore guidelines, or historical data to check that the altered spectral signature retains the correct overall pattern and that the primary emission peak has not been reduced below any secondary emission peaks.

   If the overall pattern is correct, no further steps are required. Record all samples at these adjusted settings. If the overall pattern is not correct, continue to step 5.

5. If adjustments to other laser lines are required, continue reducing the respective detector arrays by the same percentage as in step 2.
6. Repeat steps 4 and 5 until the spectral signature appears as expected or all arrays have been reduced by the same percentage.
7. Record all samples at the adjusted settings.

BASIC PROTOCOL 2

UNMIXING EVALUATION OF FULLY STAINED SAMPLE

Before any analysis can be undertaken, the FS sample must be checked to ensure that clean data can be obtained through removal of artefacts such as doublets, dead cells, and aggregates. It is also necessary to verify that there is positive staining for all markers in the panel, taking into consideration the biology of each marker. Once this has been asserted, it must be determined whether the SRCs selected (either beads or cells) successfully unmix the SS cells in Basic Protocol 1 can also be used to successfully unmix the FS sample (Video 2).

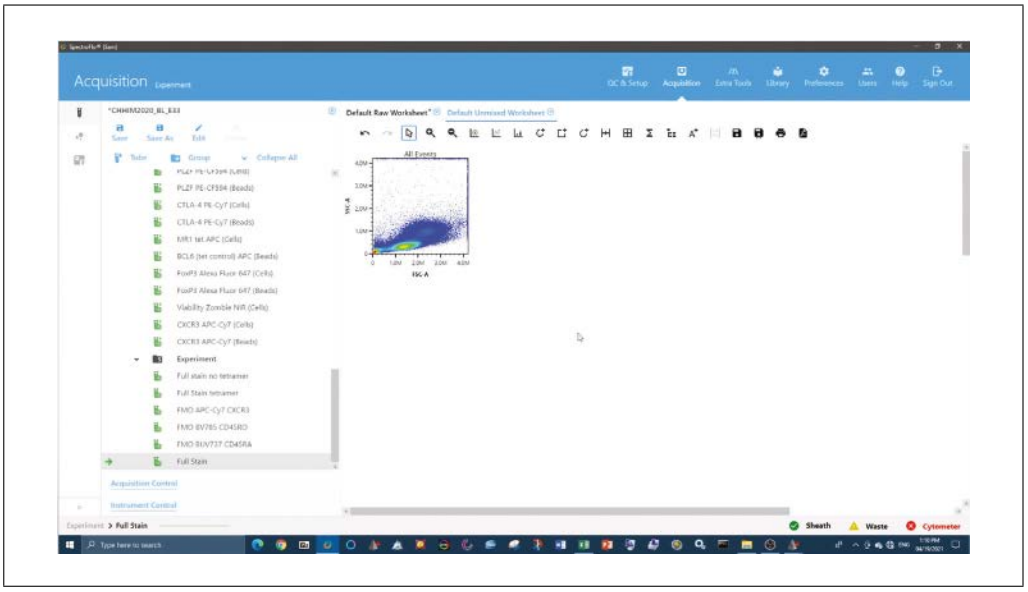

Video 2 Unmixing evaluation of fully stained sample (Basic Protocol 2).

Materials

Cytek SpectroFlo software
FCS files generated in Basic Protocol 1
N × N worksheet template

1. In the SpectroFlo software, work through the Unmixing Wizard and select the SRCs chosen from Basic Protocol 1.
2. In the unmixed workspace, gate on time to remove any events collected during an unstable flow period by plotting time vs. scatter (e.g., FSC-A or FSC-H; Fig. 4A).
3. Gate out doublets by sequentially plotting FSC-H vs. FSC-A and SSC-H vs. SSC-A, and include only the events found in the diagonal population (Fig. 4A).

   If working with whole blood or PBMC samples where incomplete RBC lysis was achieved, unlysed erythrocytes need to be excluded. One method is the blue/violet SSC gating method described by Petriz, Bradford, & Ward (2018).

4. Exclude aggregates through inspection of N × N plots for incorrectly unmixed super-bright events and gate these out of all further analyses (Fig. 4B).
5. Gate out dead cells by including only viability dye negative events (Fig. 4A).

   Viability dyes also need to be titrated (see Support Protocol 1).

6. Gate on cells of interest using FSC-A vs. SSC-A, including only the events required for analysis (Fig. 4A).

   If working with a sample that contains multiple cell types (such as PBMCs), include only the cells that will be involved in downstream analysis. For example, when analyzing a panel that contains only lymphocyte markers, gate out monocytes (validating that T cells are not excluded).

7. Create as many pseudocolor or dot plots as there are fluorophores in the panel. Set the *y* axis to SSC-A and each *x* axis to a different fluorophore (Fig. 4C).
8. Verify that a positive signal can be found for all markers (Fig. 4C).

   For rare or dim markers, FMOs can assist in determining the gating boundaries (Fig. 4D). If no clear signal is observed, take note of that reagent and check the titer and staining protocol. For additional troubleshooting, see Table 3.

9. Open the N × N worksheet template created previously and evaluate how well unmixing was performed for each marker. Inspect the FS sample by assessing whether super-negative events are present (example in Fig. 4E), which can be an indication of unmixing issues.
10. Select all plots making up the matrix. In the Plot Properties window, change the *x* axis option to the next fluorophore down the list so that all plots change simultaneously.
11. Repeat steps 9-10 until all fluorophores have been checked.
12. If there are no major unmixing errors (i.e., the positive and negative populations of each marker in the N × N plots are well aligned), continue to evaluation of marker resolution (see Basic Protocol 3).
13. If there are unmixing issues, even once the unmixing has been performed correctly and optimally, it is possible to make small adjustments (<3%) to the compensation matrix (found in the Tube Properties window).

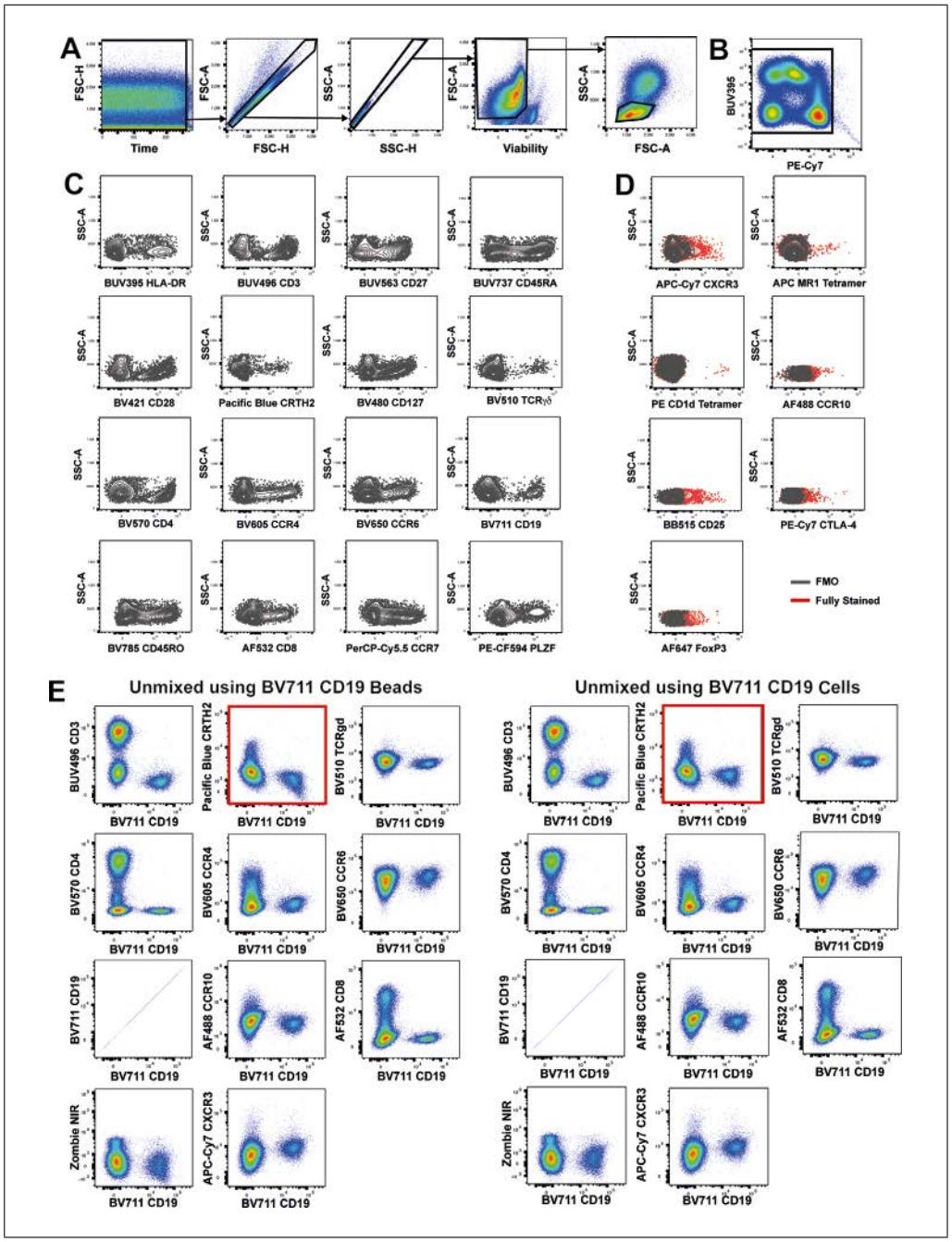

Figure 4 Inspection of the FS sample. *(***A**) Gating strategy to gate out inconsistent flow rate events (time gate), doublets, and dead cells and include only cells of interest (lymphocytes). (**B**) Example of aggregates and how to gate them out. (**C**) Dot plots of SSC-A vs. each marker in the panel. (**D**) Dot plots of SSC-A vs. rare/dim markers in the panel, overlaid with FMO controls to show true positive events. (**E**) N × N matrix used to evaluate marker positivity from core panel iteration unmixed using beads (left) or cells (right).

Adjustments to the spillover matrix should be fully justified and the integrity of the data must not be impacted (made with clear knowledge of the biology, such as expression and pattern characteristics). Under-unmixing and over-unmixing issues can be manually adjusted (Ashhurst, Smith, & King, 2017). It is unlikely that there would be a need for more than a 2% to 3% correction. If greater correction is needed, the unmixing accuracy needs to be re-evaluated.

If the samples are something other than PBMCs and significant unmixing issues are still present, more information on how to proceed can be found in the Commentary (see Critical Parameters, Complex Samples).

EVALUATION OF MARKER RESOLUTION

Once the best possible unmixing has been achieved using Basic Protocols 1 and 2, the resolution of each marker in the FS sample must be compared to the SS cell controls. Assessing the spread of the negative population and/or shifts in the positive signal will provide an indication of whether there is any loss of resolution of markers in the panel when fully stained. This assessment is best achieved by overlaying each marker in the SS cell sample onto the FS sample. If any reduction in resolution is seen, the impact of this can be further investigated to identify if it will impact the ability to identify populations of interest using an established gating strategy. Ideally, the same number of cells from the same tissue type should be stained and acquired for all samples. In practice, however, this is not often feasible, and downsampling can be used to achieve identical cell numbers across samples during analysis. In theory, the only difference between the SS and FS cells should be the number of antibodies in the tube (Video 3). Additionally, AF extraction should be tested to determine if marker resolution can be improved (Video 4).

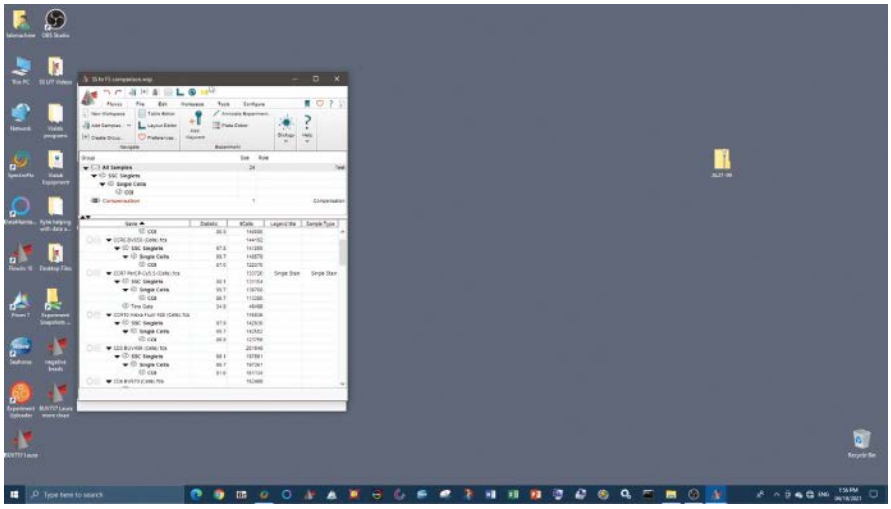

Video 3 Evaluation of marker resolution (Basic Protocol 3).

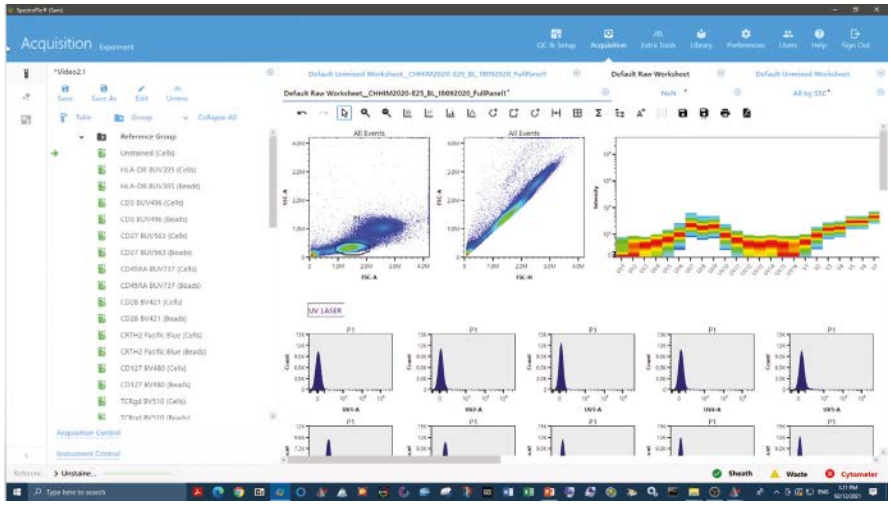

Video 4 Deciding on an approach for mitigating autofluorescence (Basic Protocol 3) and Support Protocol 3.

Materials

Data analysis software (e.g., FlowJo or FCS Express)
Cytek SpectroFlo software
FCS files generated in Basic Protocol 2
N × N worksheet template

Evaluate marker resolution (Video 3)

1. Open the unmixed FS and SS cell samples in a data analysis software package for analyzing FCS files (e.g., FlowJo or FCS Express).
2. Follow steps 2-6 of Basic Protocol 2.
3. Create a histogram for each fluorophore in the panel (Fig. 5A). If the positive population is rare, use a dot plot for visualization purposes instead of a histogram (Fig. 5B).
4. Overlay the same number of FS and SS cell sample events onto a histogram or dot plot (Fig. 5A,B).

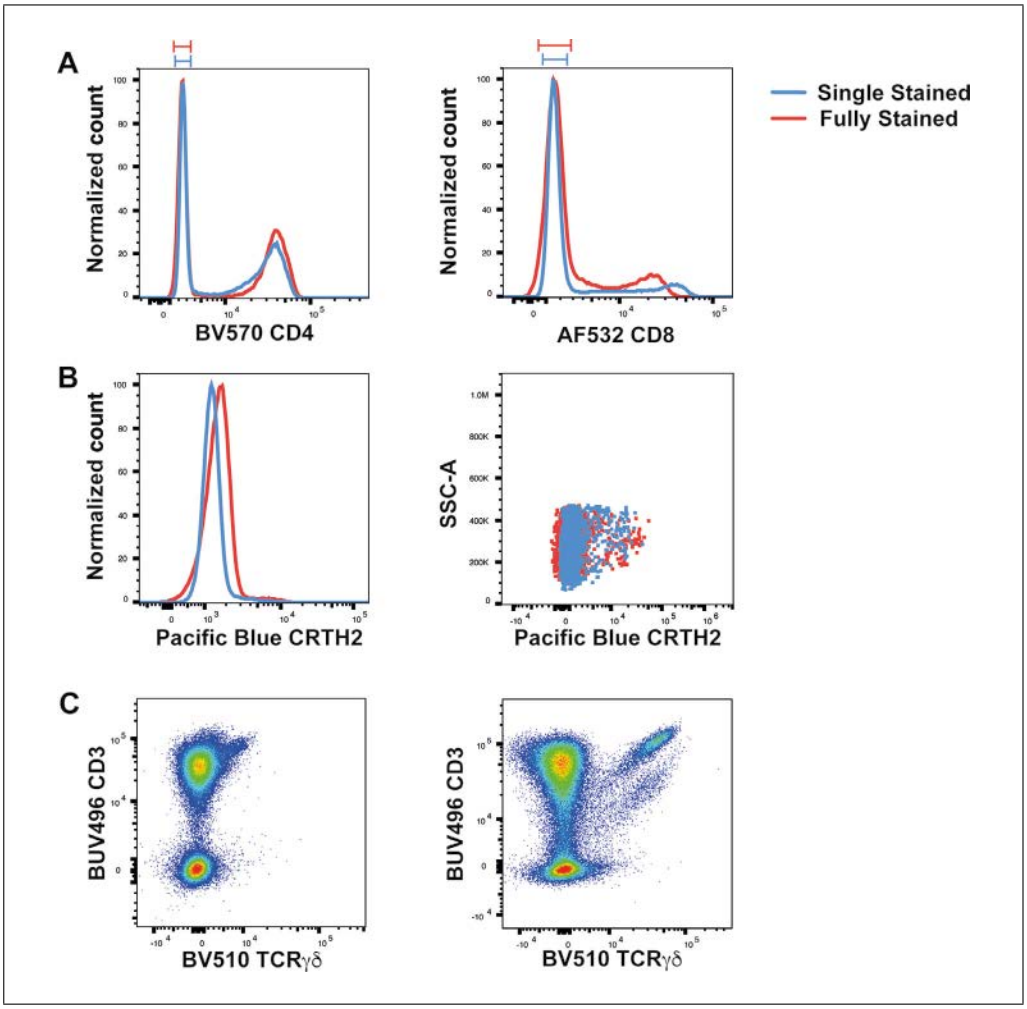

Figure 5 Evaluation of marker resolution. (**A**) A histogram overlay of BV570 CD4 SS cells vs. FS sample (left) provides an example with no additional spread in the negative population, whereas a histogram overlay of AF532 CD8 (right) depicts spreading of the negative population in the FS sample (red) compared to SS cells (blue). (**B**) Histogram and dot plot overlays of Pacific Blue CRTH2. (**C**) Dot plot of BUV496 CD3 vs. BV510 TCR$\gamma\delta$ before (left) and after (right) implementation of sequential staining (Park et al., 2020).

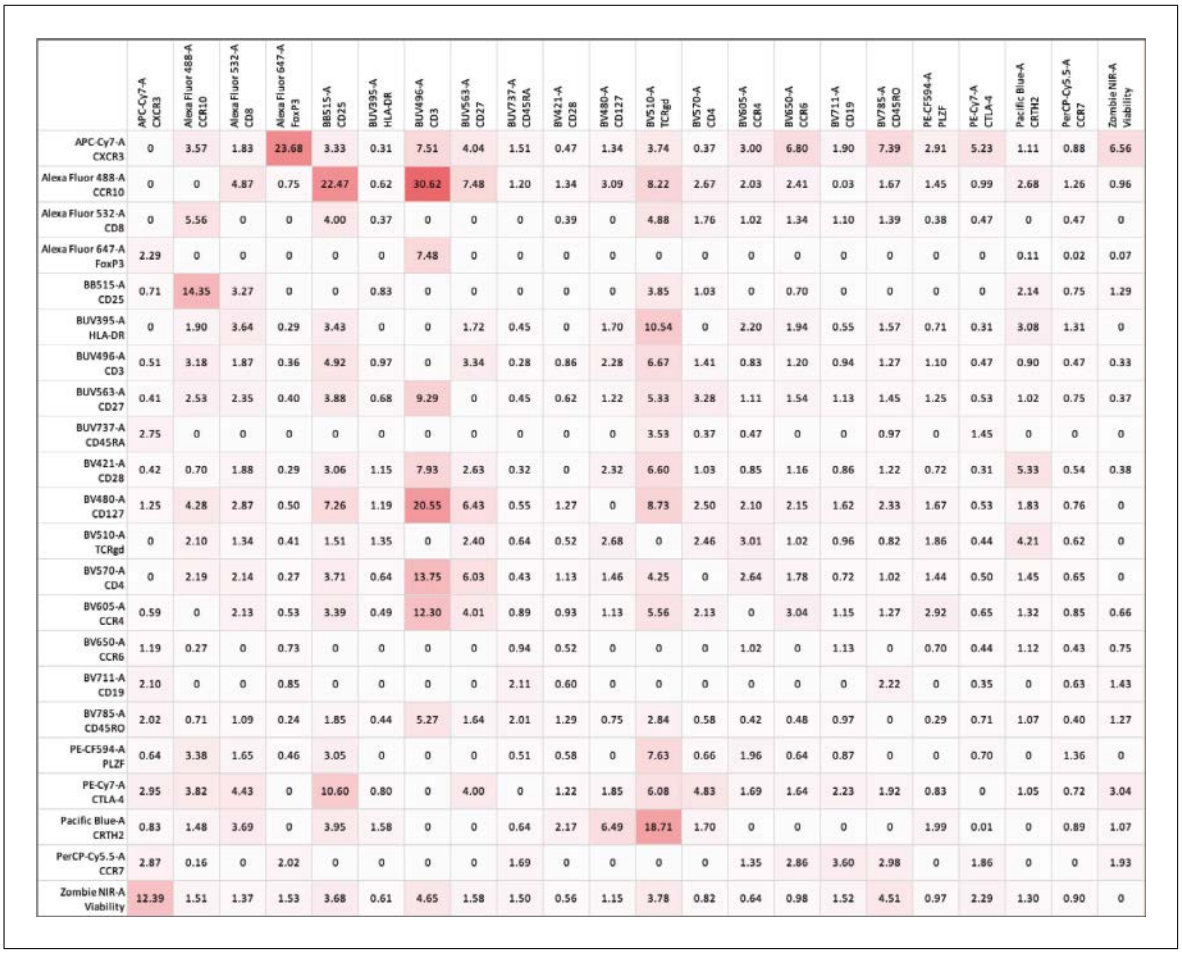

	APC-Cy7-A CXCR3	Alexa Fluor 488-A CCR10	Alexa Fluor 532-A CD8	Alexa Fluor 647-A FoxP3	BB515-A CD25	BUV395-A HLA-DR	BUV496-A CD3	BUV563-A CD27	BUV737-A CD45RA	BV421-A CD28	BV480-A CD127	BV510-A TCRgd	BV570-A CD4	BV605-A CCR4	BV650-A CCR6	BV711-A CD19	BV785-A CD45RO	PE-CF594-A PLZF	PE-Cy7-A CTLA-4	Pacific Blue-A CRTH2	PerCP-Cy5.5-A CCR7	Zombie NIR-A Viability
APC-Cy7-A CXCR3	0	3.57	1.83	23.68	3.33	0.31	7.51	4.04	1.51	0.47	1.34	3.74	0.37	3.00	6.80	1.90	7.39	2.91	5.23	1.11	0.88	6.56
Alexa Fluor 488-A CCR10	0	0	4.87	0.75	22.47	0.62	30.62	7.48	1.20	1.34	3.09	8.22	2.67	2.03	2.41	0.03	1.67	1.45	0.99	2.68	1.26	0.96
Alexa Fluor 532-A CD8	0	5.56	0	0	4.00	0.37	0	0	0	0.39	0	4.88	1.76	1.02	1.34	1.10	1.39	0.38	0.47	0	0.47	0
Alexa Fluor 647-A FoxP3	2.29	0	0	0	0	0	7.48	0	0	0	0	0	0	0	0	0	0	0	0	0.11	0.02	0.07
BB515-A CD25	0.71	14.35	3.27	0	0	0.83	0	0	0	0	0	3.85	1.03	0	0.70	0	0	0	0	2.14	0.75	1.29
BUV395-A HLA-DR	0	1.90	3.64	0.29	3.43	0	0	1.72	0.45	0	1.70	10.54	0	2.20	1.94	0.55	1.57	0.71	0.31	3.08	1.31	0
BUV496-A CD3	0.51	3.18	1.87	0.36	4.92	0.97	0	3.34	0.28	0.86	2.28	6.67	1.41	0.83	1.20	0.94	1.27	1.10	0.47	0.90	0.47	0.33
BUV563-A CD27	0.41	2.53	2.35	0.40	3.88	0.68	9.29	0	0.45	0.62	1.22	5.33	3.28	1.11	1.54	1.13	1.45	1.25	0.53	1.02	0.75	0.37
BUV737-A CD45RA	2.75	0	0	0	0	0	0	0	0	0	0	3.53	0.37	0.47	0	0	0.97	0	1.45	0	0	0
BV421-A CD28	0.42	0.70	1.88	0.29	3.06	1.15	7.93	2.63	0.32	0	2.32	6.60	1.03	0.85	1.16	0.86	1.22	0.72	0.31	5.33	0.54	0.38
BV480-A CD127	1.25	4.28	2.87	0.50	7.26	1.19	20.55	6.43	0.55	1.27	0	8.73	2.50	2.10	2.15	1.62	2.33	1.67	0.53	1.83	0.76	0
BV510-A TCRgd	0	2.10	1.34	0.41	1.51	1.35	0	2.40	0.64	0.52	2.68	0	2.46	3.01	1.02	0.96	0.82	1.86	0.44	4.21	0.62	0
BV570-A CD4	0	2.19	2.14	0.27	3.71	0.64	13.75	6.03	0.43	1.13	1.46	4.25	0	2.64	1.78	0.72	1.02	1.44	0.50	1.45	0.65	0
BV605-A CCR4	0.59	0	2.13	0.53	3.39	0.49	12.30	4.01	0.89	0.93	1.13	5.56	2.13	0	3.04	1.15	1.27	2.92	0.65	1.32	0.85	0.66
BV650-A CCR6	1.19	0.27	0	0.73	0	0	0	0	0.94	0.52	0	0	0	1.02	0	1.13	0	0.70	0.44	1.12	0.43	0.75
BV711-A CD19	2.10	0	0	0.85	0	0	0	0	2.11	0.60	0	0	0	0	0	0	2.22	0	0.35	0	0.63	1.43
BV785-A CD45RO	2.02	0.71	1.09	0.24	1.85	0.44	5.27	1.64	2.01	1.29	0.75	2.84	0.58	0.42	0.48	0.97	0	0.29	0.71	1.07	0.40	1.27
PE-CF594-A PLZF	0.64	3.38	1.65	0.46	3.05	0	0	0	0.51	0.58	0	7.63	0.66	1.96	0.64	0.87	0	0	0.70	0	1.36	0
PE-Cy7-A CTLA-4	2.95	3.82	4.43	0	10.60	0.80	0	4.00	0	1.22	1.85	6.08	4.83	1.69	1.64	2.23	1.92	0.83	0	1.05	0.72	3.04
Pacific Blue-A CRTH2	0.83	1.48	3.69	0	3.95	1.58	0	0	0.64	2.17	6.49	18.71	1.70	0	0	0	0	1.99	0.01	0	0.89	1.07
PerCP-Cy5.5-A CCR7	2.87	0.16	0	2.02	0	0	0	0	1.69	0	0	0	0	1.35	2.86	3.60	2.98	0	1.86	0	0	1.93
Zombie NIR-A Viability	12.39	1.51	1.37	1.53	3.68	0.61	4.65	1.58	1.50	0.56	1.15	3.78	0.82	0.64	0.98	1.52	4.51	0.97	2.29	1.30	0.90	0

Figure 6 Spillover spreading matrix for 24 unique-signature fluorophores used in combination on a panel used to illustrate the protocol. Spread is contributed by fluorophores listed in the rows, impacting the fluorophores listed in the columns. Spillover values are color-coded as follows: white, <3; shades of pink, 3–9; red, >9 (for example, BV480 spreads strongly into BUV496).

To ensure that each sample contains equal events, downsample the cells of interest population from all samples to the same number of events based on the sample with the fewest cells of interest. In FlowJo, for example, select the population of interest, then go to the Workspace tab and select Plugins and then DownSample. Specify the number of events to be downsampled such that all samples can meet the criteria.

5. Determine whether any spreading of the negative population has occurred in the FS sample (Fig. 5A, right).

6. Determine whether such spreading has impacted the resolution of positive and negative populations, either visually or by calculating stain index (SI; see Support Protocol 1, step 22).

7. Create a spillover spreading matrix (SSM) to assess which fluorophores are likely to be introducing spread to the fluorophore of interest (in Fig. 6, find the SSM for the panel used to illustrate the protocol).

In FlowJo, for example, using the SS cells SRCs, navigate through the Compensation Wizard defining positive and negative populations for each fluorophore. The SSM will be automatically generated alongside the compensation matrix and can be displayed or exported from the SSM button.

If the spread of the negative population results in significant loss of resolution such that separation of positive and negative populations becomes difficult, and the marker is

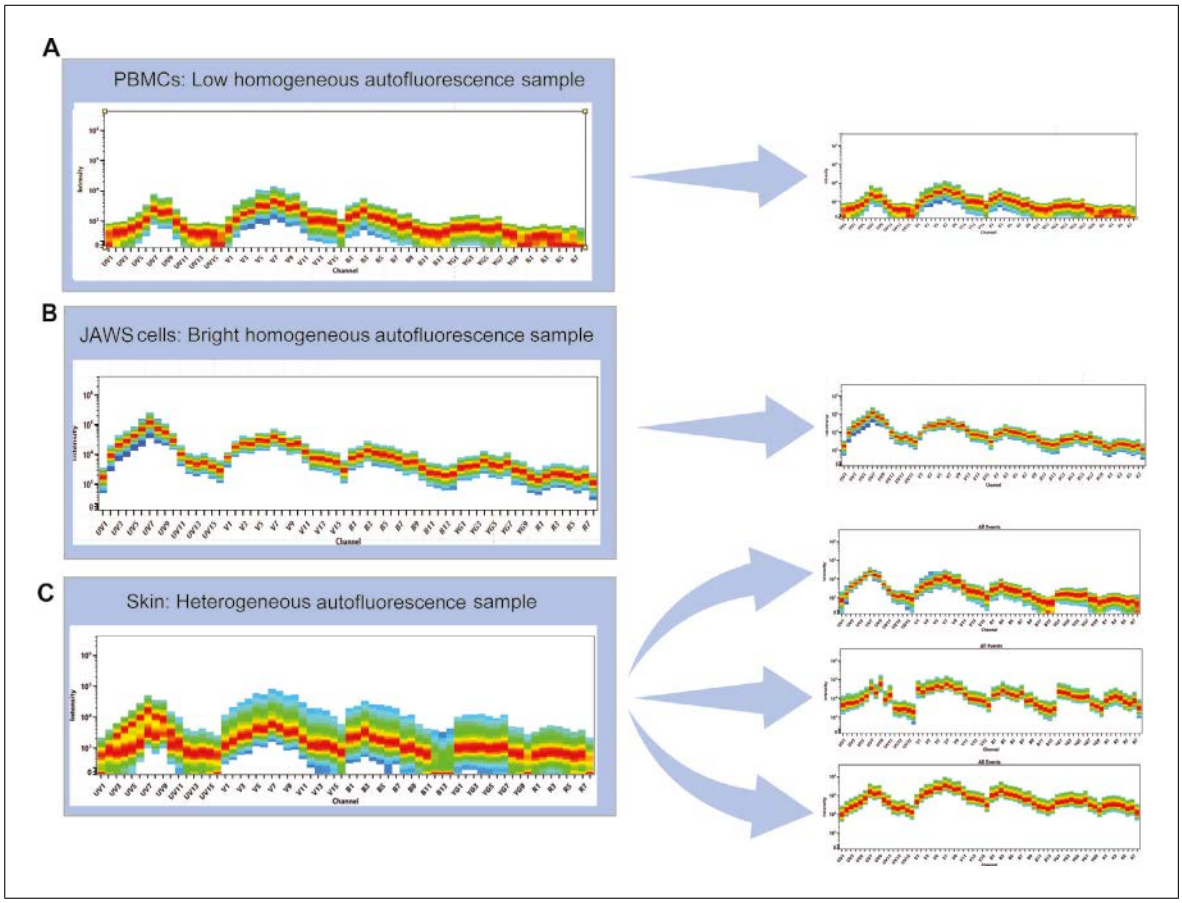

Figure 7 Determination of AF signature type. AF signatures of (**A**) unstained PBMCs, (**B**) unstained JAWS cells (immortalized immature dendritic cell line), and (**C**) unstained skin cells. The latter shows a highly heterogeneous signature that can be split into three unique spectral signatures.

co-expressed in the same cell type as the marker causing the spread, the panel design should be reconsidered and a different fluorophore may be needed to improve resolution.

8. Determine whether any loss in fluorescence intensity of given marker(s) has occurred in the FS when compared to the SS (Fig. 5C).

   Any reduction in positive signal should be investigated. An explanation is offered in Jalbert, Shikuma, Ndhlovu, & Barbour (2013) and Park et al. (2020), where sequential staining of chemokine receptors was required to achieve positive signal in the FS sample comparable to that of the SS cell controls. Sequential staining can also be applied to non-chemokine receptors (Fig. 5C).

Choose approach for mitigating AF (Video 4)

Two scenarios should be considered regarding AF: homogeneous AF, where the whole unstained sample has a single low spectral signature (Fig. 7A) or single bright spectral signature (Fig. 7B), or heterogeneous AF, where there are multiple AF signatures (Fig. 7C). For PBMCs, where the unstained sample has a relatively low homogeneous AF signature, the Simple AF Protocol can be followed to assess whether AF extraction improves marker resolution. AF extraction is particularly helpful in resolving low-expressed markers by lowering the background of the negative population with minimal effect on the positive signal. If samples have heterogeneous or homogeneous but very bright AF, it is likely that AF extraction must be used to obtain unmixing that looks correct in Basic Protocols 1 and 2. In this case, the decision to use AF extraction will be based on unmixing quality instead of improvement of marker resolution. The AF protocol for

heterogeneous AF is explained in detail in Critical Parameters (under Working with Complex Samples) and in Support Protocol 3.

Extract AF

9. Open SpectroFlo and proceed to the Unmixing Wizard.
10. Test the following options for unmixing:
    a. Unmix without AF extraction first. Select live unmixing.
    b. Repeat steps of the Unmixing Wizard with AF extraction, placing the scatter gate on the population of interest only. Select Unmix, Save & Open to generate a separate set of FCS files from step 10a.
11. If there are other cells of interest in the sample that have a brighter spectral signature, try to unmix with the scatter gate on this population in step 10b.
12. Determine the best unmixing outcome comparing the N × N plots by evaluating changes in resolution for the dyes that overlap with the range of emission of AF (e.g., BUV496, BV510, Pac Orange, BV570, FITC, PE).

MANAGING HETEREOGENEOUS AUTOFLUORESCENCE (VIDEO 5)

SUPPORT PROTOCOL 3

The following protocol is divided into three sections: Discover, Distinguish and Designate.

Discover

1. Observe N × N plot permutations of raw channel data.
    a. On the Aurora, draw as many pseudocolor or dot plots as channels.
    b. Leave the *x* axis unchanged.
    c. Set each *y* axis to the different channels, so each plot shows a different raw combination.

    An example of a SpectroFlo N × N raw template is shown in Figure 8.
2. Find a combination that separates the greatest number of populations from one another.

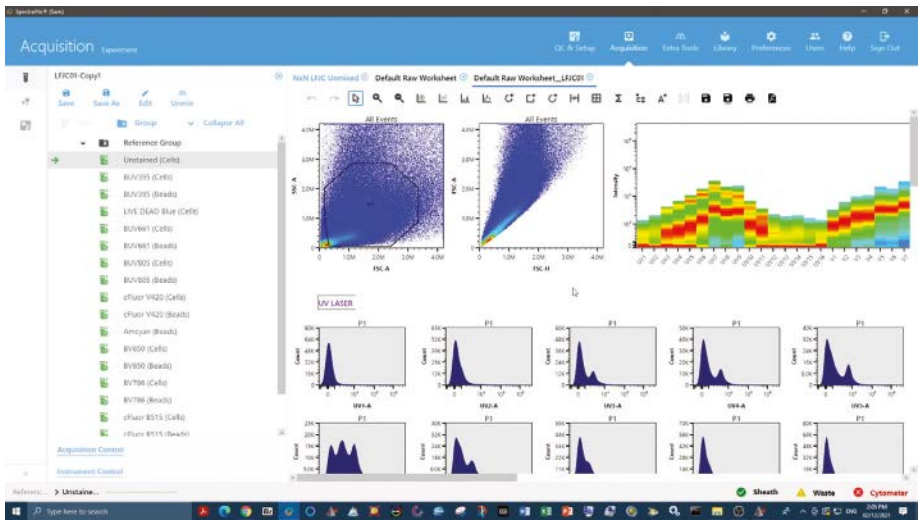

Video 5 Heterogeneous autofluorescence (Support Protocol 3).

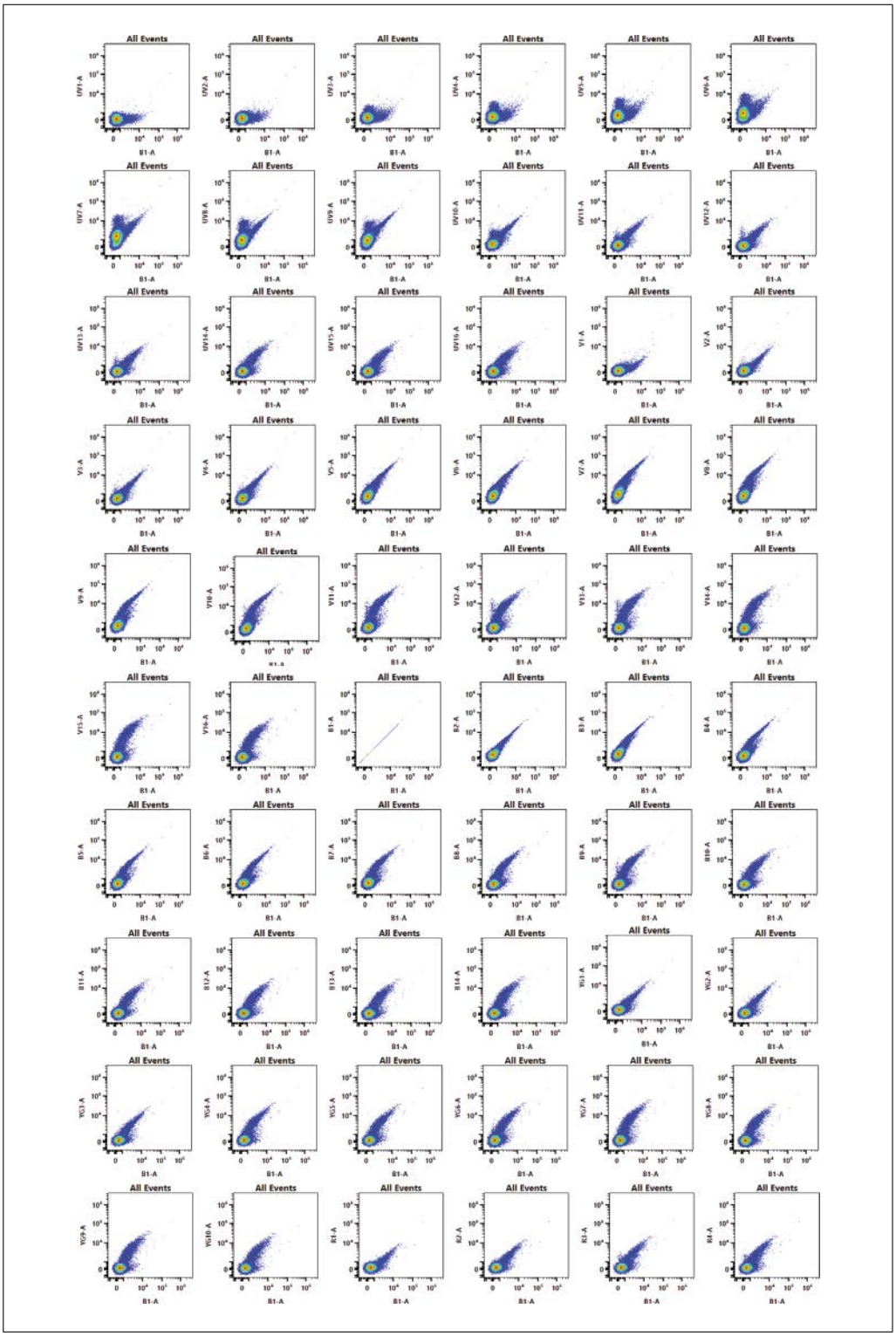

Figure 8 Example of an N × N raw worksheet.

Potential shortcut: Observe spectral plot showing ALL events and find one channel where there is obvious heterogeneity and one channel with similarity. This will immediately pull apart a minimum of two populations. Hint: Mid-range UV channels are most likely to show heterogeneity. If eosinophils are expected, YG1 will assist with isolating eosinophils from other populations.

Distinguish

3. Choose the plot with highest degree of separation.

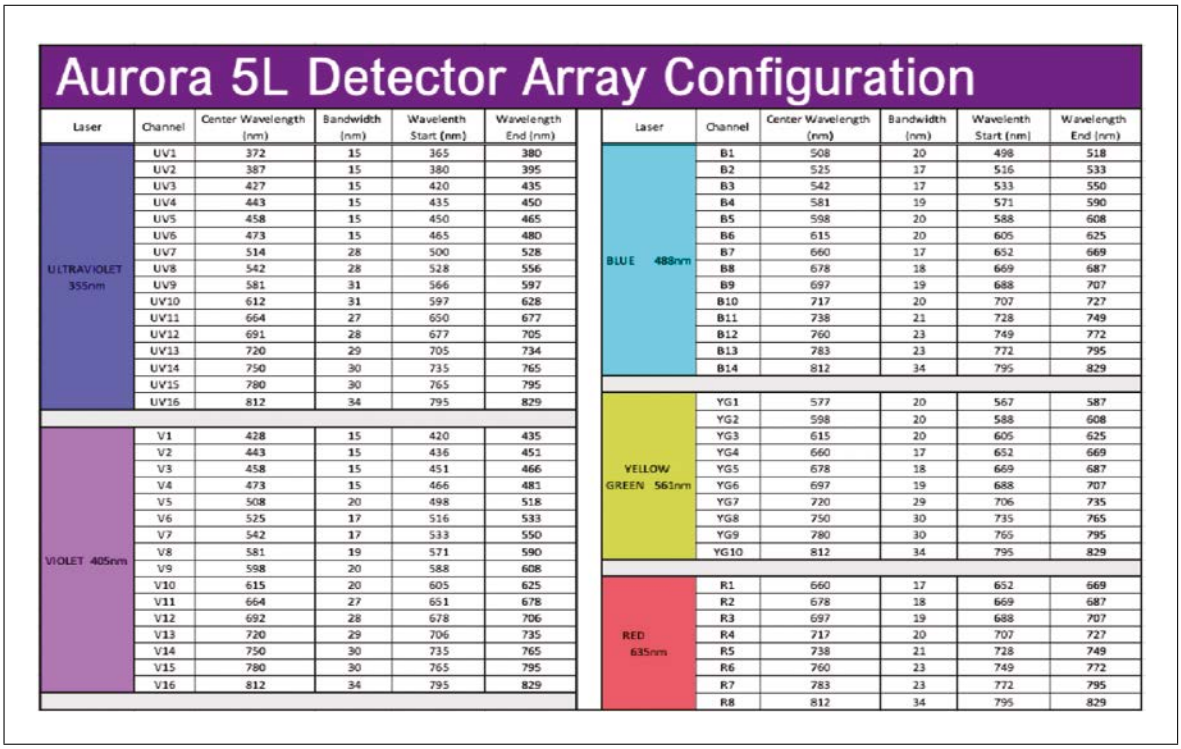

Aurora 5L Detector Array Configuration

Laser	Channel	Center Wavelength (nm)	Bandwidth (nm)	Wavelength Start (nm)	Wavelength End (nm)
ULTRAVIOLET 355nm	UV1	372	15	365	380
	UV2	387	15	380	395
	UV3	427	15	420	435
	UV4	443	15	435	450
	UV5	458	15	450	465
	UV6	473	15	465	480
	UV7	514	28	500	528
	UV8	542	28	528	556
	UV9	581	31	566	597
	UV10	612	31	597	628
	UV11	664	27	650	677
	UV12	691	28	677	705
	UV13	720	29	705	734
	UV14	750	30	735	765
	UV15	780	30	765	795
	UV16	812	34	795	829
VIOLET 405nm	V1	428	15	420	435
	V2	443	15	436	451
	V3	458	15	451	466
	V4	473	15	466	481
	V5	508	20	498	518
	V6	525	17	516	533
	V7	542	17	533	550
	V8	581	19	571	590
	V9	598	20	588	608
	V10	615	20	605	625
	V11	664	27	651	678
	V12	692	28	678	706
	V13	720	29	706	735
	V14	750	30	735	765
	V15	780	30	765	795
	V16	812	34	795	829

Laser	Channel	Center Wavelength (nm)	Bandwidth (nm)	Wavelength Start (nm)	Wavelength End (nm)
BLUE 488nm	B1	508	20	498	518
	B2	525	17	516	533
	B3	542	17	533	550
	B4	581	19	571	590
	B5	598	20	588	608
	B6	615	20	605	625
	B7	660	17	652	669
	B8	678	18	669	687
	B9	697	19	688	707
	B10	717	20	707	727
	B11	738	21	728	749
	B12	760	23	749	772
	B13	783	23	772	795
	B14	812	34	795	829
YELLOW GREEN 561nm	YG1	577	20	567	587
	YG2	598	20	588	608
	YG3	615	20	605	625
	YG4	660	17	652	669
	YG5	678	18	669	687
	YG6	697	19	688	707
	YG7	720	29	706	735
	YG8	750	30	735	765
	YG9	780	30	765	795
	YG10	812	34	795	829
RED 635nm	R1	660	17	652	669
	R2	678	18	669	687
	R3	697	19	688	707
	R4	717	20	707	727
	R5	738	21	728	749
	R6	760	23	749	772
	R7	783	23	772	795
	R8	812	34	795	829

Figure 9 Aurora 5L detector array configuration.

4. Place gates around all unique populations and observe the scatter properties and spectral signatures on adjacent spectral plots and select only the populations that have unique spectral characteristics.
5. Find the peak fluorescent channel for each unique population and then display said population on a histogram using this channel.
6. Gate the brightest 300-500 cells only, in order to derive the brightest AF SS control.
7. Right-click on the gate and export events as a new FCS file.
8. Repeat for all unique populations, producing an FCS file for each.
9. Export an AF dim population (dimmest AF spectral signature found in the sample) to be used as the negative control for the previously exported populations.

Designate

10. Designate these new AF signatures as fluorescence tags in the SpectroFlo Library.
    a. Create a new AF group.

       This will facilitate filtering and exporting these fluorophores for offline analysis, as well as identification when designing experiments.

    b. Assign the AF tag a name, choose the excitation laser, and assign an emission wavelength (use the optical configuration in Figure 9 to determine wavelength based on peak emission channel).
11. Open the experiment of interest and add the new AF tag(s) as if it were a fluorophore in the experiment.
12. In the reference controls tab, add an additional negative for the AF tags that will be the AF dim.

13. Import the populations exported during the Distinguish steps as SRCs for the corresponding tags, and import the AF dim population as an additional negative for the AF SRCs.

14. Use the Unmixing Wizard QC tools to assess AF signature similarity.

    In our experience, a similarity of 0.96 or less indicates that the AF signatures are generally considered to be unique.

15. Unmix the experiment and evaluate the unmixed N × N matrix.

    If unmixing errors are still present, refer to the troubleshooting guide in Table 3.

BASIC PROTOCOL 4

ASSESS DATA QUALITY USING EXPERT GATING AND DIMENSIONALITY REDUCTION ALGORITHMS

Informed gating is a useful way to check panel quality. It is necessary to check that all populations of interest can be identified and to investigate how well they can be resolved (Fig. 10A, Video 6). The biology of the sample should be considered to ensure that populations seen in the sample are as expected and that markers are expressed on all the expected cell types. This protocol indicates whether the panel is ready for use on experimental samples. Additionally, dimensionality reduction algorithms can be useful tools for investigating panel quality, as they simplify the data for visualization while also exposing artefacts that may be missed through expert gating. Using *t*-distributed stochastic neighbor embedding (*t*-SNE; van der Maaten & Hinton, 2008; Fig. 10B), markers that are usually co-expressed should be checked to see they are found in similar regions of the *t*-SNE plot (Brummelman et al., 2019).

Materials

Data analysis software (e.g., FlowJo, FCS Express, or any other software that allows gating of data)
FCS files generated in Basic Protocol 3

Perform expert gating

1. Open the unmixed FS sample in data analysis software used for analyzing FCS files.

2. Follow steps 2-6 of Basic Protocol 2 to gate on live single cells of interest.

3. Gate the rest of the markers based on panel design, prior knowledge, and published literature.

4. Check the gating strategy for unexpected marker combinations or cell populations (Fig. 10A).

   For example, when analyzing PBMCs, a $CD3^+CD19^+$ double-positive population is not expected. If one is found, the source of this staining must be investigated and corrected before the panel is ready for use.

5. Evaluate whether all populations of interest have clear positive signals that can be easily resolved from the negative.

6. Ensure readout markers (used for experimental readout) can be quantified in each of the cell types of interest.

Apply dimensionality reduction algorithm (t-SNE)

7. Using the cleaned data from step 2, run a *t*-SNE at the default settings (iterations: 1000; perplexity: 30) utilizing all fluorescence parameters. Exclude non-informative parameters such as those used in the data cleaning steps (e.g., viability and phenotypic markers for identifying cells of interest).

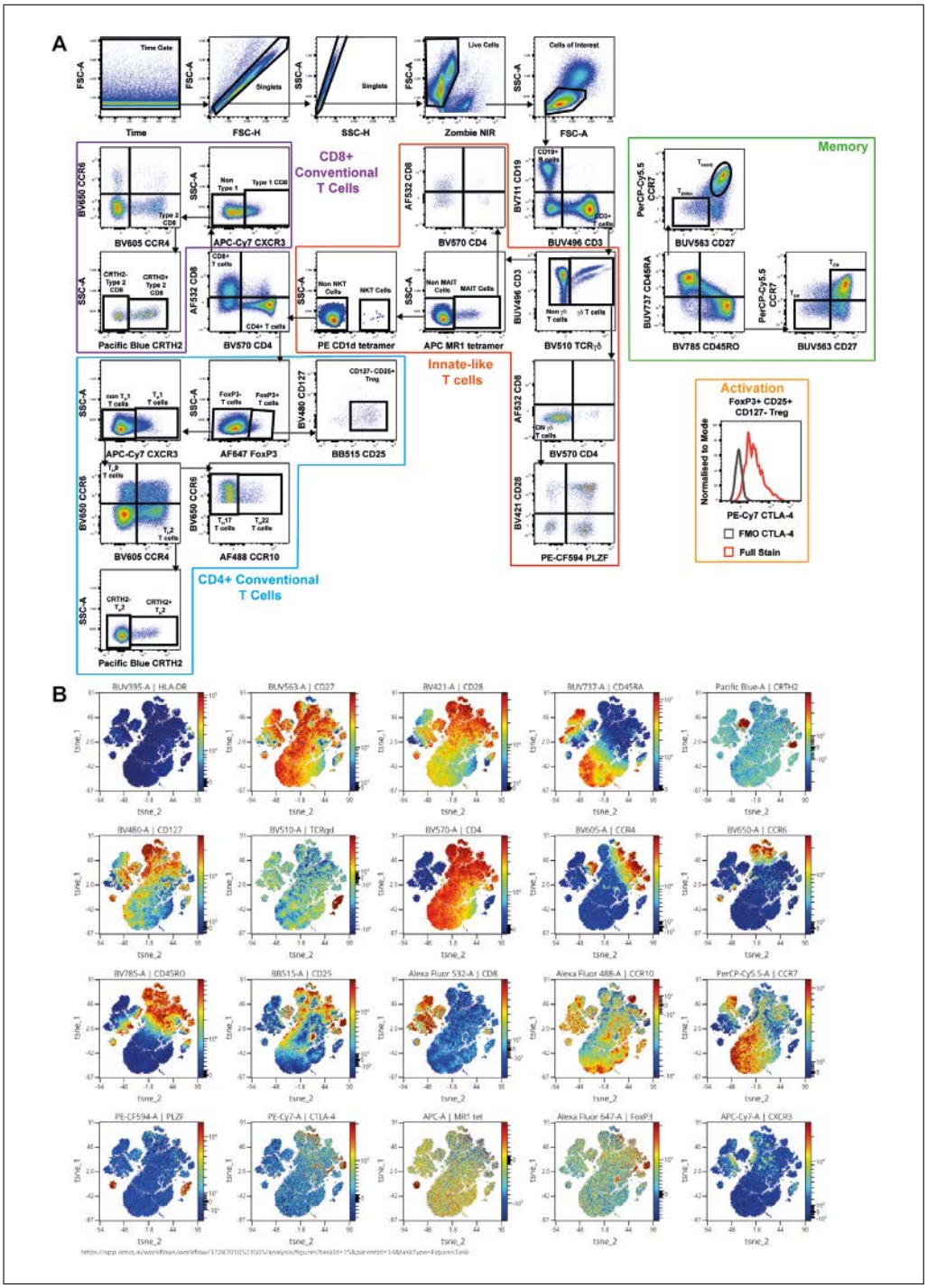

Figure 10 Gating of the FS sample. (**A**) Gating strategy of the panel, including lineage, memory, and activation readouts. (**B**) *t*-SNE as a quality control tool. *t*-SNE analysis was performed with 1000 iterations and perplexity of 30 and displayed in 2D plots using the resultant *t*-SNE 1 and *t*-SNE 2 dimensions according to the per cell expression of 20 proteins. Expression levels of HLA-DR, CD27, CD28, CD45RA, CRTH2, CD127, TCR$\gamma\delta$, CD4, CCR4, CCR6, CD45RO, CD25, CCR10, CD8, CCR7, PLZF, CTLA-4, MR1tet, FoxP3, and CXCR3 are displayed. *t*-SNE scales are shown in each graph and visualized using a rainbow heat scale.

8. Assess marker co-localization one by one in viSNE plots by coloring the *t*-SNE based on the expression of each marker (Fig. 10B).

viSNE is a visualization tool for high-dimensional single-cell data based on t-SNE.

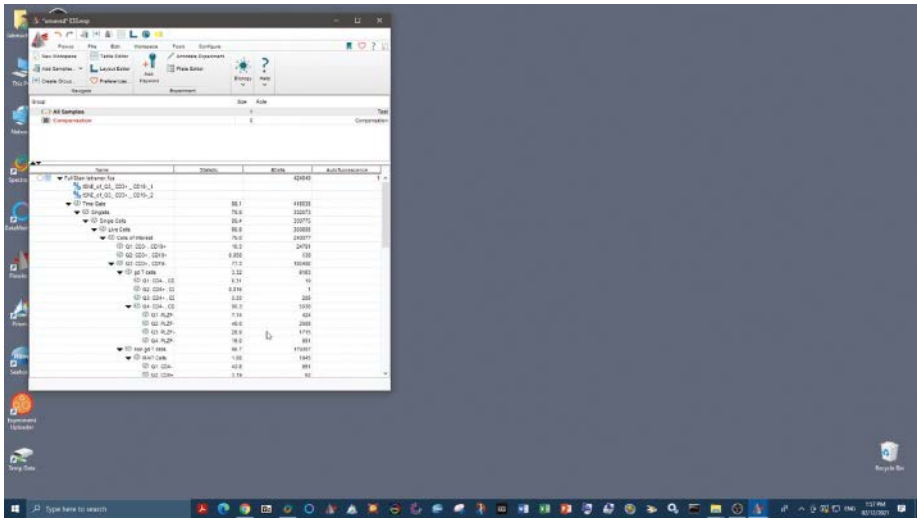

Video 6 Assessment of data quality using expert gating and dimensionality reduction algorithms (Basic Protocol 4).

9. As in step 4, check for the appearance of unexpected marker combinations on specific cell types.

See Figure 11 for a simple checklist to help ensure that all steps have been followed to obtain a high-quality and reliable immunophenotyping panel.

COMMENTARY

Background Information

The first step of building a successful large multicolor panel is good theoretical panel design. Full-spectrum flow cytometry panel design has been previously described (Ferrer-Font, Pellefigues, et al., 2020; Park et al., 2020). In summary, in the context of successful theoretical panel design, it is very important to have a clear experimental question and to know the biology of the markers that are included in the assay, including their expression and co-expression patterns. It is important to understand the instrument configuration (i.e., number of lasers on board) to know what the spectral signatures for each fluorophore will look like with the given configuration, as fluorophore brightness will vary depending on the excitation wavelength available. This information, coupled with the amount of spread (both given and received) of each fluorophore in the panel (detailed in Nguyen, Perfetto, Mahnke, Chattopadhyay, & Roederer, 2013), allows fluorophores to be optimally assigned to the different markers of the immunophenotyping panel.

After the panel has been theoretically designed, performance of QC steps is strongly recommended. This process is necessary to theoretically validate the panel before proceeding to a full experiment in order to reduce preventable issues as much as possible. It is advised to review the panel on a marker-by-marker and population-by-population basis, making sure that fluorophores inducing considerable amounts of spread (which could impair marker resolution) are allocated to non-co-expressed markers, and that dim markers receive a minimal amount of spread, while fluorophore brightness and antigen expression levels are well matched (high-expressing antigens with dim fluorophores and low-expressing antigens with bright fluorophores). To address potential issues, markers that are available with multiple fluorophores can be substituted to see if spillover spread can be minimized. Additionally, fluorophores that create (but do not receive) the most spillover can be designated to dump or viability channels. It is strongly recommended to complete panel optimization before working with an actual biological experiment, as it is a wise investment in terms of time, effort, and cost, without jeopardizing precious experimental samples.

Critical Parameters

Multiple factors influence the success of this protocol. The importance of good sample preparation—addressing sample

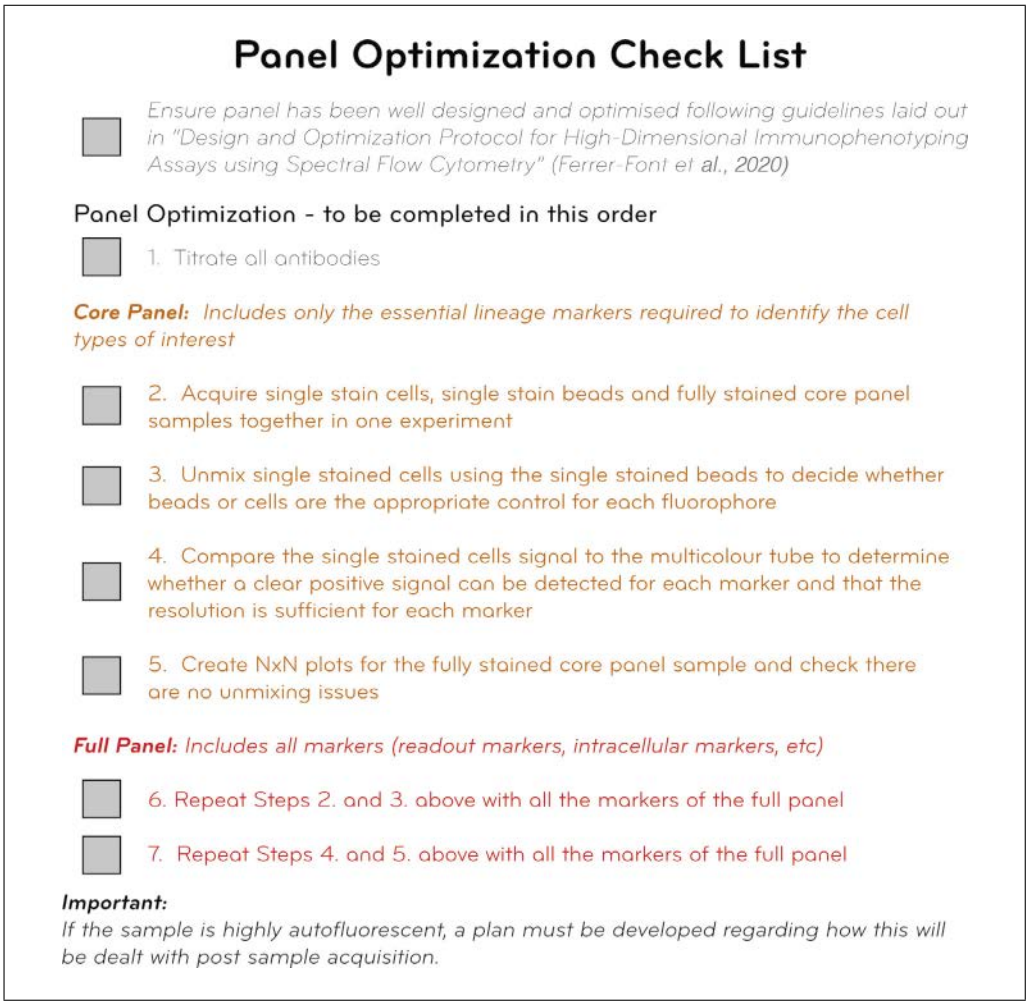

Figure 11 Panel optimization check list. To ensure the rigor and reproducibility of data acquired by spectral cytometry, the following steps are recommended for optimization and validation of each new panel.

complexity issues and the use of high-quality controls—must be emphasized.

Working with complex samples

When working with more complex samples than PBMCs (e.g., skin, tumor, fat tissue), the steps for panel optimization are the same, but there are some extra considerations.

Quality of single-cell suspension. An important consideration that is sometimes underestimated is the quality of the single-cell suspension that will be used to run the immunophenotyping panel. As different immune cell subsets have varying susceptibility to cell death, the single-cell suspension should have a viability of 80% or more to ensure proportional representation of the original sample (Costantini et al., 2003). Cell death can occur for different reasons, including how the sample has been treated before staining. Cryopreservation and harsh digestion protocols can affect sample quality and these procedures also need to be optimized. Indeed, when working with digested tissue, epitopes for the markers of interest should be verified to ensure the digestion protocol has not negatively impacted them. For example, if the same epitopes of interest exist in the spleen, one should compare marker staining and epitope preservation between digested and undigested spleen (Ferrer-Font, Mehta, et al., 2020).

Assessing instrument setup. Wherever possible, the instrument settings for fluorescence detector gains should remain unaltered from the Cytek Assay Settings (CAS). When using fluorescently labeled antibodies, this is achieved by carefully pairing expression levels to fluorophore brightness during panel design, and then by antibody titration to ensure fluorescence signals remain on-scale at the optimized settings. In certain applications where fluorescence intensity is not tunable, such as fluorescent reporter protein expression within

the cells of interest, the instrument settings may need to be adjusted to accommodate off-scale fluorescence signal. Any such change will impact not only the spectral signature being accommodated, but also other signatures with emission in the same area. Reducing fluorescence gains may lead to increased similarity between spectral signatures, which can give rise to more spillover spreading error and thus negatively impact marker resolution (Ferrer-Font, Pellefigues, et al., 2020). See Support Protocol 2 for steps required to alter fluorescence gain settings to accommodate off-scale signals. If using something other than the Cytek Aurora, it will be necessary to optimize the settings based on manufacturer's recommendations.

Autofluorescence. Samples with heterogeneous (Fig. 7C) or very bright homogeneous AF signatures (Fig. 7B) can make unmixing challenging. To improve the accuracy of the unmixing and to improve marker resolution in the case of heterogeneous AF samples, multiple AF reference controls can be created for each of the different AF signatures present in the sample (as if they were individual fluorophores included in the panel). The steps required for this process are divided in three sections called Discover, Distinguish and Designate. The goal is to Discover unique spectral signatures within the unstained control through use of a raw N × N plots; Distinguish these unique signatures into separate SRCs by exporting each population as a new FCS file which can then be reimported; and Designate each signature as unique fluorophores within the software to be unmixed as if they were part of the original panel. Care must be taken to ensure only clearly unique signatures (with similarity index <0.98) with at least 300 events of similar fluorescence intensity are distinguished to ensure high quality SRCs are generated (for a detailed protocol, see Support Protocol 3 and Video 4). For very bright homogeneous AF, the steps outlined in Basic Protocol 3 and Video 4 can be followed to improve unmixing and markers resolution outcomes.

Controls

The quality of controls will directly translate to the quality of unmixing and the data obtained. It is therefore worth investing the time to optimize them. It is of utmost importance to include all necessary controls from the beginning of a project. A complete overview about controls can be found in Maecker & Trotter (2006). Below is a summary of the categories of controls that should be considered when optimizing a flow cytometry panel.

Unstained controls. The unstained control is meant for AF assessment and should have a clean signature with no contamination from other fluorophores and match the tissue or sample type being analyzed. If, for example, different tissue types are used in an experiment, multiple unstained sample controls must be used for each tissue type. Similarly, if samples are being treated differently (e.g., fixed/fresh or stimulated/unstimulated), an unstained control should be included for each condition. It is not advised to mix samples from different conditions and collect only one unstained control, as it may not be possible to have enough events to generate clear AF signatures.

Spectral reference controls. Appropriate single-stained SRC samples are required for optimal unmixing of the fully stained sample. The purpose is to provide a signature of each fluorophore to be used by the unmixing algorithm. Briefly, SRCs should have positive and negative populations that are clearly separated or a universal negative; positive populations should be brighter than the fully stained sample; the negative and positive populations should have identical AF characteristics; sufficient events for both populations should be collected; and the fluorescence spectrum of the positive control needs to be identical to the one in the fully stained sample. To fulfill these best practices, cells and beads should be compared and the best option should be used. Special considerations for viability staining are important, as live and dead cells have different AF signatures, which means the positive and negative controls will not have the same AF signature. To overcome this issue, it is possible to kill all cells in the viability SRC (e.g., heat-killing at 55°-70°C for 5-10 min), stain only half of them, and mix these with the unstained cells. In this case, all the cells will be dead and the AF will be the same for the positive and negative controls.

SS cell controls. SS cell controls are used not only as reference controls but also to assess the performance of each marker compared to the FS tube. SS cells are gold-standard for each antibody performance and are used to quantify the spread of the negative population and/or shifts in the positive signal and thus any subsequent loss of resolution of markers in the panel.

Gating controls. A fluorescence minus one (FMO) control is a sample stained with all

fluorophores used in the experiment except one. Analyzing the FMO control for each fluorophore in the panel is not required for panel optimization, but FMOs can be used as a guide to set the boundary between positive and negative events if it is ambiguous. FMOs also aid in the assessment of spread between positive and negative events and are an important tool for assessing panel performance. A good alternative for large 20+ color spectral panels is the use of fluorescence minus multiple (FMM) controls, as recently described by Jensen & Wnek (2020).

Core versus FS panel

When optimizing a high-dimensional immunophenotyping panel, it is recommended to first complete Basic Protocols 1-4 with a *core panel.* A core panel is limited to only the essential lineage markers required to identify the cell types of interest. This will reduce confounding factors when attempting to understand the source of errors. Once a core panel has been optimized, additional markers can be added (including readout functional markers, intracellular markers, etc.) and optimized with the knowledge that issues are not originating from the core panel.

Fixation/permeabilization buffers

Intracellular staining procedures also require special consideration. It is important to source the fixation/permeabilization reagent that is most appropriate for the markers being detected (e.g., transcription factors, cytokines, or intracellular proteins) while also considering their relative locations (cytosolic or nuclear). The type of fixation buffer can influence the staining of both intracellular and surface markers. The type of fixative can have an impact in many aspects of staining: damaging the epitopes, altering the fluor stability and resulting in a different optimal titer, altering the background fluorescence without altering the positive signal (leading to reduced resolution between positive and negative populations), and altering the fluorescence spectral signatures (causing spectral signature mismatches between FS samples and SRCs, resulting in unmixing issues). It is recommended that antibodies be titrated using the same fixation/permeabilization buffer conditions used for the final staining of FS samples and SRCs.

Troubleshooting

The term troubleshooting is used when one or more issues are found in the panel and the source of these issues needs to be identified and steps included to rectify them. In this regard, the exact steps provided for validating the panel can also be applied for troubleshooting. By following these clear steps, the user will gain a better understanding of the quality of the panel and identify issues prior to acquiring experimental samples.

In general, 80%-90% of unmixing issues that arise can be traced to suboptimal controls. Therefore, it is important to use controls that are well characterized, high quality, and appropriate for the experiment (i.e., matched to the conditions of the experimental sample). This is particularly vital if they are going to be reused.

The checklist provided in Figure 11 aims to help users follow clear steps to optimize and troubleshoot their panels. By following these steps, users should be able to discover issues if they exist and have a pathway and alternatives to address and resolve them. Additional troubleshooting for general issues that may arise during panel optimization can be found in Tables 2-5.

Understanding Results

The example panel optimized using this protocol and presented here aims to identify conventional T cell subsets in peripheral blood of healthy participants. The participants were infected with low-dose human hookworm as part of a longitudinal study. It is well established that during early parasitic infection there is an increase in T-helper Type 2 immune responses (Th2) in the T cell compartments due to the primary role these cells play in host responses to parasites (McSorley & Loukas, 2010). However, the wider effects on the human immune system of long-term chronic parasitic infection with the gut-residing hookworm *Necator americanus (Na)* have not been investigated. Therefore, a panel was designed and optimized to look at the following conventional and unconventional T cell subsets of interest: $CD4^+$ T cells (Th1, Th2, Th17, Th9, Th22, and Tregs), $CD8^+$ T cells (Tc1 and Tc2), and innate-like T cells (γδ T, mucosal associate invariant T [MAIT], and natural killer T [NKT] cells). This panel can assess the frequency of these cell subsets as well as their memory and activation phenotypes, using both expert gating and high-dimensional data analysis.

Some characteristics of the fluorophore selection for a certain panel including the

Table 2 Troubleshooting for Preparation and Evaluation of Optimal SRCs (Basic Protocol 1)

Problem	Cause	Potential solution
Spectral signature of SRC does not match expected signature for fluorophore	Contamination of control with another fluorescent antibody	Preferably prepare new SRC; alternatively, in SpectroFlo software using the raw SRC, exclude the contaminating signature, export the clean file, and import this FCS file as the correct SRC
	Carryover from previous SRCs on the cytometer	Preferably prepare a new SRC; alternatively, in the SpectroFlo software using the raw SRC, exclude the contaminating signature, export the clean file and import this FCS file as the correct SRC
	Tandem dye degradation	Find the cause of degradation (issue with fixative, how long samples are stored in fixative, temperature of incubation, light exposure during protocol, etc.) and make necessary corrections (modifying staining procedure or buy a new vial)
	Brilliant Stain Buffer added to bead controls	Remake bead SRCs without addition of Brilliant Stain Buffer
	Wrong tube was recorded (signature matches different fluorophore)	Read the correct control or import the correct SRC FCS file
More than one spectral signature is visible	Autofluorescence signature	If positive and negative populations have the same secondary signature(s), this may be autofluorescence. See Basic Protocol 3 or Support Protocol 3 to decide on an approach for mitigating AF.
	Contamination of control with another fluorescent antibody	If there are multiple positive populations and gating on each one produces a distinct signature, then it is likely that there are two fluorophores in the SRC. Prepare a new SRC or exclude the signature of the contamination and import this FCS file as the correct SRC, if possible
Fluorescent signal in the negative population of the SRC	Nonspecific binding of antibody to negative beads	Revisit antibody titer to make sure the optimal titration is used; alternatively, use the universal negative feature in the software
	Inadequate sample preparation/wash procedure	Wash SRC controls well in the presence of excess wash solution such as FACS Staining Buffer (see Basic Protocol 1)
	Carryover of samples from previous SRC	Look at time vs. fluorescent signal, export a cleaned FCS file removing the contaminating signal, and import this FCS file as the correct SRC
Unmixing errors in SRCs	Gates were not set correctly in the Unmixing Wizard	Ensure that the P1 gate is set on the population with the highest expression of the marker. Place the positive histogram gate on the brightest signal (this may be different than gating on all positive signals). Better results can be obtained with tighter gates that do not include a side variety of cell sizes and/or fluorescence intensities.
	Contamination of control with another fluorescent antibody	Preferably prepare a new SRC; alternatively, in SpectroFlo software using the raw SRC, exclude the contaminating signature, export the clean file, and import this FCS file as the correct SRC

(*Continued*)

Table 2 Troubleshooting for Preparation and Evaluation of Optimal SRCs (Basic Protocol 1), *continued*

Problem	Cause	Potential solution
No positive signal can be detected	Gates were not set correctly in the Unmixing Wizard	Move P1 gate to population that expresses marker and/or move histogram to peak detector
	Not enough events were recorded	The unmixing algorithm requires a minimum of 300 positive events; record more total events
	Antibody was not added to SRC	Prepare new SRC

Table 3 Troubleshooting for Unmixing Evaluation of Fully Stained Sample (Basic Protocol 2)

Problem	Potential cause	Potential solution
Unmixing Wizard unmixes SRCs cells correctly, but unmixing errors are present in FS cells	SRCs are dimmer than fully stained sample	Use brighter SRCs; ensure staining protocol is exactly the same for SRCs and FS cells (antibody concentration, incubation time/temperature, use of fixative, stimulation of cells, etc.). Note that the optimal antibody concentration for compensation beads is often different than for cells. Pipetting error can easily occur when pipetting small volumes (<1-2 µl) for SRCs compared to using a master mix for FS samples. In this case, it is recommended to dilute antibodies to avoid pipetting small volumes. Other common mistakes include not using fix/perm buffer on compensation beads or using a tissue for SRCs that has lower marker expression than FS sample.
	Beads were used for all the SRCs and there may be a mismatch in the emission spectra between beads and cells	Use SRC stained cells instead.
	Polymer dyes (more than 2) are included in the panel without using Brilliant Stain Buffer or Super Bright Stain Buffer	Use Brilliant Stain Buffer when more than one polymer dye is added in the same tube following manufacturer recommendations.
	AF signature in FS sample is complex and different to the controls	Use AF extraction and see information regarding complex AF samples. Ensure the unstained control used for AF extraction is treated the same as the FS stained sample. AF signature may change with treatment (fixation, stimulation, timepoint, etc.). With human samples there may be patient-to-patient variability in AF signatures, so if using AF extraction for complex AF samples, an unstained control for each patient may be required. Also ensure that enough events are recorded in the unstained control to assess AF.
	Wrong tube was recorded (signature matches different fluorophore)	Read the correct control or import the correct SRC FCS file
Some FS samples unmixed correctly while others have unmixing errors	Biological variation; marker level of expression greatly changes across donors or across experimental conditions.	Try using beads as SRCs. If they are not optimal, use donor with the highest level of expression as control.

Table 4 Troubleshooting for Evaluation of Marker Resolution (Basic Protocol 3)

Problem	Potential cause	Potential solution
Low signal in certain markers (in FS and SS samples)	Marker expression too low or non-existent	Check that the marker is expected to be expressed on the particular cells or animal model of interest. Compare to Technical Data Sheet (TDS) or published literature.
	Experimental design (i.e., timepoint or stimulation) does not elicit certain markers	Stimulate cells with a positive control (e.g., PMC-ionomycin) to ensure cells are capable of expressing the markers of interest.
	Epitope is damaged by digestion procedure	Test different clone or modify digestion conditions
	Epitope is damaged by staining procedure	Test different clone or modify staining conditions
	Fluorophores chosen were too dim	Choose a brighter fluorophore for the specific marker and optimize concentration used
	Tandem dyes have degraded or decoupled	Find cause of degradation (issue with fixative, how long samples are stored in fixative, temperature of incubation, light exposure during protocol, etc.) and replace tandem dye with a new vial
FS sample stained less (lower MFI) than SS sample for a given marker	Binding site blocked by other reagents in the panel or different Ab/receptor binding kinetics	Test sequential staining, perform experiments to identify antibodies that are interfering with each other or try different clones
	Saturation is not achieved at optimal titer for SRCs	Increase titer to reach saturation
	Pipetting error when pipetting antibody cocktails	Repeat experiment to double-check
	Antibody/antibodies were trapped in the column when filtering the antibody cocktail	Optimize centrifuge spinning time and speed
Unstained, SS, and FS cells have high AF background	Cells of interest are highly autofluorescent	Extract autofluorescence
Suboptimal separation/resolution between negative and positive populations	Antibody concentration is too low or too high	Optimize antibody concentration based on antibody titration results
	Spread	Check SSM and use FMOs to confirm source of spread
	Unbound antibodies were not adequately washed from samples	Add additional centrifugation and FACS Staining Buffer wash step
	Viability dye concentration is too high and live cells are stained with dye	If live cells are stained with viability dye, the spreading error from the viability dye must be accounted for and this may cause problems with marker resolution. Ideally, viability dye should be titrated so that live cells do not stain with viability dye.

Table 5 Troubleshooting for Assessment of Data Quality (Basic Protocol 4)

Problem	Potential cause	Potential solution
Appearance of unexpected biological patterns	Inadequate cleaning gates	Make sure you are using time gates, excluding doublets, dead cells, and antibody aggregates, and gating on cells of interest
	Viability dye concentration is too high and live cells are stained with dye	Titrate viability dye to make sure the optimal concentration is used
	Lack of viability dye in panel and dead cells nonspecifically bind to antibodies	Titrate and add viability dye to FS samples
	Lack of addition of Brilliant Stain Buffer	Use Brilliant Stain Buffer when more than one polymer dye is added in the same tube following manufacturer recommendations

similarity and complexity indices of the panel (Fig. 12A) and the spectral signatures of fluorophores used (Fig. 12B) have been included. Although some fluorophores have a high similarity index, they have been allocated to different cell types and therefore the impact of the expected spreading error should be minimal (Fig. 12). A panel distribution table has also been included (Fig. 12C) to show the peak emission wavelengths for the fluorophores and markers assigned to the panel.

After following all the steps of Basic Protocols 1-4 for our panel shown here, and resolving any issues that arose (such as one tandem degradation or implementing the sequential staining for some of the markers), high-quality full-spectrum flow cytometry data as defined by clear resolution of all expected populations was achieved. The optimized staining protocol for this panel is detailed in the Supplementary Material. Sequential staining was applied, following the order given in the protocol, for markers that showed a reduction in positive signal in the FS compared to the SS control, starting at the marker with the greatest reduction and working toward the one with the least reduction. This approach provided satisfactory results and did not require the testing of other combinations. To reduce staining procedure time, further optimization would be required to determine whether some markers could be added at the same time instead of using all of them sequentially.

A clean and clear positive population can be detected for all markers in the panel, with no signal resolution loss when all antibodies are combined. In some cases, such as for the activation markers, the use of FMOs is necessary to assist in evaluating gates to determine positive staining with confidence. All populations of interest could be found using expert gating, and the populations resemble the expected expression patterns and frequencies. Additionally, high-dimensional data analysis algorithms were successfully used without the appearance of artefacts, confirming the high quality of the data.

Time Considerations

The time needed for designing, optimizing, and analyzing a high-dimensional flow cytometry panel can be highly variable and can depend on the assay complexity, number of markers, wait-time required for reagents (geographically dependent), sample access and frequency of sample delivery (particularly for patient samples), duration of the disease model being investigated, and more. As an example, it took five months to optimize the digestion, design, and optimization of a 23-color spectral flow cytometry panel in gut tissue (Ferret-Font, Mehta, et al., 2020), whereas one month may be sufficient for a PBMC panel where digestion does not need optimization. It is therefore advisable to develop certain core panels that can be applied to several experimental questions and models.

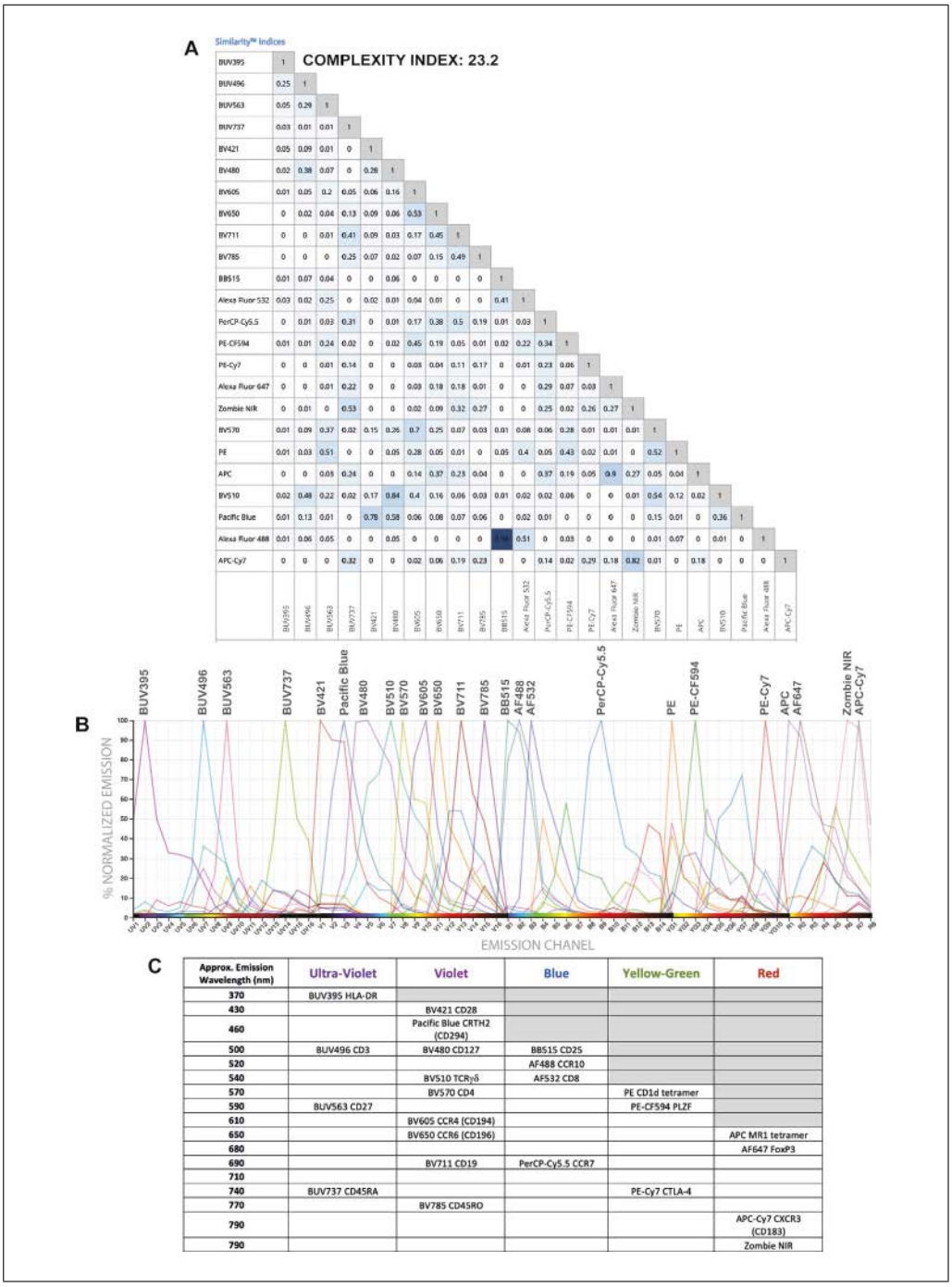

C

Approx. Emission Wavelength (nm)	Ultra-Violet	Violet	Blue	Yellow-Green	Red
370	BUV395 HLA-DR				
430		BV421 CD28			
460		Pacific Blue CRTH2 (CD294)			
500	BUV496 CD3	BV480 CD127	BB515 CD25		
520			AF488 CCR10		
540		BV510 TCRγδ	AF532 CD8		
570		BV570 CD4		PE CD1d tetramer	
590	BUV563 CD27			PE-CF594 PLZF	
610		BV605 CCR4 (CD194)			
650		BV650 CCR6 (CD196)			APC MR1 tetramer
680					AF647 FoxP3
690		BV711 CD19	PerCP-Cy5.5 CCR7		
710					
740	BUV737 CD45RA			PE-Cy7 CTLA-4	
770		BV785 CD45RO			
790					APC-Cy7 CXCR3 (CD183)
790					Zombie NIR

Figure 12 Theoretical panel design. (**A**) Similarity and complexity indices of fluorophores used in the final panel design. (**B**) Cytek Full Spectrum Viewer readout showing the fluorescence signatures of all fluorophores used in the panel, using the 5L Aurora configuration. (**C**) Panel distribution table showing peak emission wavelengths for markers and fluorophores in the panel.

Acknowledgments

This work was enabled by the Hugh Green Cytometry Centre at the Malaghan Institute of Medical Research. We wish to thank the Hugh Green Foundation, the Marjorie Barclay Trust, the Dinies Foundation and the HRC Independent Research Organisation (18/1003) for funding this study. We are also very grateful to the NIH Core Tetramer Facility for supplying the tetramers used in this panel and to Olivia Burn and Kathryn Hally for feedback on the manuscript.

Author Contributions

Laura Ferrer-Font: Conceptualization; investigation; methodology; project administration; writing–original draft; **Sam J. Small:** Investigation; methodology;

writing–original draft; **Brittany Lewer:** Investigation; writing–review & editing; **Katherine R Pilkington:** Resources; writing–review & editing; **Laura K. Johnston:** Writing–review & editing; **Lily M. Park:** Writing–review & editing; **Joanne Lannigan:** Methodology; writing–review & editing; **Maria C. Jaimes:** Conceptualization; methodology; resources; supervision; writing–review & editing; **Kylie M. Price:** Funding acquisition; project administration; supervision; writing–review & editing.

Conflicts of Interest

Kate Pilkington, Lily Park, Maria C. Jaimes are employees of Cytek Biosciences, Inc., the manufacturer of the Aurora full-spectrum flow cytometer used in these studies. Joanne Lannigan is a paid consultant for Cytek Biosciences, Inc.

Data Availability Statement

Data available on request due to privacy/ethical restrictions.

Literature Cited

Aass, H. C. D., Øvstebø, R., Trøseid, A. M. S., Kierulf, P., Berg, J. P., & Henriksson, C. E. (2011). Fluorescent particles in the antibody solution result in false TF- and CD14-positive microparticles in flow cytometric analysis. *Cytometry Part A*, *79 A*, 990–999. doi: 10.1002/cyto.a.21147.

Ashhurst, T. M., Smith, A. L., & King, N. J. C. (2017). High-dimensional fluorescence cytometry. *Current Protocols in Immunology*, *2017*, 5.8.1–5.8.38. doi: 10.1002/cpim.37.

Ayers, L., Kohler, M., Harrison, P., Sargent, I., Dragovic, R., Schaap, M., … Ferry, B. (2011). Measurement of circulating cell-derived microparticles by flow cytometry: Sources of variability within the assay. *Thrombosis Research*, *127*, 370–377. doi: 10.1016/j.thromres.2010.12.014.

Brummelman, J., Haftmann, C., Núñez, N. G., Alvisi, G., Mazza, E. M. C., Becher, B., & Lugli, E. (2019). Development, application and computational analysis of high-dimensional fluorescent antibody panels for single-cell flow cytometry. *Nature Protocols*, *14*, 1946–1969. doi: 10.1038/s41596-019-0166-2.

Costantini, A., Mancini, S., Giuliodoro, S., Butini, L., Regnery, C. M., Silvestri, G., & Montroni, M. (2003). Effects of cryopreservation on lymphocyte immunophenotype and function. *Journal of Immunological Methods*, *278*, 145–155. doi: 10.1016/S0022-1759(03)00202-3.

Disis, M., dela Rosa, C., Goodell, V., & Ling-Yu, K. (2006). Maximizing the retention of antigen specific lymphocyte function after cryopreservation. *Journal of Immunological Methods*, *308*, 13–18. doi: 10.1016/J.JIM.2005.09.011.

Feher, K., von Volkmann, K., Kirsch, J., Radbruch, A., Popien, J., & Kaiser, T. (2016). Multispectral flow cytometry: The consequences of increased light collection. *Cytometry Part A*, *89*, 681–689. doi: 10.1002/cyto.a.22888.

Ferrer-Font, L., Mehta, P., Harmos, P., Schmidt, A. J., Chappell, S., Price, K. M., … Mayer, J. U. (2020). High-dimensional analysis of intestinal immune cells during helminth infection. *eLife*, *9*, e51678. doi: 10.7554/eLife.51678.

Ferrer-Font, L., Pellefigues, C., Mayer, J. U., Small, S. J., Jaimes, M. C., & Price, K. M. (2020). Panel design and optimization for high-dimensional immunophenotyping assays using spectral flow cytometry. *Current Protocols in Cytometry*, *92*, 1–25. doi: 10.1002/cpcy.70.

Inglis, H. C., Danesh, A., Shah, A., Lacroix, J., Spinella, P. C., & Norris, P. J. (2015). Techniques to improve detection and analysis of extracellular vesicles using flow cytometry. *Cytometry Part A*, *87*, 1052–1063. doi: 10.1002/cyto.a.22649.

Jalbert, E., Shikuma, C. M., Ndhlovu, L. C., & Barbour, J. D. (2013). Sequential staining improves detection of CCR2 and CX3CR1 on monocytes when simultaneously evaluating CCR5 by multicolor flow cytometry. *Cytometry Part A*, *83 A*, 280–286. doi: 10.1002/cyto.a.22257.

Jensen, H. A., & Wnek, R. (2020). Analytical performance of a 25-marker spectral cytometry immune monitoring assay in peripheral blood. *Cytometry Part A*, *99*(2), 180-193. doi: 10.1002/cyto.a.24290.

Maecker, H. T., & Trotter, J. (2006). Flow cytometry controls, instrument setup, and the determination of positivity. *Cytometry Part A*, *69*, 1037–1042. doi: 10.1002/cyto.a.20333.

Mayeno, A. N., Hamann, K. J., & Gleich, G. J. (1992). Granule-associated flavin adenine dinucleotide (FAD) is responsible for eosinophil autofluorescence. *Journal of Leukocyte Biology*, *51*, 172–175. doi: 10.1002/jlb.51.2.172.

McSorley, H. J., & Loukas, A. (2010). The immunology of human hookworm infections. *Parasite Immunology*, *32*, 549–559. doi: 10.1111/j.1365-3024.2010.01224.x.

Nguyen, R., Perfetto, S., Mahnke, Y. D., Chattopadhyay, P., & Roederer, M. (2013). Quantifying spillover spreading for comparing instrument performance and aiding in multicolor panel design. *Cytometry Part A*, *83 A*, 306–315. doi: 10.1002/cyto.a.22251.

Park, L. M., Lannigan, J., & Jaimes, M. C. (2020). OMIP-069: Forty-color full spectrum flow cytometry panel for deep immunophenotyping of major cell subsets in human peripheral blood. *Cytometry Part A*, *97*, 1044–1051. doi: 10.1002/cyto.a.22251.

Petriz, J., Bradford, J. A., & Ward, M. D. (2018). No lyse no wash flow cytometry for maximizing minimal sample preparation. *Methods*, *134–135*, 149–163. doi: 10.1016/j.ymeth.2017.12.012.

Roederer, M. (2016). Distributions of autofluorescence after compensation: Be panglossian, fret not. *Cytometry Part A*, *89*, 398–402. doi: 10.1002/cyto.a.22820.

Sahir, F., Mateo, J. M., Steinhoff, M., & Siveen, K. S. (2020). Development of a 43 color panel for the characterization of conventional and unconventional T-cell subsets, B cells, NK cells, monocytes, dendritic cells, and innate lymphoid cells using spectral flow cytometry. *Cytometry Part A*, 2020, Dec 18. doi: 10.1002/cyto.a.24288.

Schmutz, S., Valente, M., Cumano, A., & Novault, S. (2016). Spectral cytometry has unique properties allowing multicolor analysis of cell suspensions isolated from solid tissues. *PLoS One*, *11*, e0159961. doi: 10.1371/journal.pone.0159961.

Shi, L., Lu, L., Harvey, G., Harvey, T., Rodríguez-Contreras, A., & Alfano, R. R. (2017). Label-free fluorescence spectroscopy for detecting key biomolecules in brain tissue from a mouse model of Alzheimer's disease. *Scientific Reports*, *7*, 1–7. doi: 10.1038/s41598-017-02673-5.

Stewart, C. C., & Stewart, S. J. (1997). Titering antibodies. *Current Protocols in Cytometry*, *00(*1*)*, 4.1.1–4.1.13. doi: 10.1002/0471142956.cy0401s14.

van der Maaten, L., & Hinton, G. (2008). Visualizing data using t-SNE. *Journal of Machine Learning Research*, *9*, 2579–2605.

van der Vlist, E. J., Nolte-'t Hoen, E. N. M., Stoorvogel, W., Arkesteijn, G. J. A., & Wauben, M. H. M. (2012). Fluorescent labeling of nano-sized vesicles released by cells and subsequent quantitative and qualitative analysis by high-resolution flow cytometry. *Nature Protocols*, *7*, 1311–1326. doi: 10.1038/nprot.2012.065.

ORIGINAL ARTICLE

MIFlowCyt

ISAC CYTOMETRY Journal of Quantitative Cell Science PART A

Analytical performance of a 25-marker spectral cytometry immune monitoring assay in peripheral blood

Holly A. Jensen | **Richard Wnek**

Translational Molecular Biomarkers, Merck & Co., Inc, Kenilworth, New Jersey

Correspondence
Richard Wnek, Translational Molecular Biomarkers, Merck & Co., Inc., Building K15, Kenilworth, NJ 07033.
Email: richard.wnek@merck.com

Abstract

Herein, we describe the development and analytical performance characteristics of a spectral flow cytometry assay for longitudinal immune monitoring biomarker applications in human whole blood and/or peripheral blood mononuclear cells (PBMCs). This 25 immune biomarker panel and robust gating strategy, developed in normal healthy volunteers, resolves memory, polarization, and activation markers on T, B, and NK cells as well as myeloid subpopulations including monocytes, dendritic cells, neutrophils, basophils, and myeloid-derived suppressor cells (MDSCs). Three associated fluorescence-minus-multiple (FMM) designs are proposed as gating controls. To our knowledge, this is the first report to investigate intra-run precision, post collection whole blood stability, and the impact of PBMC processing in the context of spectral cytometry. We achieved high intra-run sample precision (<20% CV) for >95% of all gated immune cell populations analyzed across biospecimen types. Additionally, we explored the application of FlowSOM analysis and resulting impact on assay precision metrics. We observed biomarker stability in blood out to 24 h (86%), 48 h (83%), and 72 h (76%) while highlighting select markers (i.e., CXCR3) and rare cell subsets (i.e., naïve Tregs, plasmacytoid DCs, MDSCs) affected by storage and/or PBMC manipulation. Interrogation of sample type is imperative to coherent application of immune monitoring assays. Overall based on analytical performance, this 25-biomarker spectral cytometry assay is sufficiently robust for implementation in translational research settings.

KEYWORDS
assay precision, blood stability, Cytek Aurora, immune monitoring, immunophenotyping, PMBC, spectral cytometry

1 | INTRODUCTION

There is a growing need for advanced cytometric biomarker analysis during clinical development, particularly in the field of immunology and immune-oncology where focused biomarker testing and longitudinal patient monitoring are increasingly performed. Investigating immune population correlates in blood offers an overall measure of systemic immune fitness and obviates challenging tissue collection requirements. However, achieving highly granular, fluorescence-based 20+ immunophenotyping biomarker information from a single-stained patient sample remains a challenge. Feasible and reproducible assay performance often constrains conventional flow cytometry panel design, prompting biomarker distribution across several smaller panels. Examples include the five 8-color panels developed by Human Immune Phenotyping Consortium [1], six 9-color panels developed by Ivison et al. for standardized multicenter testing [2], and 12 individual 10-color panels developed by Pitoiset et al. to collectively capture 70 different biomarkers [3]. Although standardized mass cytometry assays (potentially capable of 50+ biomarker evaluation) have been developed for clinical immune monitoring of peripheral blood [4], batch effects and slower sample run times are limiting to broader adoption in translational research settings.

To improve reagent, sample resource and processing efficiency, we explored panel design on the Cytek Aurora spectral cytometry platform. The advantages of spectral cytometry [5], spectral unmixing [6], and guidance on spectral cytometry panel design [7] have been reported elsewhere. We aimed for a 25-biomarker immune monitoring panel, using OMIP-042 [8] as a starting point while referencing major immunophenotypes described by the Human Immune Phenotyping Consortium [1], OMIP-034 [9], and OMIP-056 [10]. Ultimately, we reviewed over 45 OMIPs and immune panels published within the last decade. The most common immune surface markers are included (CD3, CD4, CD8, CD14, CCR7, CD19, CD45RA, CD16, CD127, CD27, HLADR, CD56, CD38, and CD25) in addition to markers for CD4 T helper subsets (CXCR3, CCR6, and CCR4) and dendritic cells (CD11c and CD123). CD45 is included to distinguish leukocytes from residual red blood cells or debris, and a live/dead marker when staining cryopreserved PBMCs. Also, individuals with disease may exhibit an expanded compartment of myeloid-derived suppressor cells (MDSCs) [11]. Although a true MDSC biomarker remains elusive, common MDSC gating strategies include CD33, CD15, and CD11b [12,13]. Finally, we incorporated the terminal effector marker KLRG1 [14]. Antibody reagent titrations and fluorophore stability are detailed. A robust, hierarchical gating strategy is provided with additional guidance on fluorescence-minus-multiple (FMM) controls. This panel design exercise was expanded to include characterization of analytical performance. Blood sample stability, intra-run precision and population changes after PBMC isolation or cryopreservation are evaluated using peripheral blood from healthy volunteers. Finally, we compare our manual gating scheme to FlowSOM analysis toward objective population identification and improved assay precision analysis.

2 | MATERIALS AND METHODS

2.1 | Whole blood preparation

Peripheral blood from healthy donors was obtained using our company's Volunteer Donation Program in accordance with institutional regulations. For red blood cell (RBC) lysis, 3 ml of donor blood collected in Na-Heparin tubes was mixed with 7 ml of 1X BD Pharm Lyse (BD, Franklin Lakes, NJ) and incubated at room temperature for 15 min. RBC-lysed blood was centrifuged at 350*g* for 5 min. Leukocyte pellets were resuspended in an additional 7 ml of 1X BD Pharm Lyse and incubated at room temperature for 10 min. RBC-lysed blood was spun at 350*g* for 5 min. Leukocyte pellets were resuspended in 1 ml of BD Stain Buffer (BD, Franklin Lakes) such that 30 µl resuspended leukocytes equates to ~100 µl nonconcentrated blood.

2.2 | PBMC isolation, cryopreservation, and thawing

Donor blood (10 ml) collected in Na-Heparin tubes were mixed 1:1 with PBS and transferred to 50 ml Accuspin tubes (Millipore Sigma, MO) containing 15 ml of room temperature Histopaque-1077 (Millipore Sigma) below the frit. Accuspin tubes were centrifuged at 800*g* for 20 min with no brake. Contents above the frit were transferred to a 50 ml tube and the volume brought to 35 ml with PBS. Following centrifugation at 350*g* for 10 min, cell pellets were resuspended in 35 ml of PBS and centrifuged a second time at 350*g* for 10 min. Cell pellets were resuspended in 3 ml of BD stain buffer such that 30 µl equates to ~100,000 PBMC cells. For cryopreservation, cell pellets were resuspended in 1 ml of freezing medium (90% FBS, 10% DMSO) and stored at −80°C. To thaw cryopreserved PBMCs, vials were quickly warmed using a 37°C water bath. Thawed samples were pipetted drop by drop into warmed (37°C) X-VIVO 15 cell culture media (Lonza, Basel, Switzerland) containing 10% FBS and 1% Pen/Strep. Post-thaw viability typically exceeded 80%. PBMCs were centrifuged at 350*g* for 10 min and cell pellets were resuspended in BD Stain buffer such that 30 µl ~100,000–300,000 cells.

2.3 | Full panel stain

Samples containing 200,000 cells (PBMCs) or 200 µl of RBC-lysed blood (60 µl resuspended sample) were treated with 10 µg/ml Fc block (BD, Franklin Lakes) for 10 min at room temperature. Separately, antibody dilutions (antibody reagents are reported in Figure 1(A)) were prepared in BD Stain buffer such that 5–6 µl are required per test. Antibodies were combined into a cocktail in BD Falcon tubes. The Fc-blocked sample cells were added to the antibody mix and incubated for 1 h at 4°C in the dark. After incubation, 400 µl of PBS was added and samples were centrifuged at 350*g* for 5 min. Cell pellets were resuspended in either 300 µl PBS (for immediate analysis) or in 100 µl of 1:2000 Zombie NIR in PBS. If adding Zombie NIR, samples were incubated for 20 min at room temperature, then 400 µl of BD stain buffer was added and samples centrifuged at 350*g* for 5 min. Cell pellets were then resuspended in 300 µl PBS for analysis. All reference controls were acquired using AbC and ArC compensation beads (ThermoFisher, Waltham, NA) prepared following the manufacturer's instructions. The same beads were used to assess reagent stability for each fluorescently conjugated antibody at 0, 10, 20, and 35 days. For acquisition, we recommend collecting at least 10,000 non-debris events for titration data and 25,000+ non-debris events for full panel/FMM stains. Samples were run in duplicate or triplicate. We acquired the entire sample from each tube on a Cytek Aurora with 4-laser (V16-B14-YG10-R8) or upgraded 5-laser (UV16-V16-B14-YG10-R8) fixed configuration using CAS (Cytek Assay Settings). Daily QC was performed to maintain instrument performance.

2.4 | Data analysis

Flow cytometry data were visualized and gated in FCS Express 7 (De Novo Software, Pasadena, CA) and tabulated values were graphed in Prism 7 (GraphPad Software, San Diego, CA). Tables were

(A)

Cytek Aurora		Antibody Panel Reagents					Titration Results	Reagent Stability Cosine Similarity Index		
Laser	Detector	Marker	Clone	Fluorophore	Vendor	Catalog No.	µl per test	Day 10	Day 20	Day 35
405 nm	V1	KLRG1	SA231A2	BV421	Biolegend	367705	0.3	0.99997	0.99996	0.9999
405 nm	V3	CD4	SK3	Pacific Blue	Biolegend	344620	0.6	0.99985	0.99975	0.99968
405 nm	V4	CD19	SJ25C1	BV480	BD	566164	1.25	0.99994	0.99994	0.99991
405 nm	V5	CD33	WM53	BV510	Bioelgend	303421	0.3	0.99918	0.9998	0.99952
405 nm	V7	CD14	Tuk4	Pacific Orange	Invitrogen	MHCD1430	0.6	0.99958	0.99979	0.99946
405 nm	V8	CD8	RPA-T8	BV570	Biolegend	301037	0.6	0.99967	0.9992	0.99965
405 nm	V10	CCR4	L291H4	BV605	Biolegend	359418	1.25	0.99975	0.99934	0.99977
405 nm	V11	CD11b	ICRF44	BV650	Biolegend	301336	0.3	0.99988	0.99975	0.9995
405 nm	V13	CD25	2A3	BV711	BD	563159	1.25	0.9995	0.99985	0.99895
405 nm	V14	CD56	5.1H11	BV750	Biolegend	362555	0.6	0.9999	0.99994	0.99986
405 nm	V15	CCR6	G034	BV785	Biolegend	353422	0.6	0.99997	0.99994	0.99992
488 nm	B1	CD3	UCHT1	Alexa Fluor 488	BD	557694	0.3	0.99991	0.99994	0.99983
488 nm	B1	CD15	HI98	Alexa Fluor 488	Biolegend	301910	0.3	n/a	n/a	n/a
488 nm	B3	CD45	HI30	Alexa Fluor 532	eBioscience	58-0459-41	0.6	n/a	0.99831	0.9976
488 nm	B9	CD45RA	HI100	PerCP-Cy5.5	BD	563429	0.3	0.99953	0.99949	0.99933
488 nm	B10	CD16	3G8	PerCP-eF710	eBioscience	46-0168-42	0.6	0.99958	0.99908	0.999
561 nm	YG1	CXCR3	G025H7	PE	Biolegend	353705	0.6	0.99946	0.99933	0.99948
561 nm	YG3	CCR7	150503	PE-CF594	BD	562381	1.25	0.99957	0.99961	0.99927
561 nm	YG5	CD11c	Bly6	PE-Cy5	BD	551077	1.25	0.99971	0.99943	0.99933
561 nm	YG9	CD123	6H6	PE-Cy7	Biolegend	306009	0.3	0.99978	0.99916	0.99915
640 nm	R1	CD127	A019D5	APC	Biolegend	351315	0.6	0.99915	0.99929	0.99904
640 nm	R2	HLA-DR	L243	Alexa Fluor 647	Biolegend	307621	0.3	0.9999	0.99992	0.99983
640 nm	R4	CD27	O323	Alexa Fluor 700	Biolegend	302813	1.25	0.99941	0.9997	0.99969
640 nm	R6	Live/Dead	--	Zombie NIR	Biolegend	423105	1:2000	n/a	n/a	n/a
640 nm	R7	CD38	HIT2	APC-Fire 750	Biolegend	303545	0.6	0.9984	0.9986	0.99874

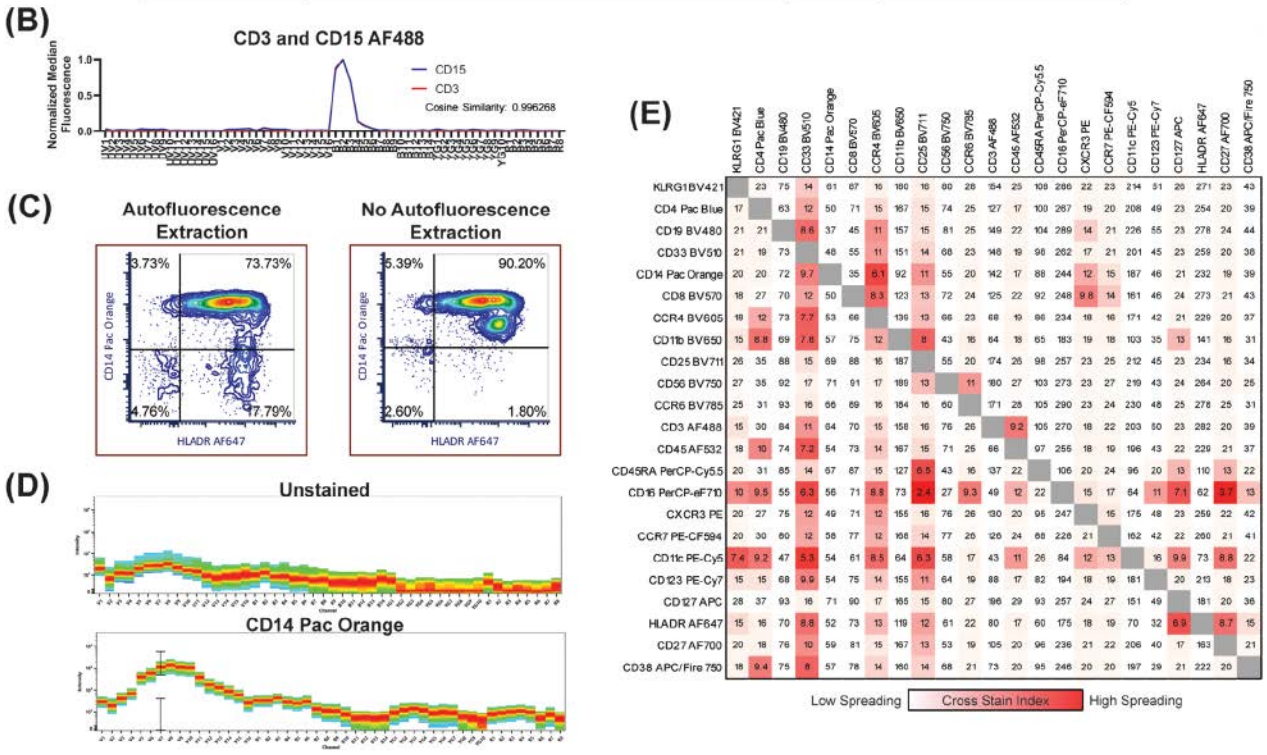

FIGURE 1 Single reagent and panel performance. (A) The reagent table details excitation laser, detector channel, target marker, antibody clone, conjugated fluorophore, vender and catalog number, titrated concentration, and reagent stability (normalized cosine similarity) after 10, 20, and 35 days of storage at 4°C. Final reagent test concentrations were selected based on saturating or near-saturating signal for the positive population, reduced spread of the negative population, and reduced reagent volume (see Figure S2). All cosine similarities are >0.99 and graphical data are reported in Figure S3. (B) Spectral plots for CD3 Alexa Fluor 488 (AF488) and CD15 AF488 are overlaid and have a normalized cosine similarity >0.99. (C) Autofluorescence extraction is required for correct unmixing of CD14 (left bivariate plot), otherwise CD14- cells appear as CD14lo (right plot). (D) Comparing the spectral profiles of unstained cells (top profile) and CD14 Pacific Orange (bottom plot), the phenomenon seen in (C)is likely due to similar profiles. A lack of autofluorescence extraction drives background signal to contribute to CD14 estimation. (E) We calculated Cross Stain Index (CSI), a measure developed by Cytek that is similar to Stain Index and gives a better estimation of spillover spreading effects on the Aurora platform. We used single-stained cell-based controls and found that there are minimal regions of strong spillover spreading (i.e., low CSI). For this panel, low CSI values occur between fluorophores that are not assigned to strongly co-expressed markers. Special thanks to Alex Wendling for sharing his FCS Express template for generating CSI matrices

generated in Microsoft Excel (Microsoft, Redwood WA) and all figures were built in Adobe Illustrator (San Jose, CA). Normalized cosine similarity and precision calculations (% CV, coefficient of variation) were performed in Microsoft Excel. Two-way ANOVA statistical analysis and linear regression (R^2) were performed in Prism 7. tSNE analysis on monocyte subsets was performed in FCS Express 7. tSNE and FlowSOM analyses on low-density (non-granulocyte) cells were performed in Cytobank (Beckman Coulter, Brea, CA). tSNE was run using standard inputs (perplexity = 30, iterations = 1000) and using all channels excepting FSC, SSC, autofluorescence, and CD45 AF532 for analysis. FlowSOM (metaclusters = 15, clusters = 100, iterations = 1000) was performed using proportional sampling and sample normalization.

3 | RESULTS

3.1 | Panel design and reagents

3.1.1 | Panel design

The 25-biomarker panel was optimized for use on a Cytek Aurora spectral flow cytometry platform with a 4-laser (V16-B14-YG10-R8) fixed configuration (Figure 1(A)). The avalanche photodiode detector (APD) modules provide near-contiguous coverage of all emitted wavelengths. Several fluorophores selected are challenging to employ concurrently on a traditional flow cytometry system, due to spillover or shared filter sets. These include Pacific Blue and BV480, Pacific Orange and BV570, BV750 and BV785, AF488 and AF532, PerCP-Cy5,5 and PerCP-e710, APC and AF647, and Zombie NIR and APC/Fire 750. However, these fluorophore pairs have distinct spectral signatures (Figure S1). Significant consideration went into understanding the co-expression of markers [15] during the fluorophore-assignment process. A brief account of the panel design workflow can be found in Supplementary Note S1.

3.1.2 | Reagent stability and titration

The Cytek Aurora software (SpectroFlo) enables storage of single stain reference control data which are adjusted daily to reflect instrument QC updates. However, unchecked fluorophore degradation can cause disparity between samples and prerecorded single stain spectral profiles. We tracked the stability of each fluorescently-conjugated reagent after 10, 20, and 35 days (Figure S3) and assessed longitudinal changes in spectral profiles using normalized cosine similarity (Figure 1(A)). Additionally, CD3 and CD15 (both assigned to Alexa Fluor 488) have identical spectral signatures (Figure 1(B)) and only require one reference control for spectral unmixing. Overall, these antibody reagents, including those with tandem fluorophores, are highly stable (normalized cosine similarity >0.99) over a span of 35 days, suggesting minimal to no impact on fluorophore integrity when stored properly at 4°C. We also observed little-to-no change in these reagent spectral profiles for as long as 3 months (data not shown). However, these findings may represent reagent-specific stability. Fluorescently conjugated antibody reagents should be individually assessed, and reference controls must be updated in the software regularly to ensure proper unmixing. Additionally, autofluorescence extraction must be included to correctly identify CD14+ populations (Figure 1(C)). Here, the spectral profile of CD14 Pacific Orange closely mimics that of unstained cells (Figure 1(D)). Without autofluorescence extraction, the autofluorescence profile can drive the unmixing algorithm to identify CD14- cells as CD14lo (Figure 1(C)). All fluorescently conjugated antibody reagents were titrated using healthy donor peripheral blood mononuclear cells (PBMCs). Optimized reagent concentrations reported in Figure 1(A) reflect titration data reported in Figure S2.

3.1.3 | Cross Stain Index

While single stain similarity measures interrogate reagent quality, other criteria are needed to assess panel performance. Cross Stain Index (CSI) is a measure presented by Cytek that better captures the mutual impact of fluorophores than traditional measures like spillover spreading or resolution impact. Like stain index, CSI uses normalization to the negative population, but when a secondary fluorophore is present. Thus, CSI reflects the ability to distinguish double-positives from their respective negatives. We assessed the quality of our panel design using a CSI matrix (Figure 1(E)) and, unsurprisingly, found negative impact on well-known areas of overlap, such as APC and Alexa Fluor 647. Due to thoughtful panel design, placement of mutually exclusive markers on regions of greatest concern had already been achieved. CD33 BV510 is the most heavily impacted reagent in this panel, but this had minimal impact on our gating strategy.

3.2 | Hierarchical gating strategy

We focused heavily on establishing a robust gating strategy (Figure 2). Multiple hierarchical gating schemes from pan-leukocyte panel designs were referenced, including OMIP-023, OMIP-042, OMIP-034, OMIP-044, OMIP-056, a CyTOF gating strategy [4], standardized gating by the HIPC [1], and other sources. Poor upstream gating on scatter plots (i.e., gating based on morphological characteristics, see Figure S4) can lead to gating errors and drive high % CV values of downstream populations. A comprehensive legend of the gating scheme with detailed population descriptions is provided (Figure 3).

3.2.1 | High- and Low-density cells

We focused here on gating peripheral whole blood samples (Figure 2 (B)), but a similar strategy can be applied to fresh or cryopreserved PBMC, with removal of granulocyte gating and addition of upstream live/dead gating (Figure 2(A)). Following debris, doublet and CD45-exclusion, a SSC versus CD3+CD15+ bivariate plot consistently

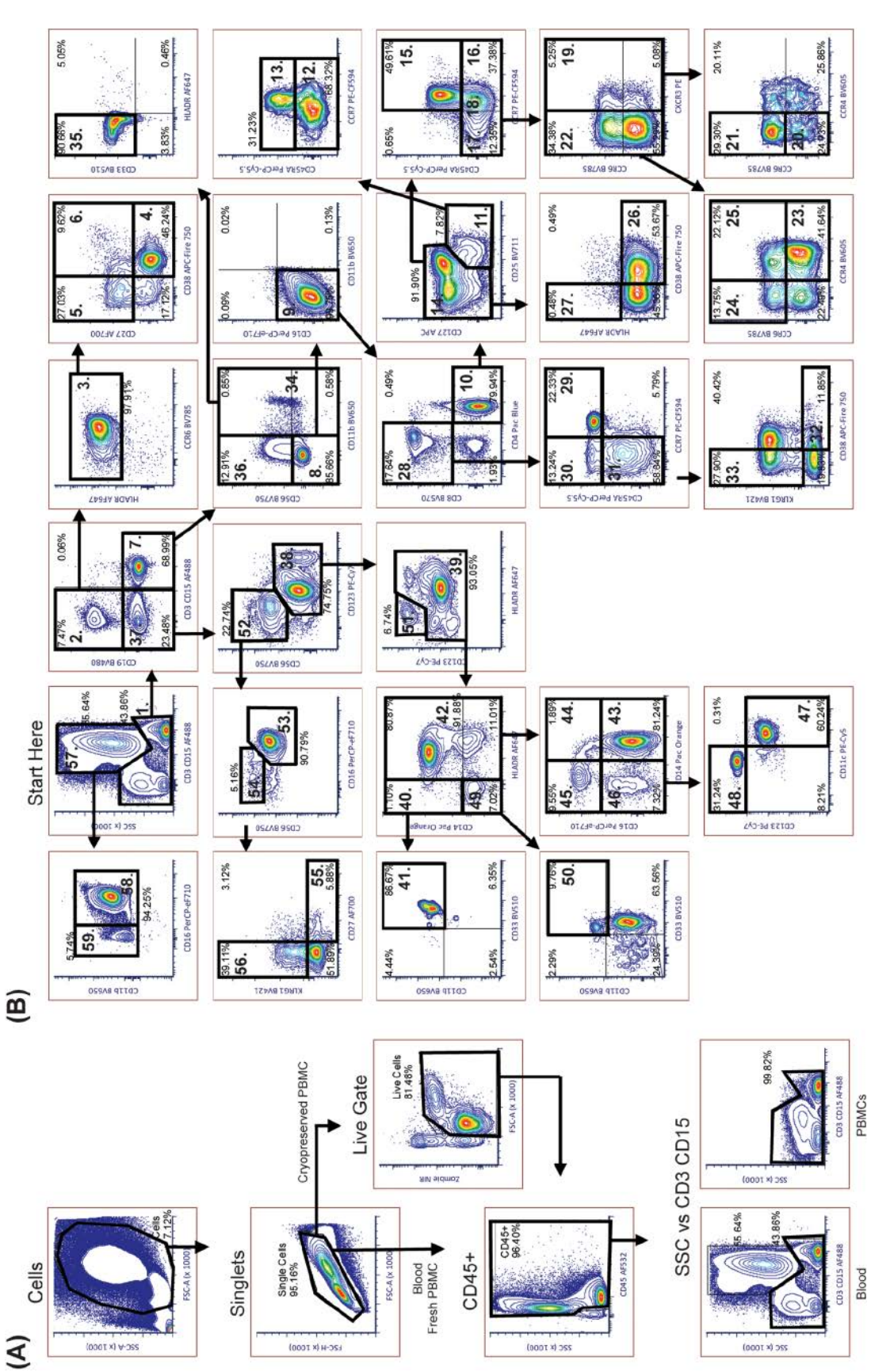

FIGURE 2 Gating strategy. (A) Debris, doublets, and CD45−cells are excluded from the downstream gating as shown using a whole blood example. For blood and fresh PBMC, viability routinely exceeds 97–98% so viability staining is not included. For cryopreserved PBMC, a live/dead gate is included prior to CD45−cell exclusion. An example SSC versus CD3/CD15 plot for blood and PBMC (either fresh or cryopreserved) is shown. (B) The established gating strategy for the immune monitoring panel contains 27 bivariate plots and 59 individual gates not including upstream debris, doublet and CD45− elimination shown in A. All 59 gates are numbered, and a comprehensive legend of the numbered gates is provided in Figure 3(A). Refer to Figure S4 for details regarding the CD56+ artifact on CD15+CD11b+ low-density granulocytes (LDGs)

ISAC CYTOMETRY Journal of Quantitative Cell Science PART A

(A)

Legend for Figure 2B

Gating Hierarchy	Population Description
1. SSClo	Low-Density cells
2. CD19+	CD19+ cells
3. CD19+HLADR+	Total B cells
4. CD19+HLADR+CD38+	CD38+ Mature B cells
5. CD19+HLADR+CD27+	CD27+ Memory B cells
6. CD19+HLADR+CD27+CD38+	Plasmablasts & Plasma cells
7. CD3+CD15+	CD3+CD15+ cells
8. CD3+CD15+CD56-	CD3+CD15+ non-NKT cells
9. CD3+	Total T cells
10. CD4+	CD4 T cells
11. CD127loCD25hi	CD4 T regulatory cells (Tregs)
12. CD127loCD25hiCD45RA-	Memory CD4 Tregs
13. CD127loCD25hiCD45RA+	Naïve CD4 Tregs
14. nonCD127loCD25hi	nonTreg CD4 T cells
15. CD4+CD45RA+CCR7+	Naïve CD4 T cells
16. CD4+ CD45RA-CCR7+	Central Memory CD4 T cells
17. CD4+ CD45RA-CCR7-	Effector Memory CD4 T cells
18. CD4+ CD45RA-	Total Memory CD4 T cells
19. CD4+TMEM CXCR3+	CXCR3+ Memory CD4 T cells
20. CXCR3+CCR4-CCR6-	Th1 Memory CD4 T cells
21. CXCR3+CCR4-CCR6+	Th1/Th17 MemoryCD4 T cells
22. CD4+TMEM CXCR3-	CXCR3- Memory CD4 T cells
23. CXCR3-CCR4+CCR6-	Th2 Memory CD4 T cells
24. CXCR3-CCR4-CCR6+	Th9 Memory CD4 T cells
25. CXCR3-CCR4+CCR6+	Th17/22 MemoryCD4 T cells
26. CD4+CD38+	CD38+ activated CD4 T cells
27. CD4+HLADR+	HLADR+ activated CD4 T cells
28. CD8+	CD8 T cells
29. CD8+ CD45RA+CCR7+	Naïve CD8 T cells
30. CD8+ CD45RA+CCR7-	Effector CD45RA+ CD8 T cells

Gating Hierarchy Continued	Population Description
31. CD8+ CD45RA-CCR7-	Effector Memory CD8 T cells
32. CD8+CD38+	CD38+ activated CD8 T cells
33. CD8+KLRG1+	KLRG1+ terminal effector CD8 T cells
34. CD15+CD11b+	CD15+CD11b+ LDGs
35. CD15+CD11b+HLADR-CD33+	PMN-MDSCs
36. CD3+CD56+	NKT cells
37. CD3-CD15-CD19-	non(T,B,LDG) cells
38. CD3-CD15-CD19-CD123+	Myeloid Cells & Basophils
39. nonHLADR-CD123+	nonBasophils
40. CD14+HLADR-	CD14+HLADR- cells
41. CD14+HLADR-CD11b+CD33+	M-MSDCs
42. HLADR+	HLADR+ Monocytes & DCs
43. CD14hiCD16lo	Classical Monocytes
44. CD14hiCD16hi	Intermediate Monocytes
45. CD14loCD16hi	Nonclassical Monocytes
46. HLADR+CD14-CD16-	Dendritic cells (DCs)
47. CD11chiCD123lo	monocytic DCs (mDCs)
48. CD11cloCD123hi	plasmacytoid DCs (pDCs)
49. CD14-HLADR-	CD14-HLADR- cells
50. CD14-HLADR-CD11b+CD33+	e-MDSCs
51. HLADR-CD123+	Basophils
52. CD3-CD15-CD19-CD56+	NK cells
53. CD56loCD16hi	CD56lo cytotoxic NK cells
54. CD56hiCD16lo	CD56hi cytokine-producing NK cells
55. CD56+CD27+	CD27+ mid-stage NK cells
56. CD56+KLRG1+	KLRG1+ terminal effector NK cells
57. SSChi	Granulocytes
58. CD15+CD16+	Neutrophils
59. CD15+CD16-	Eosinophils

(B)

Fluor-Minus-Multiple Controls

Panel	FMM1	FMM2	FMM3
KLRG1	KLRG1	-	KLRG1
CD4	CD4	CD4	CD4
CD19	CD19	CD19	CD19
CD33	CD33	CD33	-
CD14	CD14	-	CD14
CD8	CD8	CD8	CD8
CCR4	-	CCR4	CCR4
CD11b	CD11b	CD11b	-
CD25	-	CD25	CD25
CD56	CD56	-	CD56
CCR6	CCR6	CCR6	-
CD3	CD3	CD3	CD3
CD15	-	CD15	CD15
CD45	CD45	CD45	CD45
CXCR3	CXCR3	-	CXCR3
CCR7	CCR7	CCR7	-
CD11c	CD11c	-	CD11c
CD45RA	-	CD45RA	CD45RA
CD16	CD16	CD16	-
CD123	-	CD123	CD123
CD127	CD127	-	CD127
HLADR	HLADR	HLADR	-
CD27	-	CD27	CD27
CD38	CD38	CD38	-

(C)

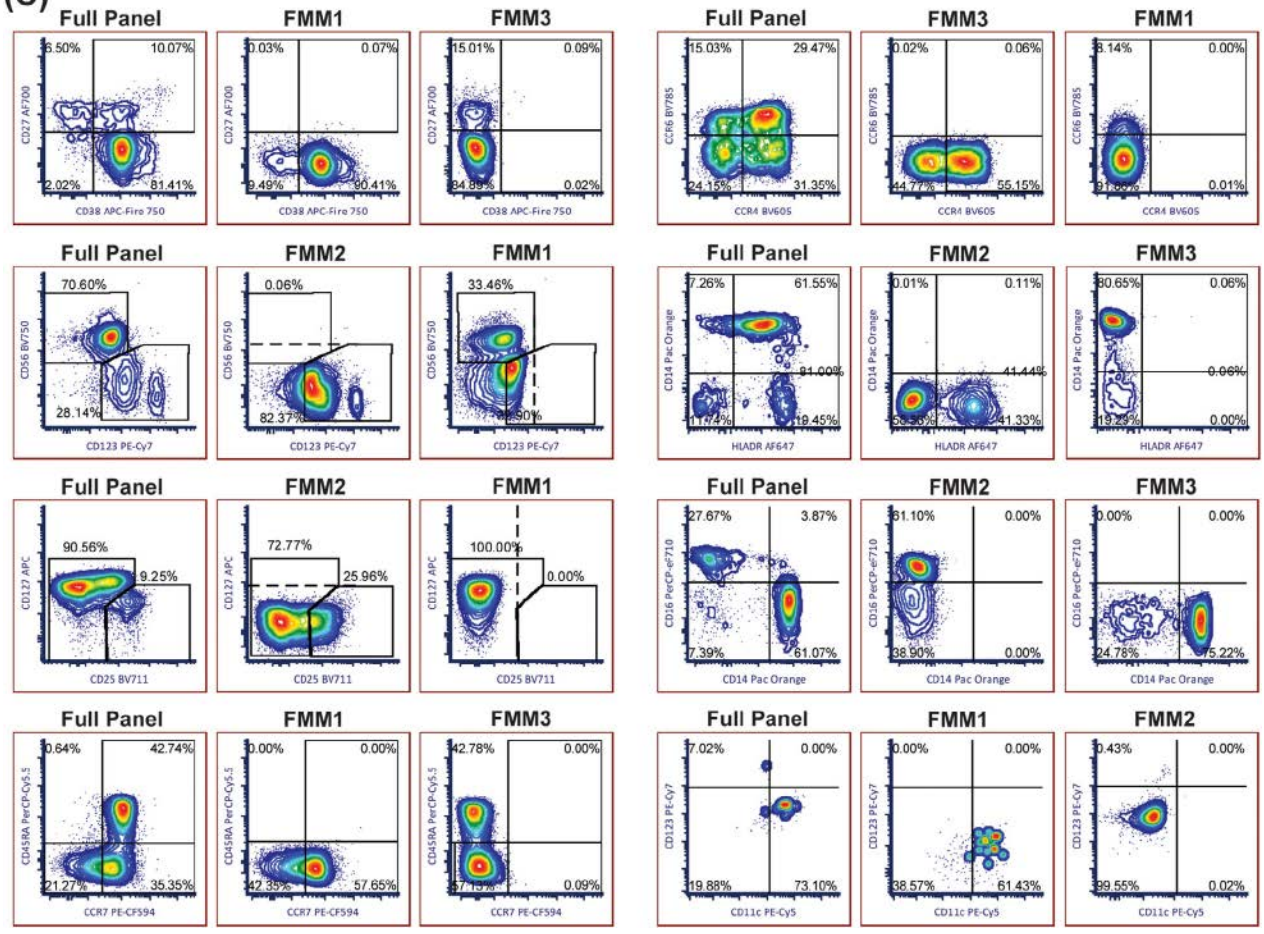

FIGURE 3 Gating legend and fluorescence-minus-multiple (FMM) controls. (A) A detailed legend of the established hierarchical gating strategy presented in Figure 2(B) is shown. (B) We designed three FMMs controls that eliminate six to seven reagents each. (C) Example bivariate plots showing how the suggested FMM controls can be used to place gates and confirm populations. Note that for CD56 versus CD123 and CD127 versus CD25, polygon gates are used in place of quadrants. Dotted lines are shown to clarify how the FMMs are used to guide placement of the polygon gates. Also note that for some populations, gate placement is dictated by high expression levels as opposed to positive (CD14hi, CD25hi)

yielded the cleanest manual separation of granulocytes across donors (Figure S4(D)). Granulocytes are then gated on a CD11b versus CD16 plot to identify eosinophils (CD16–) and neutrophils (CD16+). Monocytes and lymphocytes are assessed together to prevent misassignment of CD33lo cell types (pDCs, basophils, and some B cells) that straddle these two populations on a standard SSC versus FSC plot (Figure S4(C)).

3.2.2 | T-, B-, and NK-cell Gating

We began with a CD19 versus CD3+CD15+ plot to separate out B cells (Figure S5(A)), which are further assessed with HLADR, CCR6, CD38, and CD27. CD15+ low-density granulocytes (LDGs) exist within the CD3+CD15+ cell gate and can confound the T- and NKT-cell gate (Figure S4(E)). CD11b+ is used to separate these CD15+ cells from the T and NKT cells. T-cell gating follows a conventional format using CD8 versus CD4, CD45RA versus CCR7 for naïve/memory T cells, and CD127 versus CD25 for CD4 T regulatory cells, or Tregs (Figure 2). Tregs are gated on a separate CD45RA versus CCR7 plot to identify naïve/natural Tregs from memory/induced Tregs. HLADR, KLRG1, and CD38 plots are also used to identify activated T cells. A similar CCR6 versus CCR4 and CXCR3 gating format to that of OMIP-042 [8] is used to identify polarized T helper (Th) populations. We explored several CD56 versus myeloid marker bivariate plots (Figure S5(B)) and chose CD123, which consistently yielded the cleanest separation of CD56+ NK cells, which are then identified as CD56hiCD16lo or CD56loCD16hi. NK cells are also plotted on a KLRG1 versus CD27 bivariate plot for visualization of terminal effector and memory-like phenotypes.

3.2.3 | Monocyte and MDSC gating

CD123+HLADR– basophils are first removed from the CD3–CD15–CD19–CD56– population. Common monocyte gating strategies include either CD16 versus CD14 (e.g., OMIP-038) or CD14 versus HLADR (e.g., OMIP-042, OMIP-044) bivariate plots. We confirmed that gating on all HLADR+ cells is the best option for preventing nonclassical monocyte contamination in the monocytic DC (mDC) gate and vice versa (Figure S6). HLADR+ cells are analyzed to identify CD14hiCD16lo classical monocytes, CD14hiCD16hi intermediate monocytes, and CD14loCD16hi nonclassical monocytes. The CD14–CD16– population is gated on a CD123 versus CD11c plot to identify CD11chiCD123lo mDCs and CD11cloCD123hi plasmacytoid DCs (pDCs). Although a true MDSC biomarker remains elusive, efforts to establish a gating consensus have been published [12]. Most strategies focus on HLADR–/lo populations that are either CD15+ or CD14+ to identify granulocytic (PMN-) MDSC and monocytic (M-) MDSC, respectively, with additional characterization using CD11b and CD33. Here, CD14+HLADR– and CD14–HLADR– were gated and subject to CD11b versus CD33 bivariate plots to identify any M-MDSCs or early (e-) MDSCs. Earlier, we defined CD15+CD11b+ LDGs and many of these appear to be CD33+HLADR– PMN-MDSCs.

3.2.4 | FMMs

For large 20+ color panel design where sample and reagent economy are concerns, true fluorescence-minus-one (FMO) controls become intractable. Fluorescence-minus-multiple (FMM) controls are employed here to ensure correct population analysis when applying gating strategies to bivariate plots. Primary lineage markers with consistently clean separation do not need to be included in FMM controls (CD4, CD19, CD8, CD3, CD45, and Zombie NIR). We designed three companion FMM control panels that each eliminate six to seven biomarkers (Figure 3(B)). When distributing absentee markers across three FMMs, several factors were considered. Nearby fluorophores were separated, creating "local FMOs" while maintaining separation of absentee marker pairs used in bivariate plots (e.g., CCR4 BV605 vs. CCR6 BV785, see Figure 3(C)). Finally, we aimed to distribute activation markers (CD25, HLADR) equitably across the three FMMs.

3.3 | Analytical performance characterization

3.3.1 | Donor variability

Upon application of the established immunophenotyping panel, we first confirmed the variability in immune cell population frequencies in peripheral blood across six healthy donors (Figure 4(A)). Similar to other findings [16], the peripheral immune compartment differed when comparing longitudinal collections from the same individual (Figure 4(B)). We collected blood samples from five healthy donors and provide examples for which the % population (% of parent gate) differed for an individual donor over a period of 14 days. Immune perturbations are unsurprising due to a multitude of factors such as small changes in nutrition, sleep, and/or minute opportunistic infections that go unnoticed.

3.3.2 | Blood stability

We assessed biomarker stability in three healthy donor blood samples collected in Na-Heparin tubes and stored at 4°C for 24, 48, and 72 h before analysis. Intra-donor average differences at each timepoint from baseline (0 h) for every % gated population are presented in Figure 4(C). CXCR3+ memory CD4 cells exhibit an average >500% change from 0 h (i.e., an increase from 5-10% at baseline to 40-50%) by 24 h, suggesting this population is sensitive to prolonged storage. Interestingly, this increase in CXCR3+ memory CD4 T cells then remains relatively stable at 48 and 72 h (Figure 4(C); Table S2). Other populations affected by 24 h of storage prior to analysis include increased Th17/22 cells, decreased CD45RA+ Tregs and decreased CD11cloCD123hi pDCs. Interestingly, some of these populations were also more sensitive to PBMC isolation or cryopreservation (Figure 5(C,D)). A statistical summary of Figure 4(C) is shown in Figure 4(D).

3.3.3 | Assay precision in blood

Less abundant (but certainly not rare) immune subsets such as CD4 memory subsets or T regulatory cells can fail conventional cytometry assay precision metrics [2,16]. We analyzed blood collected from six healthy donors and stained in triplicate to assess the intra-assay precision of the established immunophenotyping panel. The % CV (percent coefficient of variation) values were calculated across replicates (intra-run/intra-donor) and % CV results averaged across donors for reporting simplicity (Figure 4(E); Table S1). With robust gating, we

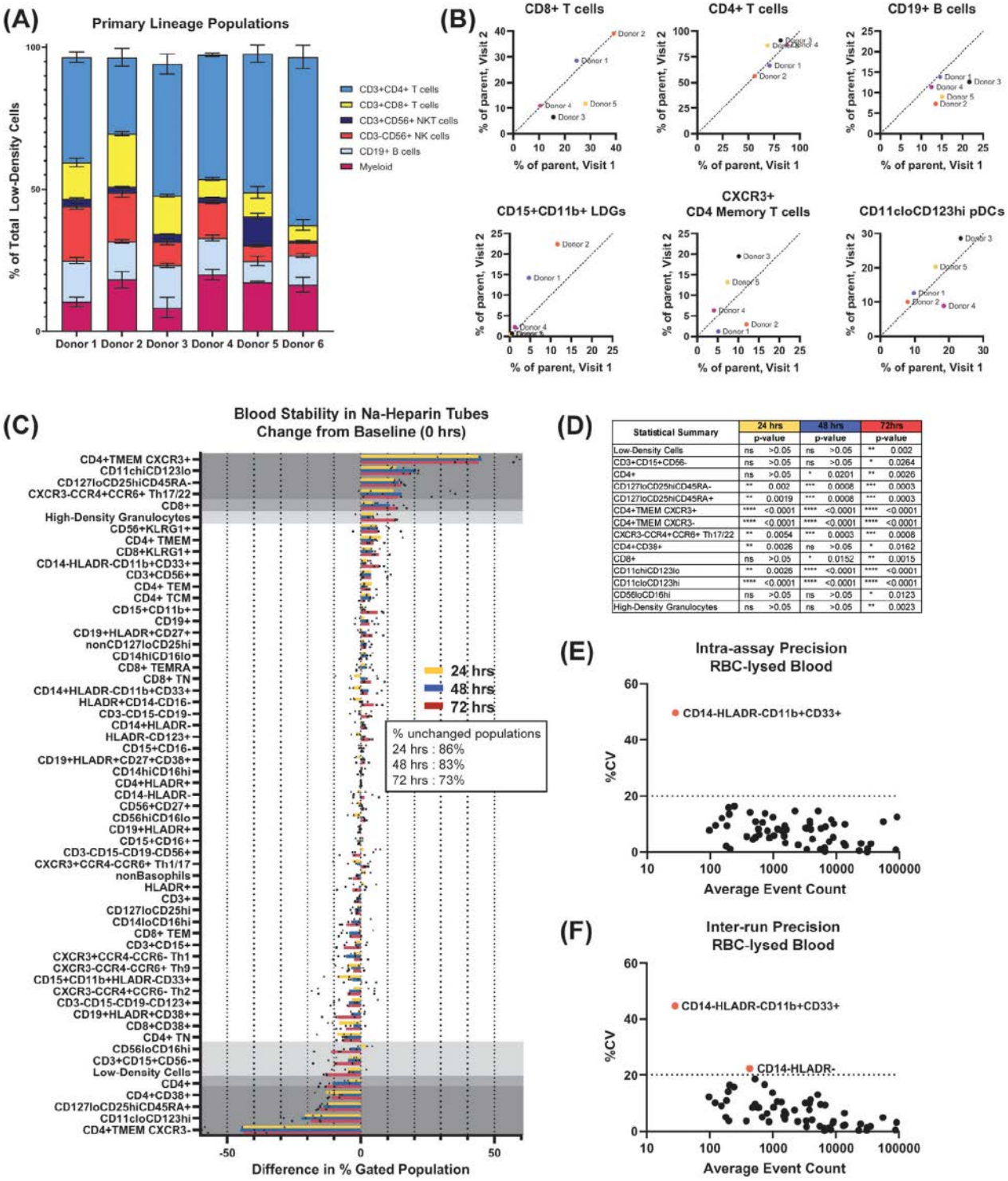

Statistical Summary	24 hrs		48 hrs		72hrs	
	p-value		p-value		p-value	
Low-Density Cells	ns	>0.05	ns	>0.05	**	0.002
CD3+CD15+CD56-	ns	>0.05	ns	>0.05	*	0.0264
CD4+	ns	>0.05	*	0.0201	**	0.0026
CD127loCD25hiCD45RA-	**	0.002	***	0.0008	***	0.0003
CD127loCD25hiCD45RA+	**	0.0019	***	0.0008	***	0.0003
CD4+TMEM CXCR3+	****	<0.0001	****	<0.0001	****	<0.0001
CD4+TMEM CXCR3-	****	<0.0001	****	<0.0001	****	<0.0001
CXCR3-CCR4+CCR6+ Th17/22	**	0.0054	***	0.0003	***	0.0008
CD4+CD38+	**	0.0026	ns	>0.05	*	0.0162
CD8+	ns	>0.05	*	0.0152	**	0.0015
CD11chiCD123lo	**	0.0026	****	<0.0001	****	<0.0001
CD11cloCD123hi	****	<0.0001	****	<0.0001	****	<0.0001
CD56loCD16hi	ns	>0.05	ns	>0.05	*	0.0123
High-Density Granulocytes	ns	>0.05	ns	>0.05	**	0.0023

FIGURE 4 Legend on next page.

observed high replicate precision (<20% CV) across the majority of cell populations (% of parent gate) with exception to the CD14−HLADR−CD11b+CD33+ (e-MDSC) population, which failed repeatability (>20% CV). This population generally consisted of fewer than 100 cells at the employed acquisition settings (Figure 4(E); Table S1). Lastly, we averaged the % CV of replicates across the timepoints explored to assess inter-run precision, as inter-operator or inter-instrument runs were not obtainable. As before, the CD14−HLADR−CD11b+CD33+ e-MDSC population consistently failed intra-assay precision (>20% CV) and thus failed inter-run precision (Figure 4(F)).

3.3.4 | Assay precision in PBMC

We also assessed intra-assay precision for freshly isolated PBMC and cryopreserved PBMC (Figure 5(A,B)). Using equivalent sample preparation (i.e., number of low-density cells per tube) and the same acquisition settings, both PBMC and cryopreserved PBMC had too few events (sometimes none) for CD14−HLADR−CD11b+CD33+ to allow % CV calculation (Table S1). Cryopreserved PBMC also failed precision for the total CD14−HLADR− cells (Figure 5(B); Table S1). Generally, % CVs for PBMC data trend higher for less abundant populations as noted by others [2]. Nonetheless, our spectral cytometry assay and associated gating strategy is highly robust for blood, PBMC and cryopreserved PBMC samples, exhibiting <20% CV for >95% all gated populations.

3.3.5 | Biomarkers in PBMCs

We investigated the changes to immune cell populations after PBMC isolation in the context of the developed assay. Comparisons were made between donor-matched blood and PBMCs isolated the same day from three healthy individuals. Only low-density populations were compared as PBMCs do not contain high-density granulocytes (Figure 2(A)). Calculating the difference in % population (% of parent) reveals that 42 out of 49 gated immune cell populations (86%) are stable after PBMC isolation (Figure 5(C)). Only a handful of populations (e.g., pDCs and CD15+CD11b+ LDGs) are statistically significantly different between blood and isolated PBMC, but many changes trend similarly across the donors used. Notably, there is an average >500% increase in CXCR3+ memory CD4 T cells after PBMC isolation (Table S1), suggesting this marker is sensitive to this process.

PBMC cryopreservation can also impact surface marker expression [17–19]. Isolated PBMC from three healthy individuals were compared to donor-matched PBMC after storage at −80°C for 7 or more days. Cryopreserved PBMC were stained with Zombie NIR live/dead stain and gated as required (Figure 2(A)). Calculating the difference in % population from baseline (fresh PBMC), most populations do not exhibit a significant change (36 out of 49 gates, or 73%) after cryopreservation (Figure 5(D); Table S1). However, there were some opposing trends for individual donors. Significant changes across the three donors include CD14hiCD16lo/CD14loCD16hi monocyte cell ratio, CD4/CD8 ratio, a shift away from naïve CD45RA+ Tregs toward memory CD45RA− Tregs, disruption of CD38 expression on CD4 T cells, increased M-MDSCs and increased Th1 cells. A decrease in CD45RA+ Treg abundance when comparing blood to matched cryopreserved PBMCs has been reported elsewhere [2,17]. Overall, care must be taken to assess biomarkers of interest when using cryopreserved PBMC samples.

3.4 | Advanced data analysis

We performed tSNE analysis on healthy blood donor datasets followed by FlowSOM analysis [20] using the cloud-based analysis platform Cytobank. When comparing 15 metaclusters to an equivalent number of manual gates, the FlowSOM algorithm identified several populations differently (Figure 6(A,C)). FlowSOM assigned mDCs and monocytes to a single metacluster, while combining intermediate and nonclassical monocytes into another metacluster. Interestingly, rare/unknown cell types or artifacts were identified and placed into

FIGURE 4 Donor variability, blood stability, and assay precision. (A) We assessed immune compartment variability in the peripheral blood of six healthy donors. The bar chart displays the % of total CD45+ low-density cells for each donor. Note the differences in major immune cell lineages for each individual. (B) We assessed intra-donor longitudinal variability by comparing blood collections from the same five healthy donors taken 14 days apart. Six example populations are shown for which small immune perturbations can be seen for each donor between the two collection timepoints. (C) We investigated the stability of healthy blood from three donors collected in Na-Heparin tubes and stored at 4°C during the interim. The difference in % population at 24 h (yellow), 48 h (blue) and 72 h (red) from baseline (0 h) is shown for each gated population. Intra-donor averages from triplicates are shown with black triangles (24 h), dots (48 h) or squares (72 h). Populations with statistically significant changes are shown within the grey shaded regions. (D) The statistical results from (C) are shown in the table. The average % population values across all donors at each timepoint (Table S2) were compared to the 0 h timepoint using two-way ANOVA. Statistically significant populations across all donor samples are indicated with * (p<0.05), ** (p<0.01), *** (p<0.001) or **** (p<0.0001). Forty-five out of 59 (76%) of gated populations are not significantly changed by storage at 4°C for 72 h, and 51 out of 59 (86%) of the gated populations are not significantly changed after 24 h of storage at 4°C. (E) We assessed the intra-assay (intra-donor, intra-run) % coefficient of variation (% CV) for each gated population. The % CV values are graphed against average donor event count for the respective population. Tabulated data for the graphical data are shown in Table S1. For simplicity, the intra-assay % CV values were averaged across six healthy donors. Only CD14−HLADR−CD11b+CD33+ population (e-MDSC) fails precision (>20% CV) for the whole blood analysis. (F) We assessed inter-run precision across the timepoints explored as inter-operator and inter-instrument runs were not obtainable. As before, the CD14−HLADR−CD11b+CD33+ e-MDSC population consistently failed intra-assay precision (>20% CV) and thus failed inter-run precision. The parent population CD14−HLADR− also failed inter-run precision

ISAC CYTOMETRY
Journal of Quantitative Cell Science PART A

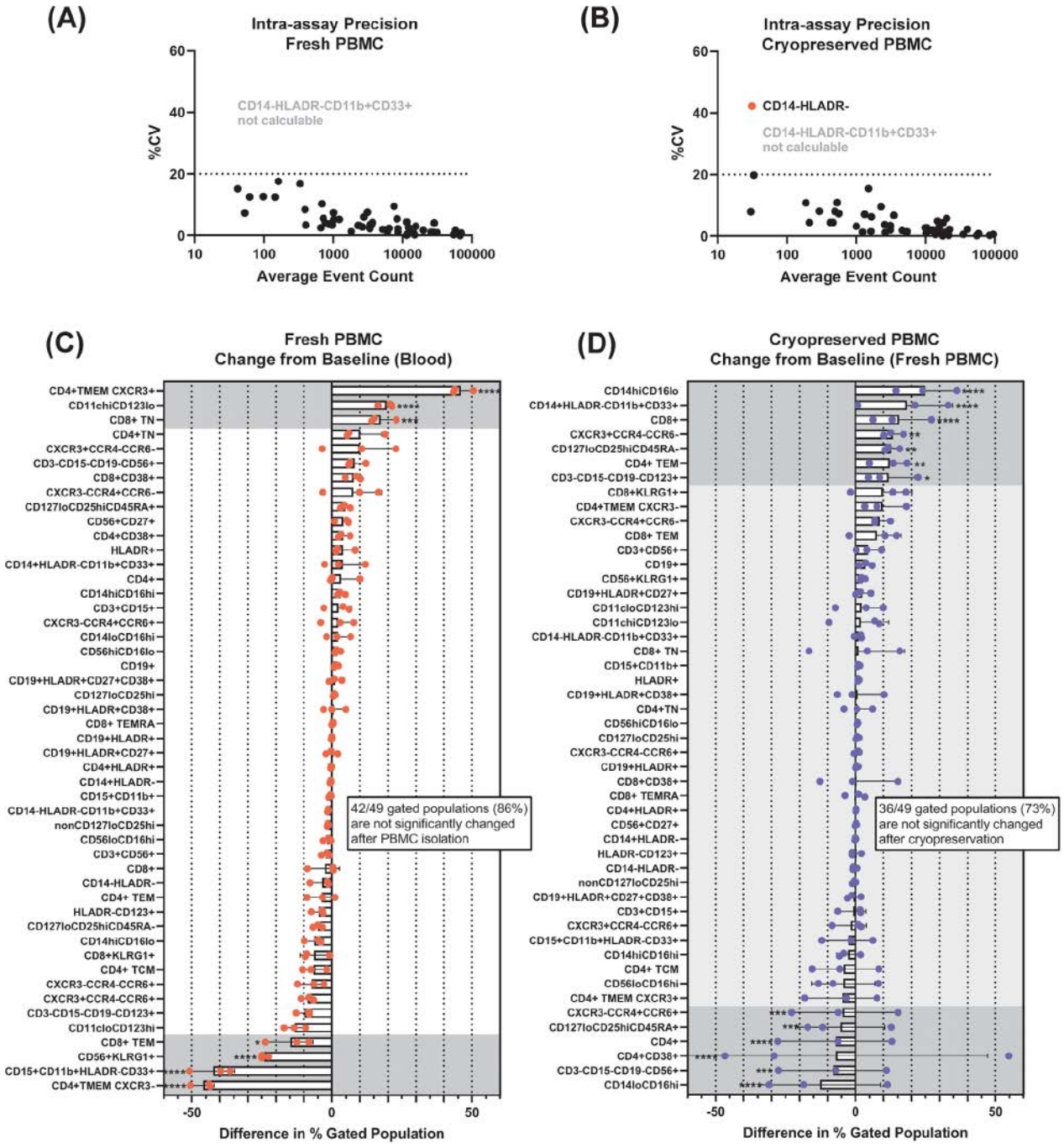

FIGURE 5 Assay performance on peripheral blood mononuclear cell (PBMC). We assessed the intra-assay (intra-donor, intra-run) % coefficient of variation (% CV) for each gated population for (A) fresh PBMC and (B) cryopreserved PBMC. Tabulated data for the graphical data in (A) and (B) are shown in Table S1. For simplicity, the intra-assay % CV values were averaged across three healthy donors each for PBMC and cryopreserved PBMC. Only the CD14−HLADR−CD11b+CD33+ population (e-MDSC) is not estimable for PBMC or cryopreserved PBMC. CD14−HLADR− fails precision (>20% CV) for cryopreserved PBMC. The % CV values are graphed against average donor event count for the respective population. (C) The difference in % gated population for PBMC from baseline (blood) is shown for each donor (red dots, intra-donor average of three replicates) and averaged across donors (white bars). Populations that display significant changes (PBMC) from baseline (blood) are calculated using two-way ANOVA and indicated with * (p<0.05), ** (p<0.01), *** (p<0.001) or **** (p<0.0001) within the grey shaded region. Forty-two out of 49 (86%) of comparable gated populations are not significantly changed by PBMC isolation. (E) The difference in % gated population for cryopreserved PBMC from baseline (freshly isolated PBMC) is shown for each donor (blue dots, intra-donor average of three replicates) and averaged across donors (white bars). Populations that display significant changes (cryopreserved PBMC) from baseline (PBMC) are calculated using two-way ANOVA and indicated with * (p<0.05), ** (p<0.01), *** (p<0.001) or **** (p<0.0001) within the grey shaded region. Thirty-six out of 49 (73%) of comparable gated populations are not significantly changed by cryopreservation, although trends were mixed across donors

their own metaclusters. FlowSOM more cleanly identified NK cells, which were contaminated with CD14−HLADR− cells using our manual gating strategy (Figure 6(A)) despite our thoughtful comparison of CD56 versus myeloid marker gating options (Figure S5(B)). FlowSOM separated NKT cells from CD8 T cells differently and reduced the number of events identified as Tregs by our manual gating strategy. This suggests that our manual gating of Tregs using CD127 versus CD25 plots captures nonTregs as well. The immune marker expression profiles for the manually gated populations and FlowSOM metaclusters are shown as heatmaps (Figure 6(B,D)). A comparison of the expression heatmaps suggests that, for example, CCR4 should be used in addition to CD127 and CD25 (considering the absence of FoxP3 here) to correctly identify Tregs manually.

We compared the % of parent and % CV values for individual populations analyzed using manual gating to FlowSOM analysis. This required extensive manual annotation of individual FlowSOM clusters. For example, while FlowSOM assigned some rarer populations to independent clusters (basophils, pDCs), several clusters (five or more) within a single metacluster could be phenotypically classified as naïve CD4 T cells. Thus, these clusters were analyzed together to achieve comparable population metrics. Ideally, a comprehensive evaluation of the optimal metacluster-to-cluster ratio for FlowSOM analysis could be explored but is beyond the scope of this work. Here, we manually calculated % of parent cluster values, based on annotated grouped clusters, from event-per-cluster FlowSOM results. FlowSOM does result in differences in population identification (Figure 6(E)) and interestingly, results in % CV values that are less robust for some populations, notably monocytes (Figure 6(F)). This could be partially due to FlowSOM's previously demonstrated overlap between mDCs with classical monocytes, and intermediate with nonclassical monocytes at the applied clustering settings. In the end, effective and efficient workflows to translate automatically analyzed cytometry data into assay performance reportables such as % CVs are still needed.

4 | DISCUSSION

The recent *Cytometry Part A* Special Issue: Rigor and Reproducibility highlighted the importance of antibody validation, sample preparation and instrument, assay and post-analysis standardization [21–23]. These practices are indispensable to successful analytical performance or complete validation of high-dimensional assays. Recently, Park et al. published OMIP-069 detailing 40-color immunophenotyping on a full spectrum cytometer [24]. Despite this milestone, performance characterization activities for large spectral cytometry or mass cytometry panel designs face future challenges due to the complexity of high-parameter datasets. That being said, spectral cytometry inherently empowers straightforward assessment of pre-analytical reagent stability and compatibility. The fixed optical configuration of spectral cytometers combined with vendor-established gain values (e.g., the Cytek Assay Setting) minimizes the work required for multi-instrument standardization. Variability in large panel preparation can be mitigated with robotic pipetting platforms or lyophilized samples. Meanwhile, interactive web resources have become available to address the quality of antibody reagents and evaluate the expression profiles of a multitude of immune biomarkers [15,25].

Our comprehensive gating strategy captures major immune subsets reported by the Human Immune Phenotyping Consortium [1]. Our experience advocates against employing manual gates on standard SSC versus FSC plots to mitigate downstream population assignment errors. Additionally, we explored monocyte populations in depth using tSNE analysis and observed that six to nine populations may exist on a typical CD14 versus CD16/HLADR plot (Figure S6). These include classical monocytes, intermediate monocytes, nonclassical monocytes, mDCs, pDCs, a potential transitional state between classical monocyte and mDC, e-MDSC or other precursor cell type, M-MDSC or similar, and a unique CD16+ population (negative/low for all other markers). Interestingly, this CD16+ cell type appears to be the same population that FlowSOM eliminated from our manual CD56+ gate (Figure 6(A,B)). Multiple monocyte types were also identified on similar bivariate plots using five myeloid markers in place of CD14 and CD16 [26]. Of note, the exact relationship between nonclassical monocytes and DCs has not been fully elucidated. Nonetheless, tSNE clearly separated mDCs from nonclassical monocytes despite their significant overlap on standard bivariate plots (Figure S6). It is imperative to address these technicalities and develop a gating scheme that is accurate and relatively robust across individual samples. Multicenter manual gating alone can be a significant source of assay variability [1,23], although others report that biological variability often exceeds technical variability [2].

For some populations, other groups have reported much higher % CVs for cryopreserved PBMC samples analyzed using conventional flow cytometry than we found in this study [2,16]. Standardization with PBMCs works well for abundant cell populations, but less so for rarer subsets and the T helper subsets [1]. Using our 25-biomarker assay, only the phenotypic e-MDSC population either failed repeatability in blood (>20% CV) or was incalculable in PBMC due to fewer than 100 cells at the employed acquisition settings. Disease sample benchmarking could potentially improve panel performance [23] as nonhealthy samples typically have expanded MDSC compartments [11]. Immune biomarkers and populations that were sensitive to 24+ h blood storage or PBMC manipulation (or both) include CXCR3 expression on memory CD4 T cells, Th1 or Th17 cells, CD45RA+ Tregs, CD38+ CD4 T cells, classical and nonclassical monocytes, M-MDSCs, CD15+CD11b+ LDGs, and CD11cloCD123hi pDCs. Care should be taken when interpreting results for these potentially sensitive populations. One group using five 9-color immune panels found that most immune cell populations in the blood are stable when analyzed 24 h post collection in EDTA tubes; however, their panels did not include CXCR3 [2]. Other tube formats with stabilizers could improve upon biomarker stability. Adoption of an empirical approach to establish what populations are stable post blood collection, and in what tube format, can better inform acceptable conditions and timeframes for analysis.

Currently, many advanced algorithms are accessible through commercial software. However, we experienced the challenge of manually

ISAC CYTOMETRY Journal of Quantitative Cell Science PART A

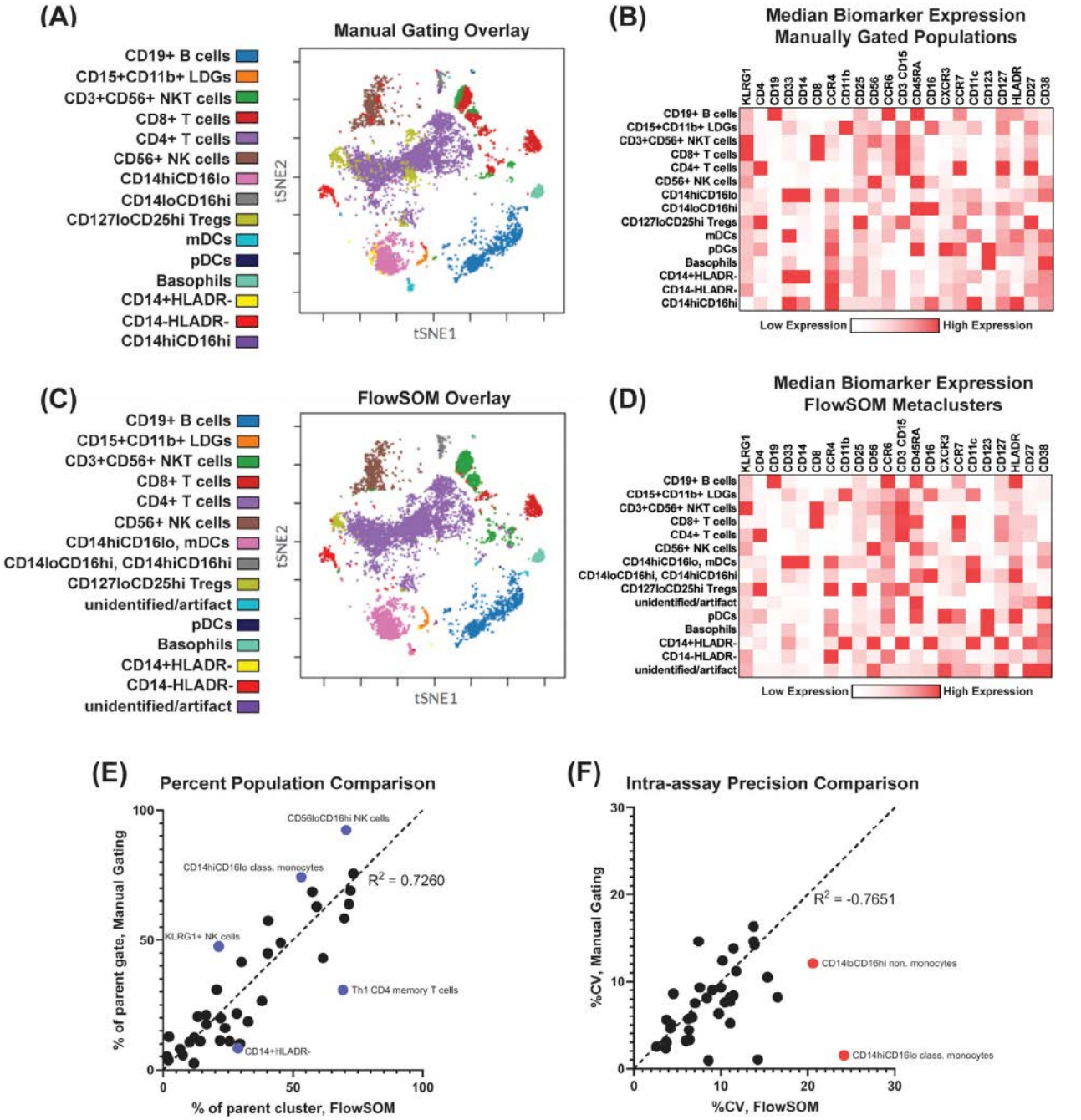

FIGURE 6 Manual gating versus FlowSOM. (A) We performed tSNE analysis in Cytobank on the low-density (non-granulocyte) cells from six healthy donor blood data and overlaid manually defined gates for 15 major immune cell subsets (one donor example shown). (B) The normalized median biomarker expression for the manually gated immune cell subsets are shown in the heatmap, with white indicating no/low expression and red indicating high expression. (C) We also performed FlowSOM analysis in Cytobank, selecting 15 metaclusters which were then overlaid onto our tSNE plot (same donor example shown). There were key differences between the FlowSOM clustered data and the manually gated data, suggesting that automated machine-learning algorithms like FlowSOM can greatly improve upon subjective manual gating methods. Notable differences FlowSOM produced include cleaner NK cell population and restricted Treg identification. (D) The normalized median biomarker expression for the FlowSOM metaclusters are shown in the heatmap, with white indicating no/low expression and red indicating high expression. (E) We annotated the 100 clusters and 15 metaclusters identified by FlowSOM into 37 immunophenotypes. Although the manual gating strategy contains 59 gates total, this accounts for inclusion of hierarchical step-wise gates (e.g., the CD3−CD15−CD19− gate), the high-density granulocyte gates, and activation marker gates (e.g., HLADR+ CD4 T cells) that did not always have representative or distinct clusters in the FlowSOM results. The equivalent FlowSOM versus manually gated % of parent values (average from six healthy donor blood samples) for 37 comparable populations are shown. The data fit a direct relationship (line of slope 1) with a coefficient of determination (R^2) of 0.7260. The five populations with the highest residuals (greatest distance from center line) are shown by the blue dots, although there were no statistical outliers. (F) The % CV values (from intra-donor triplicates) were calculated for the 37 annotated FlowSOM populations and plotted against the % CVs determined previously for the manually gated data. The data fit a direct relationship with an R^2 of −0.7951. Two populations that failed intra-assay precision based on FlowSOM clustering were classical monocytes and nonclassical monocytes, shown by the red dots, which were also statistical outliers. The CD14−HLADR−CD11b+CD33+ (e-MDSC) population that failed intra-assay precision previously was not an independent FlowSOM cluster

annotating our FlowSOM results to estimate intra-assay precision. Efficient and advanced workflows that readily convert cytometry data into statistically meaningful analyses and reportables are still lacking. Many internally implemented analyses rely on multidisciplinary subject matter experts with sufficient backgrounds in both immune profiling and computational analysis. Presently, creating data analysis workflows often becomes just as time-consuming, if not more so, than manual gating.

5 | CONCLUSIONS

We explored high-parameter flow cytometry assay development on a spectral cytometer and performed a preliminary evaluation of associated performance characteristics. Spectral cytometry platforms allow great flexibility in assay design while retaining familiarity with conventional reagent and instrument operation. We assessed intra-assay precision for blood, fresh PBMCs and cryopreserved PBMCs and found that >95% of gated populations exhibited high precision across experimental replicates. Additionally, gated populations do not change significantly for most populations after 24 h of blood storage (86%), PBMC isolation (86%), or PBMC cryopreservation (73%). Overall, we present this 25-biomarker immune monitoring panel as an example of the highly improved analytical performance achievable on a spectral cytometry platform toward translational biomarker application.

ACKNOWLEDGMENTS

The authors would like to acknowledge the Cytek team for their technical support. Special thanks to Alex Wendling for sharing his FCS Express template for generating CSI matrices. Finally, thanks to the Merck & Co., Inc., Kenilworth, NJ, USA Volunteer Blood Donation program and our company's phlebotomists Michael Uva and Connie Lewis for providing healthy donor samples.

CONFLICT OF INTEREST

The authors have no conflicts of interest.

REFERENCES

1. Finak G, Langweiler M, Jaimes M, Malek M, Taghiyar J, Korin Y, et al. Standardizing flow cytometry immunophenotyping analysis from the human immunophenotyping consortium. Sci Rep. 2016;6:20686.
2. Ivison S, Malek M, Garcia RV, Broady R, Halpin A, Richaud M, et al. A standardized immune phenotyping and automated data analysis platform for multicenter biomarker studies. JCI Insight. 2018;3(23): e121867.
3. Pitoiset F, Cassard L, El Soufi K, Boselli L, Grivel J, Roux A, et al. Deep phenotyping of immune cell populations by optimized and standardized flow cytometry analyses. Cytom A. 2018;93(8):793–802.
4. Hartmann FJ, Babdor J, Gherardini PF, Amir ED, Jones K, Sahaf B, et al. Comprehensive immune monitoring of clinical trials to advance human immunotherapy. Cell Rep. 2019;28(3):819–31 e4.
5. Lannigan J. Is there a pot of gold at the end of the Spectrum? Cytom A. 2020;97(11):1105–1108.
6. Novo D, Gregori G, Rajwa B. Generalized unmixing model for multispectral flow cytometry utilizing nonsquare compensation matrices. Cytom A. 2013;83(5):508–20.
7. Ferrer-Font L, Pellefigues C, Mayer JU, Small SJ, Jaimes MC, Price KM. Panel design and optimization for high-dimensional immunophenotyping assays using spectral flow cytometry. Curr Protoc Cytom. 2020;92(1):e70.
8. Staser KW, Eades W, Choi J, Karpova D, DiPersio JF. OMIP-042: 21-color flow cytometry to comprehensively immunophenotype major lymphocyte and myeloid subsets in human peripheral blood. Cytom A. 2018;93(2):186–9.
9. Baumgart S, Peddinghaus A, Schulte-Wrede U, Mei HE, Grutzkau A. OMIP-034: comprehensive immune phenotyping of human peripheral leukocytes by mass cytometry for monitoring immunomodulatory therapies. Cytom A. 2017;91(1):34–8.
10. Dintwe O, Rohith S, Schwedhelm KV, McElrath MJ, Andersen-Nissen E, De Rosa SC. OMIP-056: evaluation of human conventional T cells, donor-unrestricted T cells, and NK cells including memory phenotype by intracellular cytokine staining. Cytom A. 2019;95(7):722–5.
11. Pawelec G, Verschoor CP, Ostrand-Rosenberg S. Myeloid-derived suppressor cells: not only in tumor immunity. Front Immunol. 2019; 10:1099.
12. Mandruzzato S, Brandau S, Britten CM, Bronte V, Damuzzo V, Gouttefangeas C, et al. Toward harmonized phenotyping of human myeloid-derived suppressor cells by flow cytometry: results from an interim study. Cancer Immunol Immunother. 2016;65(2):161–9.
13. Gabrilovich DI. Myeloid-derived suppressor cells. Cancer Immunol Res. 2017;5(1):3–8.
14. Li L, Wan S, Tao K, Wang G, Zhao E. KLRG1 restricts memory T cell antitumor immunity. Oncotarget. 2016;7(38):61670–8.
15. Amir ED, Lee B, Badoual P, Gordon M, Guo XV, Merad M, et al. Development of a comprehensive antibody staining database using a standardized analytics pipeline. Front Immunol. 2019;10:1315.
16. Burel JG, Qian Y, Lindestam Arlehamn C, Weiskopf D, Zapardiel-Gonzalo J, Taplitz R, et al. An integrated workflow to assess technical and biological variability of cell population frequencies in human peripheral blood by flow cytometry. J Immunol. 2017;198(4): 1748–58.
17. Lemieux J, Jobin C, Simard C, Neron S. A global look into human T cell subsets before and after cryopreservation using multiparametric flow cytometry and two-dimensional visualization analysis. J Immunol Methods. 2016;434:73–82.
18. Costantini A, Mancini S, Giuliodoro S, Butini L, Regnery CM, Silvestri G, et al. Effects of cryopreservation on lymphocyte immunophenotype and function. J Immunol Methods. 2003;278 (1–2):145–55.
19. Kotsakis A, Harasymczuk M, Schilling B, Georgoulias V, Argiris A, Whiteside TL. Myeloid-derived suppressor cell measurements in fresh and cryopreserved blood samples. J Immunol Methods. 2012;381 (1–2):14–22.
20. Van Gassen S, Callebaut B, Van Helden MJ, Lambrecht BN, Demeester P, Dhaene T, et al. FlowSOM: using self-organizing maps for visualization and interpretation of cytometry data. Cytom A. 2015;87(7):636–45.
21. Kalina T, Lundsten K, Engel P. Relevance of antibody validation for flow cytometry. Cytom A. 2020;97(2):126–36.
22. Laskowski TJ, Hazen AL, Collazo RS, Haviland D. Rigor and reproducibility of cytometry practices for immuno-oncology: a multifaceted challenge. Cytom A. 2020;97(2):116–25.
23. Kalina T. Reproducibility of flow cytometry through standardization: opportunities and challenges. Cytom A. 2020;97(2):137–47.
24. Park L, Lannigan J, James MC. OMIP-XXX: 40-color full Spectrum flow cytometry panel for deep Immunophenotyping of major cell subsets in human peripheral blood. Cytom A. 2020;97:1044–51.
25. Kalina T, Fišer K, Pérez-Andrés M, Kuzílková D, Cuenca M, Bartol SJW, et al. CD maps-dynamic profiling of CD1-CD100 surface expression on human leukocyte and lymphocyte subsets. Front Immunol. 2019;10:2434.

ISAC CYTOMETRY Journal of Quantitative Cell Science PART A

26. Ong SM, Teng K, Newell E, Chen H, Chen J, Loy T, et al. A novel, five-marker alternative to CD16-CD14 gating to identify the three human monocyte subsets. Front Immunol. 2019;10:1761.

SUPPORTING INFORMATION

Additional supporting information may be found online in the Supporting Information section at the end of this article.

How to cite this article: Jensen HA, Wnek R. Analytical performance of a 25-marker spectral cytometry immune monitoring assay in peripheral blood. *Cytometry*. 2021;99:180–193. https://doi.org/10.1002/cyto.a.24290

CYTOMETRY
Journal of Quantitative Cell Science PART A

Phenotypic Analysis of the Mouse Hematopoietic Hierarchy Using Spectral Cytometry: From Stem Cell Subsets to Early Progenitor Compartments

Michael Solomon,[1] Monica DeLay,[2] Damien Reynaud[1,3*]

[1]Stem Cell Program, Division of Experimental Hematology and Cancer Biology, Cincinnati Children's Hospital Medical Center, Cincinnati, Ohio, 45229,

[2]Cytek Biosciences, Fremont, California, 94538,

[3]Department of Pediatrics, University of Cincinnati College of Medicine, Cincinnati, Ohio, 45229,

Received 14 January 2020; Revised 25 March 2020; Accepted 29 April 2020

Grant sponsor: National Heart, Lung, and Blood Institute, Grant numberR01HL141418; Grant sponsor: National Institute of General Medical Sciences, Grant numberS10OD025045

Additional Supporting Information may be found in the online version of this article.

*Correspondence to: Damien Reynaud, Cincinnati Children's Hospital Medical Center, Division of Experimental Hematology and Cancer Biology, 3333 Burnet Avenue, MLC 7013, Room S7.603, Cincinnati, OH 45229 Email: damien.reynaud@cchmc.org

Grant sponsor: National Institutes of Health, Grant numbers: S10OD025045 and R01HL141418.

Published online 25 May 2020 in Wiley Online Library (wileyonlinelibrary.com)

DOI: 10.1002/cyto.a.24041

Abstract

Phenotypic analysis by flow cytometry is one of the most utilized primary tools to study the hematopoietic system. Here, we present a complex panel designed for spectral flow cytometry that allows for the in-depth analysis of the mouse hematopoietic stem and progenitor compartments. The developed panel encompasses the hematopoietic stem cell (HSC) compartment, an array of multipotent progenitors with early marks of lineage specification and a series of progenitors associated with lymphoid, granulo-macrophagic, megakaryocytic and erythroid lineage commitment. It has a built-in redundancy for key markers known to decipher the fine architecture of the HSC compartment by segregating subsets with different functional potential. As a resource, we used this panel to provide a snapshot view of the evolution of these phenotypically defined hematopoietic compartments during the life of the animals. We show that by using a spectral cytometer, this panel is compatible with the analysis of GFP-expressing gene-reporter mice across the hematopoietic system. We leverage this tool to determine how previously described markers such as CD150, CD34, CD105, CD41, ECPR, and CD49b define specific HSC subsets and confirm that high expression of the transcription factor Gfi1 is a hallmark of the most primitive HSC compartment. Altogether, our results provide a convenient protocol to obtain in one analysis a more extensive view of the hematopoietic architecture in mouse models. Our results could also serve as a base for further development of high-end panels leveraging spectral flow cytometry beyond the 15-fluorochrome panel presented in this report. © 2020 International Society for Advancement of Cytometry

Key terms

immunophenotyping; spectral flow cytometry; mouse hematopoietic hierarchy; hematopoietic stem cell compartments; hematopoietic progenitors; aging; gene-reporter mouse model

HEMATOPOIESIS is a well-characterized step-wise process that develops from a small population of self-renewing multipotent hematopoietic stem cells (HSC) to an assembly of progenitors with diverse proliferation and differentiation potentials. Assessment of the diversity of the hematopoietic stem and progenitor cell (HSPC) compartments has become more and more refined and complex (1,2). Thus, the functional definitions of early HSPC populations have dramatically changed. Studies of HSCs self-renewal potential that were traditionally monitored through their ability to reconstitute the hematopoiesis in lethally irradiated recipients over a 4-month-period have been extended to secondary and even tertiary transplantation experiments to reveal HSC subsets with different differentiation and self-renewal potentials (3). HSPC compartments previously identified as multipotent have been established as heterogeneous and carrying early signs of lineage specification (4,5). Molecular descriptions of this heterogeneity through gene expression or epigenetic

analyses at the single cell level have uncovered new paths of lineage specification and differentiation (6). Besides these sophisticated assays, phenotypic analysis by flow cytometry remains a key tool to characterize the hematopoietic hierarchy. Notably, flow cytometry is the primary experimental assay to analyze hematopoietic disruptions associated with broad physio-pathological conditions or to characterize the impact of targeted molecular disruption in genetically modified mice. Recent years have been associated with a steady increase of the number of cell surface markers able to identify different hematopoietic cell populations and characterize their fine composition (7). However, much remains to be done in the field to compare the different phenotypic characterizations that have developed over time and used by different groups. Here, we combine several previously described phenotyping strategies that characterize multiple critical nodes of the mouse hematopoietic hierarchy from HSC subgroups to progenitors committed toward the lymphoid, granulo-macrophagic, megakaryocytic and erythroid lineages. We show that combined panel enables the direct comparison of previously described HSC subsets and provides a versatile tool for the routine analysis of the earliest mouse hematopoietic compartments.

Materials and Methods

Mice

Wild-type C57BL/6J (B6.SJL-Ptprca Pepcb/BoyJ) mice were purchased from The Jackson Laboratory (Bar Harbor, ME) (#002014) and *Gfi1-GFP* reporter mice were generously provided by Pr. Grimes (CCHMC) (8). Mice were housed at the AAALAC-accredited animal facility of the Cincinnati Children's Hospital Medical Center (CCHMC). All animal experiments were approved by the CCHMC Institutional Animal Care and Use Committee.

Flow Cytometry

Bone marrow (BM) cells were flushed from mouse femurs and tibiae and treated with ACK (150 mM NH_4Cl and 10 mM $KHCO_3$) for 2 min at 4°C to lyse red blood cells (RBC). Short RBC lysis conditions were chosen as we observed a reduction of the erythoid progenitors (CFU-E and pre-CFU-E) in harsher condition. After treatment, cells were washed using Hank's Buffered Salt Solution (HBSS, Gibco #14175-093) with 2% heat-inactivated fetal bovine serum (hereafter referred to as Staining Media, SM) and counted with a hemocytometer. For each analysis, two tubes of 10^7 unfractionated BM cells were simultaneously stained and combined for flow cytometry analysis. Reagents and optimized antibody dilutions are presented in Supplementary Table 1. BM cells were stained with unconjugated rat lineage-specific antibodies (Ter-119, Mac1, Gr-1, B220, CD5, CD3, CD4, CD8) in a volume of 500 µl of SM for 45 min at 4°C. Cells were washed with SM and stained with goat anti-rat PE-Cy5 secondary antibody in a volume of 400 µl of SM for 30 min at 4°C. After wash with SM, cells were stained with c-kit-APC-eFluor780, Sca1-PB, CD48-BV711, CD150-PE, Flk2-Biotin, FcγR-BV510, CD34-FITC, EPCR-PerCP-eFluor710, CD49b-PE/Dazzle594, CD41-BV605, CD105-APC, and CD127-BV785 antibodies in a volume of 200 µl for 30 min at 4°C in a 1:3 ratio of Brilliant Staining Buffer (BD #563-784)/SM. Secondary staining was performed with streptavidin-PE-Cy7 for 30 min at 4°C in a volume of 200 µl of SM. For dead cell exclusion, cells were washed with phosphate-buffered solution (PBS without serum, Corning #21-031-CV) and stained with Zombie NIR fixable viability kit for 15 min at room temperature. Cells were resuspended in SM and filtered through 70 µM nylon mesh before analysis. All single-stained controls, except Zombie NIR, were stained using UltraComp eBeads compensation beads used according the manufacturer's instructions (1 drop, ~50 µl) and stained with antibody concentrations listed in Supplementary Table 1. For the Zombie NIR single stained control, 10^6 healthy BM cells were mixed with 10^6 dead BM cells (obtained after 10 min treatment at 65°C) and resuspended in 100 µl Zombie NIR (1:200 dilution) for 15–30 min at room temperature. All antibody concentrations for single stained controls were optimized to ensure a brighter or equally bright signal as compared to the sample signal. Data were collected on a 4 Laser (16 Violet [405 nm] channels, 14 Blue [488 nm] channels, 10 Yellow-Green [561 nm] channels, 8 Red [640 nm] channels) Cytek Aurora spectral flow cytometer and analyzed with SpectroFlo software (Cytek Biosciences, Fremont, CA), which uses Ordinary Least Squares Linear Unmixing to deconvolute the different fluorescence spectra (9). Around 10^7 events (~10 min per sample) were recorded to ensure resolution of rare HSC populations. Comparison with "conventional" polychromatic cytometer were performed on a 5 Laser (UV [355 nm], Violet [405 nm], Blue [488 nm], Yellow-Green [561 nm], Red [635 nm]) BD LSRFortessa cell analyzer (BD Biosciences, San Jose, CA) (Supplementary Table 2). The same panel and controls were used with the exception of dead cell exclusion which was performed with Propidium Iodide (100 ng/ml) detected along with the lineage staining in the PE-Cy5 channel. Data was acquired, and compensation was performed using BD FACSDiva software (BD Biosciences).

Flow Cytometry Data Analysis

Data was analyzed using FlowJo v10.6.1 software (BD). Briefly, biexponential transformations were manually set for every fluorochrome to ensure accurate representation of event distributions and better data display. Offset histograms were presented in modal mode for better representation of small cell populations. An identical gating strategy was used for all presented samples. Time parameter was not used in the gating strategy, as no fluidic disturbances or signal anomalies were observed during sample acquisition. Gate positions were determined using fluorescence minus one (FMO) controls to delineate boundaries separating negative from positive staining. For HSC subsets defined within a continuum of marker expression, gates were adjusted based on population density to define low and high marker expressing populations. t-Distributed stochastic neighbor embedding (t-SNE) was

used as an unsupervised nonlinear dimensionality reduction method to explore and visualize the multidimensional data generated with the panel (10). tSNE analyses of individual samples were performed on indicated populations based on all parameters (excluding forward scatter, side scatter, lineage, and dead cell parameters) with default FlowJo v10.6.1 software setting (Vantage point tree Algorithm; Iterations: 1000; perplexity: 30 Learning rate (eta): 128). Representative analyses are presented. Unmixed primary FCS files and FlowJo analysis Wsp files are available upon request.

Results

Development of a 14-Color Panel Describing Early Mouse Hematopoiesis

To facilitate a deeper characterization of the mouse hematopoietic tree, we combined several "classical" hematopoietic phenotyping strategies to encompass the entire early hematopoietic hierarchy from the HSC compartment to the diverse multipotent progenitor fractions and lineage-committed progenitors segregating the lymphoid, granulo-macrophagic, megakaryocytic, and erythroid cell fates (Fig. 1A). We included the original populations described by the Weissman laboratory as marking the commitment toward the lymphoid lineages (i.e., common lymphoid progenitor, CLP) or the myeloid lineages (i.e., common myeloid progenitor, CMP; granulo-macrophagic progenitor, GMP; megakaryocytic-erythroid progenitors, MEP) (11,12) (Fig. 1B). We further deciphered the hierarchy of the myelo-erythroid progenitors by combining the markers identified by the Bryder group to visualize the divergence of the megakaryocytic and erythroid potentials (13). Within the multipotent progenitor (MPP) compartment, we used Flk2 marker (14) and the signaling lymphocyte activation molecule (SLAM) family members CD48 and CD150 (15) to separate (i) a series of functionally distinct populations (classically denoted MPP2: LSK Flk2$^-$ CD48$^+$ CD150$^+$; MPP3: LSK Flk2$^-$ CD48$^+$ CD150$^-$ and MPP4: LSK Flk2$^+$ CD48$^+$ CD150$^-$) that carry the early marks of lineage specification (4) and (ii) a population of multipotent progenitors (denoted MPP5: LSK Flk2$^-$ CD48$^-$ CD150$^-$) with limited reconstitution ability in transplantation experiments (16). We also used this set of markers to define a population denoted (HSC-SLAM: LSK Flk2$^-$ CD48$^-$ CD150$^+$) that encompass all the long-term reconstitution potential detectable within the BM hematopoietic tissue (15). To fully reveal the diversity of this population, we combined several markers described in published reports to define HSC subsets with different self-renewal potential or different lineage

(A)

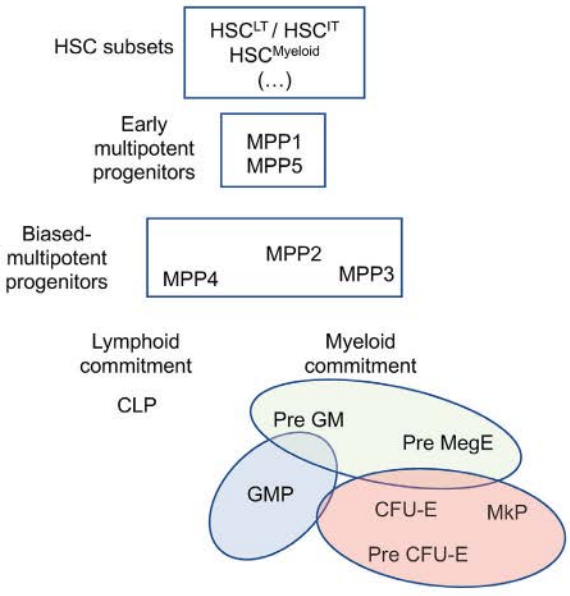

(B)

Hematopoietic Stem and Progenitor Cells: Lin^{neg} ckit$^+$ Sca1$^+$ (LSK)		
Kiel et al. *Wilson et al.* *Beneviste et al.* *Balazs et al.* *Gekas et al.* *(…)*	HSC subsets	LSK, Flk2$^-$CD48$^-$CD150$^+$CD34$^-$ CD49b / EPCR / CD41/ CD105
	MPP1	LSK, Flk2$^-$CD48$^-$CD150$^+$CD34$^+$
	MPP5	LSK, Flk2$^-$CD48$^-$CD150$^-$
	MPP2	LSK, Flk2$^-$CD48$^+$CD150$^+$
	MPP3	LSK, Flk2$^-$CD48$^+$CD150$^-$
	MPP4	LSK, Flk2$^+$
Lymphoid Progenitors		
Kondo et al.	CLP	Lin^{neg} ckit^{low} Sca1^{low} Flk2$^+$ CD127$^+$
Myeloid Progenitors: Lin^{neg} ckit$^+$ Sca1$^-$ (LK)		
Akashi et al.	GMP	LK, CD34$^+$FcgR$^+$
	CMP	LK, CD34$^+$FcgR$^-$
	MEP	LK, CD34$^-$FcgR$^-$
Pronk et al.	MkP	LK, CD150$^+$CD41$^-$
	GMP	LK, CD150$^-$CD41$^-$FcgR$^+$
	Pre GM	LK, CD150$^-$CD105$^-$CD41$^-$FcgR$^-$
	Pre MegE	LK, CD150$^+$CD105$^-$CD41$^-$FcgR$^-$
	CFU-E	LK, CD150$^-$CD105$^+$CD41$^-$FcgR$^-$
	Pre CFU-E	LK, CD150$^+$CD105$^+$CD41$^-$FcgR$^-$

Figure 1. Definition of the hematopoietic populations of interest. (**A**) Cell populations of interest characterizing the murine hematopoietic hierarchy: Schematic shows (i) the heterogeneity of the earliest hematopoietic stem cells, including long term HSC subset (HSC^{LT}) and its downstream intermediate-term progeny (HSC^{IT}) as well as a HSC subset biased toward the myeloid lineage (HSC^{Myeloid}); (ii) the most primitive MPP1 and MPP5 multipotent progenitors in addition to a series of lineage-biased multipotent progenitors, MPP2, MPP3, and MPP4 that are geared toward megakaryocytic, granulo-macrophagic and lymphoid differentiation, respectively; (iii) a compartment of lineage-committed progenitors containing the common lymphoid progenitors (CLP) that marks lymphoid-specification and a multitude of myeloid committed progenitors. This latter group includes two stages of granulocyte/macrophagic differentiation denoted PreGM and GMP as well as a hierarchy defining the megakaryocytic/erythroid (MegE) differentiation, composed of common MegE progenitors (Pre MegE) and specialized colony-forming erythroid (Pre CFU-E and CFU-E) and megakaryocytic (MkP) immature precursors. (**B**) Phenotypic characterization of various early hematopoietic stem and progenitor cell surface markers as defined by key seminal publications.

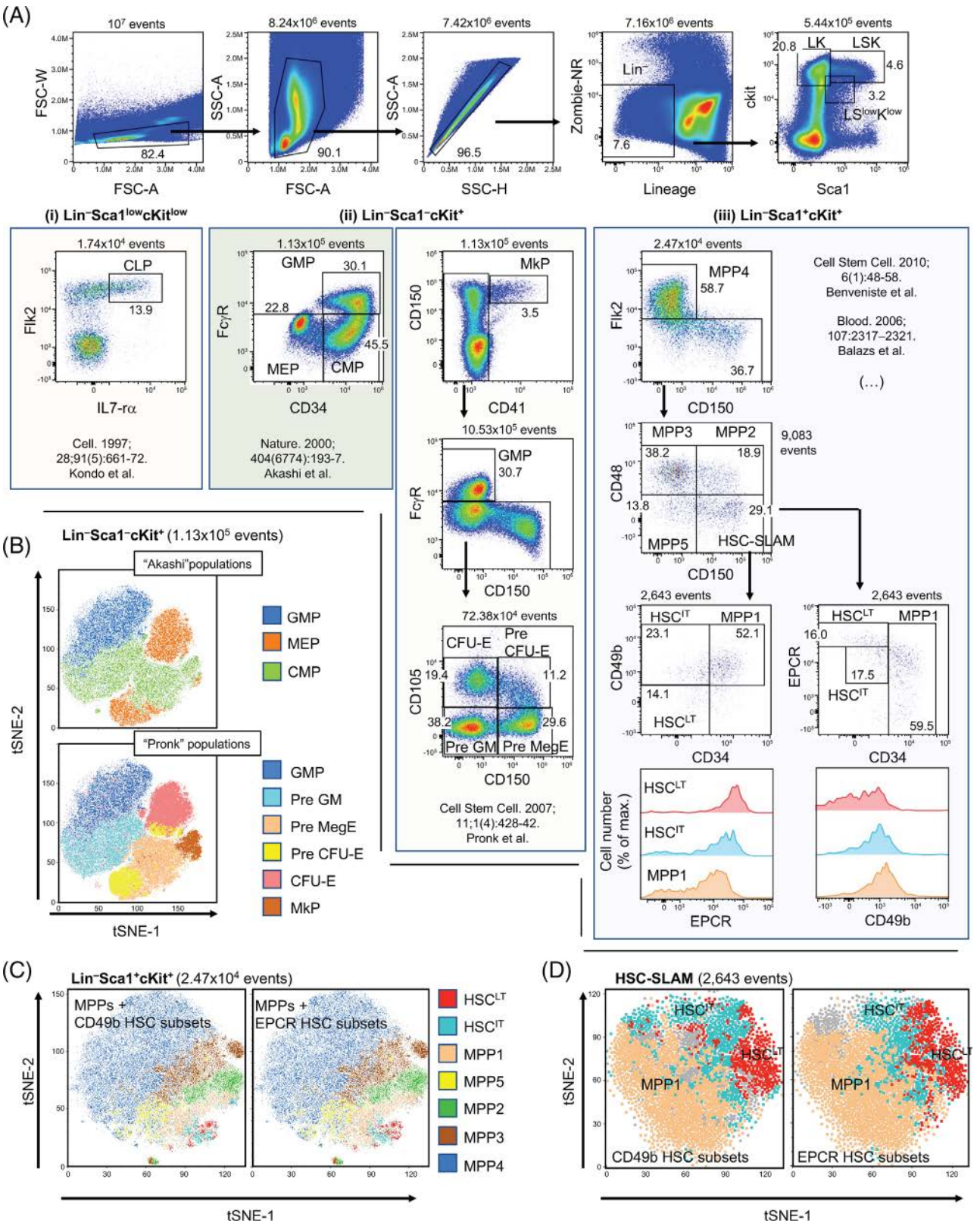

Figure 2. Combined analysis of the mouse hematopoietic stem and progenitor cell compartments. (**A**) Representative flow cytometry plots of the 14-parameter flow analysis on 8-week-old murine bone marrow (BM) cells: following erythrocyte lysis, BM cells were stained with fluorochrome-conjugated antibodies and a viability discriminator. BM cells were gated based on morphology to remove cellular debris and doublets. Lineage-negative (Lin^-) live cells were analyzed for cKit and Sca1 expression: (i) Within the $Lin^-ckit^{low}sca1^{low}$

output. This includes the CD34 marker that segregates the most immature MPP population (MPP1: LSK Flk2$^-$ CD48$^-$ CD150$^+$ CD34$^+$) with limited self-renewal potential (17). This also includes markers such as EPCR (also known as PROCR/CD201) (18,19), CD49b (Integrin α2) (20,21), CD41 (Integrin α2b) (3,22), or CD105 (Endoglin) (23,24). This particular combination of markers in one unique panel was designated to assess the phenotypic heterogeneity present in the HSC-SLAM compartment and determine how strategies used by different groups may overlap.

In our analysis, we used forward and side scatter to exclude cellular debris and doublets before investigating the cells for viability and removing mature hematopoietic cells that express one or more lineage markers (Ter119, Mac1, Gr1, B220, CD5, CD4, CD8, and CD3) (Fig. 2A). Within this lineage negative fraction, lineage-committed and multipotent progenitor fractions were defined based on the expression of c-kit and Sca1 (25,26). As previously described, CLPs were derived from the Lin^{neg} ckit^{low} Sca1^{low} fraction (Fig. 2A, left panel), myeloid-committed progenitors from the Lin^{neg} ckit$^+$ Sca1$^-$ (LK) population and the HSC/MPP populations from the Lin^{neg} ckit$^+$ Sca1$^+$ (LSK) compartment. Quality control for the spectral unmixing was performed by comparing the interaction of every parameter versus every other parameter within the live, lineage negative population (Supplementary Fig. 1). Gating for each population was determined with fluorescence minus one (FMO) controls with some adjustments based on population density or biological (different aged mice) comparisons (Supplementary Fig. 2). The results in wild-type adult mice, were consistent with previously published studies (11-13,15,27). Side-by-side comparisons between spectral and "conventional" polychromatic flow cytometers demonstrated consistent population distribution with minor differences in resolution (Supplementary Fig. 3). For the myeloid progenitors, high-dimensional analyses with tSNE (based on all parameters except lineage and live/dead) confirmed the complementarity of the panels described by Akashi et al. and Pronk et al. to study the granulo-macrophagic and erythro-megakaryocytic differentiation paths (Fig. 2A, central panel and Fig. 2B) (11,13). For the HSC compartment, we confirmed that CD49b and EPCR segregate the most immature CD34$^-$ HSC-SLAM fraction in two populations defined in the literature as long-term and intermediate-term HSCs (denoted HSC^{LT} and HSC^{IT}, respectively) (18-20) (Fig. 2A, right panel). The results demonstrates that CD49b and EPCR segregate identical populations based on percentage and cross-expression, with CD34^{lo} CD49b$^-$ HSC-SLAM showing high EPCR expression and CD34^{lo} EPCR^{high} HSC-SLAM being CD49b negative. This was graphically illustrated by tSNE which (i) segregates the different MPP populations in LSK fraction and (ii) highlights the similarity of the HSC subsets defined based on the expression of CD49b and EPCR in the HSC-SLAM population (Fig. 2C,D). Altogether, these results establish a new panel to study early mouse hematopoietic hierarchy by spectral flow cytometry.

Phenotypic Characterization of the Mouse Hematopoietic Tree at Different Ages

To further validate these results, we used the combined panel to illustrate the phenotypic changes of the hematopoietic tree occurring at different mouse stage of life (Fig. 3 and Supplementary Table 4). We included (i) 8-week-old adult mice as reference for steady-state hematopoiesis, (ii) 2-week-old mice, which correspond to a stage of quick development of the BM hematopoietic tissue characterized by the presence of cycling HSCs, (iii) 4-week-old mice when HSCs acquire their adult functional properties and finally 12-month-old mice as an example of aging hematopoiesis (28-31). We observed the expansion of the HSC-SLAM and MPP4 compartments during the transition between 2 and 4 weeks of age (Supplementary Fig. 4A and Supplementary Table 5). Adult HSC structure defined by number of HSC^{LT} and HSC^{IT} was established in 4-week-old mice (Supplementary Fig. 4B and Supplementary Table 5). As expected, we found an impairment of lymphoid specification pathway with age with progression reduction of the size of lymphoid-specified and lymphoid committed progenitors, MPP4 and CLP, respectively. 12-Month-old mice also showed the previously described expansion of the HSC-SLAM population with a dramatic reduction of the complexity of the compartment, which presents a phenotype similar to the most immature young HSCs (Fig. 3) (2). Notably, 12-month-old HSCs showed low CD34 expression and became homogeneously CD49b$^-$, EPCR^{high} and CD105$^+$. Finally, the staining confirmed that old HSCs acquired CD41, a marker of myeloid-bias and aging (22,32). Altogether, the results further validate our gating strategy for the CD49b, CD105, and CD41 makers. They highlighted the progressive transition from an HSC heterogeneous immunophenotype in young adults that reflect their functional diversity to a homogeneous phenotype in aging mice where the proposed panels failed to reveal HSC diversity.

population, the common lymphoid progenitor (CLP) was identified as described by Kondo et al. (12). (ii) Within the Lin$^-$ckit$^+$sca1$^-$ (LK) population, myeloid-committed progenitors (CMP, GMP, MEP, Pre GM, Pre MegE, Pre CFU-E, CFU-E and MkP) were identified as defined by Akashi et al. (11) or Pronk et al. (13). (iii) Within the Lin$^-$ckit$^+$sca1$^+$ (LSK) population, early (MPP1 and MPP5) and lineage-biased (MPP2/MPP3/MPP4) multipotent progenitors were identified based on CD48, CD150 and CD34 expression (17). Comparative analysis of the hematopoietic stem cells (HSC) subsets was performed based on the expression of CD34, CD49b and EPCR (18,20). Figure is representative of seven independent experiments (see Supplementary Table 3). (**B**) High-dimensional analysis with t-distributed stochastic neighbor embedding (tSNE) (based on all parameters except lineage and live/dead) confirmed the complementarity of the results described by Akashi et al. (11) and Pronk et al. (13) to study the granulo-macrophagic and erythro-megakaryocytic differentiation paths. (**C** and **D**) tSNE analyses (based on all parameters except lineage and live/dead) segregates the different MPP populations in LSK fraction and indicates the similarity of the HSC subsets defined based on the expression of CD49b and EPCR in the LSK (**C**) and HSC-SLAM population (**D**).

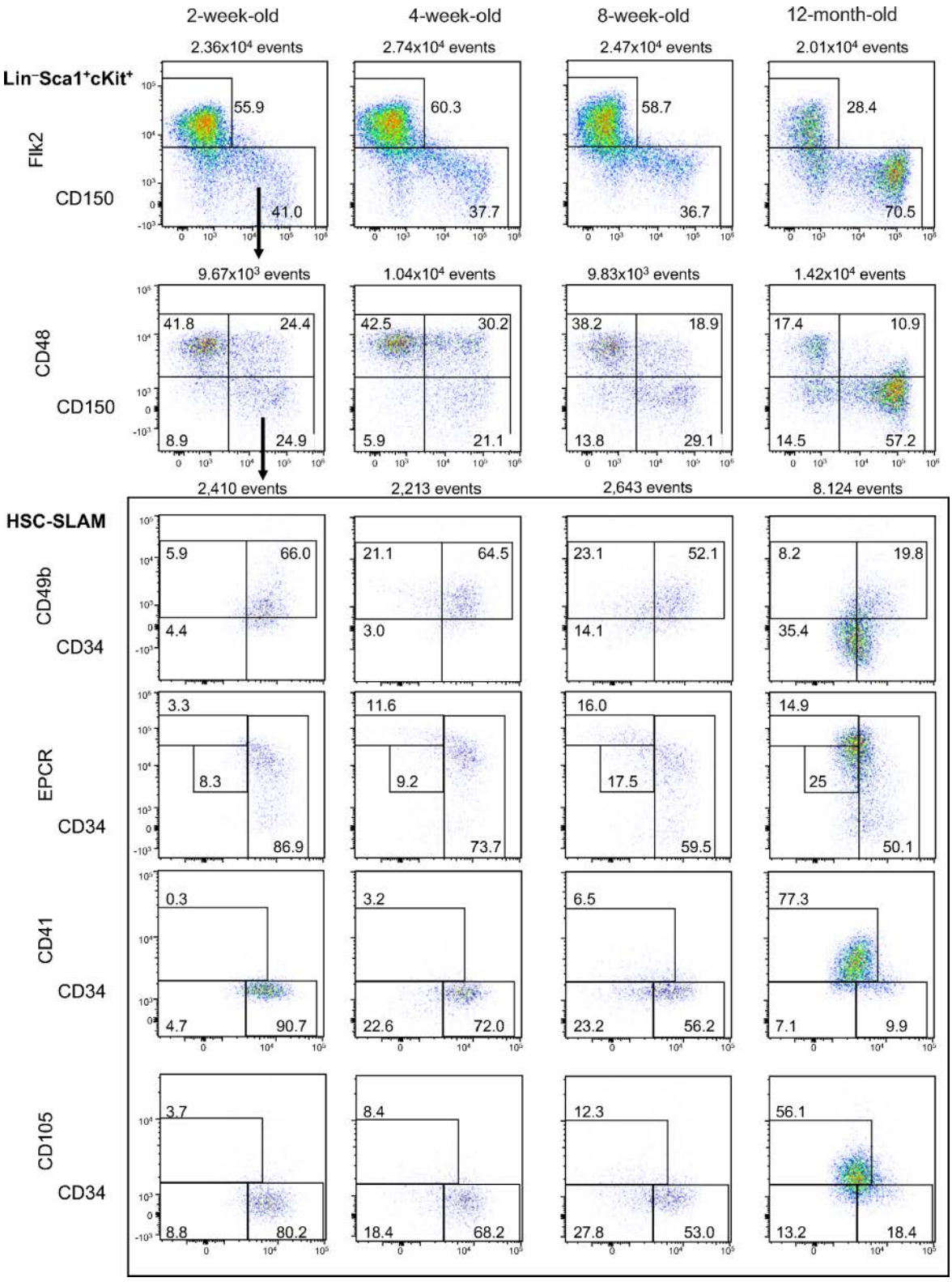

Figure 3. Complexity of the HSC compartment depending on age. Representative flow cytometry plots of the 14-parameter flow analysis on BM cells isolated from 2- and 4-week-old juvenile mice, 8-week-old adult mice and 12-month-old mice. Shown plots were gated on live LSK cells as indicated in Figure 2. Figure is representative of 3–7 independent experiments for each age group (see Supplementary Table 4).

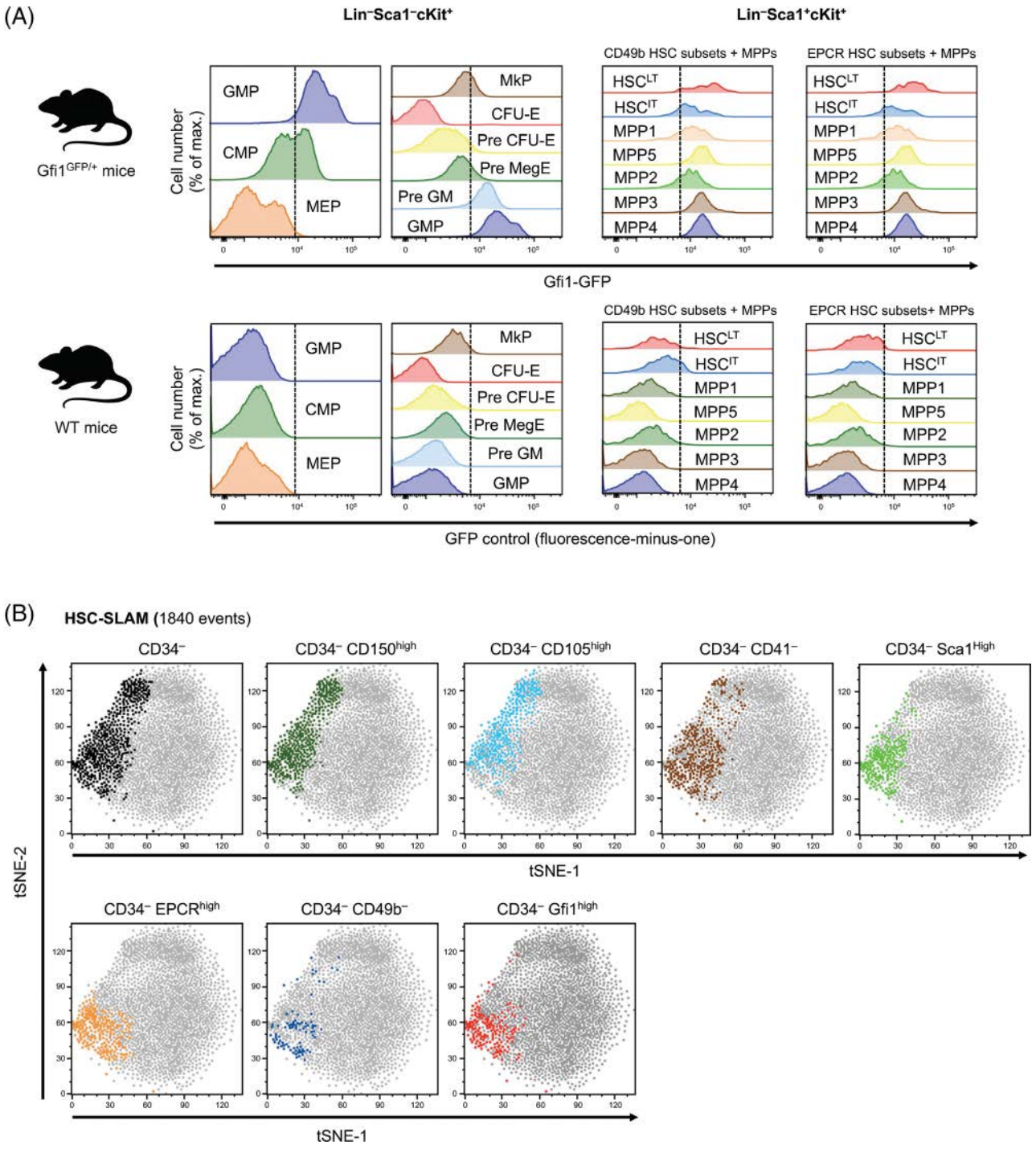

Figure 4. Gfi1 expression in hematopoietic stem and progenitor cells. (**A**) Analysis of Gfi1$^{GFP/+}$ reporter mice: Heterogeneity of Gfi1 expression in (i) various myeloid-committed progenitors defined by Akashi et al. (11) and Pronk et al. (13) (left panels) and (ii) multipotent progenitors and EPCR-/CD49b-defined HSC subsets (right panels). Lower panel shows nonspecific fluorescence detection in the GFP channel for various hematopoietic compartments in WT mice. Dash line separates negative from positive signal based on the FMO. (**B**) tSNE analyses (based on all parameters except lineage and live/dead) on HSC-SLAM population (1840 events in the gate) demonstrating how expression of CD150, CD105, CD41, Sca1, EPCR, CD49b, or Gfi1 highlight the heterogeneity of the immature CD34^{-} HSC-SLAM compartment. Figure is representative of two independent experiments.

Gfi1 as a Marker of the Most Immature HSC Subset

Finally, we investigated the compatibility of this panel for the analysis of GFP-expressing gene-reporter mice. We focused on Gfi1, a well-described transcriptional factor regulating several key cell fate decisions across the hematopoietic system (33). We used our new panel on BM cells isolated from a

knock-in Gfi1 reporter mouse that carries a GFP cassette inserted in the endogenous Gfi1 locus and allows for the monitoring of the activity of this locus at the single cell level. Despite the expected negative correlation in the negative populations due to high spectral similarity between CD34-FITC and GFP (Supplementary Fig. S5A and S5B), we were able to detect a specific GFP signal in all analyzed populations (Fig. 4A) (34). As expected for the myeloid progenitors, we found that Gfi1 expression increases during the granulo-macrophagic differentiation and conversely decreases during erythro-megakaryocytic differentiation (Fig. 4A, left panel). Similar trends were observed in the LSK fraction with the megakaryocytic-biased MPP2 showing lower Gfi1 expression than the lymphoid-biased MPP4 and myeloid-biased MPP3 (Fig. 4A, right panel). Consistent with a previous report, we confirmed that the highest Gfi1 expression occurs in the most immature HSC subset defined by CD49b and EPCR expression (35). To further illustrate this point, we used tSNE analysis to determine the most useful markers to identify the specific subsets in the $CD34^-$ HSC-SLAM compartment (Fig. 4B). This analysis confirmed that Gfi1-high expression coincides with the $CD49b^-$ $EPCR^{high}$ $CD34^{lo}$ HSC-SLAM set of cells. Lack of CD41 or high level of Sca1 expression seems to also mark the HSC^{LT} fraction, although with reduced specificity. In contrast, high level of CD150 and CD105 expression appears not discriminant into the $CD34^-$ HSC-SLAM population. Altogether, our results validate the use of our panel in GFP-expressing gene-reporter mice and confirm that Gfi1 is highly expressed in the most immature HSC subset phenotypically identified so far.

Discussion

Flow cytometry is widely used as an investigative tool to qualitatively and quantitatively assess the hematopoietic hierarchy (13,27,36). Here, we combined several previously published flow cytometry panels and used spectral flow cytometry to facilitate the analysis of the key hematopoietic nodes that reflect self-renewal and transplantation potentials as well as early specification and commitment toward the different hematopoietic lineages. This report also highlights the importance to account for the phenotypic heterogeneity of the HSC compartment to describe hematologic characteristics. Multiple phenotypic definitions of the HSC compartment can be found in the literature. Across laboratories, HSCs are defined in the LSK fraction based on the expression of (i) CD34 and Flk2, (ii) CD105, or (iii) the SLAM markers CD48 and CD150 (14,15,23,37). Further refinement of these heterogeneous compartments has been recently established based on the combination of these markers or the addition of new ones, such as EPCR, CD49b, and CD41 (18,20,22). The complex architecture of the HSC compartment and this heterogeneity of markers could be a source of misinterpretation for certain phenotypes and discrepancies between studies. By combining these markers, the described panel allows to assess the degree of phenotypic overlap between these HSC populations. We found a reassuring correlation between high expression of EPCR and the lack of expression of CD49b on $CD34^-$ HSC-SLAM, as both populations have been functionally shown to contain the most immature HSC^{LT} subset with the strongest serial transplantation ability (20,38). Similarly, low EPCR expression and CD49b acquisition indicate a downstream intermediate HSC^{IT} subset characterized functionally by time-restricted reconstitution ability (20,21). All other phenotypes based on high expression levels of CD150, Sca1, or CD105 failed to be fully discriminant in separating these two HSC subsets. We further leveraged spectral cytometry to detect GFP in the Gfi1-reporter mouse and showed that high expression of Gfi1 is a marker of the most immature HSC^{LT} subset, highlighting its known contributions to HSC functions (33,35). Finally, our results emphasize the loss of HSC-SLAM phenotypic heterogeneity associated with age as 12-month-old mice showed by the acquisition of a homogeneous $CD34^{-/lo}$ $EPCR^{hi}$ $CD49b^-$ phenotype with increased expression of CD150, CD41, and CD105. Altogether, the protocol described here aims to serve as a base for deeper phenotypic characterization of the early mouse hematopoietic compartment. The report also provides useful reference points to reconcile the multiple phenotypes described in the literature for identification of these functionally diverse hematopoietic populations.

Acknowledgments

We acknowledge the assistance of the CCHMC Research Flow Cytometry core (supported by a National Institutes of Health grant S10OD025045). This work was supported by a National Institutes of Health grant (R01HL141418) to D.R. The authors would like to thank Jamie Fellers for proofreading the manuscript.

Conflict of Interest

M.D. is an employee and receives salaries of Cytek Biosciences. M.S. and D.R. declare no competing financial interests.

Author Contributions

M.S. performed and analyzed all the experiments. M.D. provided critical insights on panel development and data analysis. D.R. conceived and supervised the project. M.S. and D.R. wrote the manuscript.

LITERATURE CITED

1. Haas S, Trumpp A, Milsom MD. Causes and consequences of hematopoietic stem cell heterogeneity. Cell Stem Cell 2018;22:627–638.
2. Jurecic R. Hematopoietic stem cell heterogeneity. Adv Exp Med Biol 2019;1169: 195–211.
3. Yamamoto R, Morita Y, Ooehara J, Hamanaka S, Onodera M, Rudolph KL, Ema H, Nakauchi H. Clonal analysis unveils self-renewing lineage-restricted progenitors generated directly from hematopoietic stem cells. Cell 2013;154:1112–1126.
4. Cabezas-Wallscheid N, Klimmeck D, Hansson J, Lipka DB, Reyes A, Wang Q, Weichenhan D, Lier A, von Paleske L, Renders S, et al. Identification of regulatory networks in HSCs and their immediate progeny via integrated proteome, transcriptome, and DNA methylome analysis. Cell Stem Cell 2014;15:507–522.
5. Rodriguez-Fraticelli AE, Wolock SL, Weinreb CS, Panero R, Patel SH, Jankovic M, Sun J, Calogero RA, Klein AM, Camargo FD. Clonal analysis of lineage fate in native haematopoiesis. Nature 2018;553:212–216.
6. Olsson A, Venkatasubramanian M, Chaudhri VK, Aronow BJ, Salomonis N, Singh H, Grimes HL. Single-cell analysis of mixed-lineage states leading to a binary cell fate choice. Nature 2016;537:698–702.

7. Morita Y, Ema H, Nakauchi H. Heterogeneity and hierarchy within the most primitive hematopoietic stem cell compartment. J Exp Med 2010;207:1173–1182.
8. Yucel R, Kosan C, Heyd F, Moroy T. Gfi1:Green fluorescent protein knock-in mutant reveals differential expression and autoregulation of the growth factor independence 1 (Gfi1) gene during lymphocyte development. J Biol Chem 2004;279:40906–40917.
9. Futamura K, Sekino M, Hata A, Ikebuchi R, Nakanishi Y, Egawa G, Kabashima K, Watanabe T, Furuki M, Tomura M. Novel full-spectral flow cytometry with multiple spectrally-adjacent fluorescent proteins and fluorochromes and visualization of in vivo cellular movement. Cytometry Part A 2015;87A:830–842.
10. van der Maaten L, Hinton G. Visualizing data using t-SNE. J Mach Learn Res 2008; 9:2579–2605.
11. Akashi K, Traver D, Miyamoto T, Weissman IL. A clonogenic common myeloid progenitor that gives rise to all myeloid lineages. Nature 2000;404:193–197.
12. Kondo M, Weissman IL, Akashi K. Identification of clonogenic common lymphoid progenitors in mouse bone marrow. Cell 1997;91:661–672.
13. Pronk CJ, Rossi DJ, Mansson R, Attema JL, Norddahl GL, Chan CK, Sigvardsson M, Weissman IL, Bryder D. Elucidation of the phenotypic, functional, and molecular topography of a myeloerythroid progenitor cell hierarchy. Cell Stem Cell 2007;1:428–442.
14. Adolfsson J, Borge OJ, Bryder D, Theilgaard-Monch K, Astrand-Grundstrom I, Sitnicka E, Sasaki Y, Jacobsen SE. Upregulation of Flt3 expression within the bone marrow Lin(−)Sca1(+)c-kit(+) stem cell compartment is accompanied by loss of self-renewal capacity. Immunity 2001;15:659–669.
15. Kiel MJ, Yilmaz OH, Iwashita T, Yilmaz OH, Terhorst C, Morrison SJ. SLAM family receptors distinguish hematopoietic stem and progenitor cells and reveal endothelial niches for stem cells. Cell 2005;121:1109–1121.
16. Pietras EM, Reynaud D, Kang YA, Carlin D, Calero-Nieto FJ, Leavitt AD, Stuart JM, Gottgens B, Passegue E. Functionally distinct subsets of lineage-biased multipotent progenitors control blood production in normal and regenerative conditions. Cell Stem Cell 2015;17:35–46.
17. Wilson A, Laurenti E, Oser G, van der Wath RC, Blanco-Bose W, Jaworski M, Offner S, Dunant CF, Eshkind L, Bockamp E, et al. Hematopoietic stem cells reversibly switch from dormancy to self-renewal during homeostasis and repair. Cell 2008;135:1118–1129.
18. Balazs AB, Fabian AJ, Esmon CT, Mulligan RC. Endothelial protein C receptor (CD201) explicitly identifies hematopoietic stem cells in murine bone marrow. Blood 2006;107:2317–2321.
19. Kent DG, Copley MR, Benz C, Wohrer S, Dykstra BJ, Ma E, Cheyne J, Zhao Y, Bowie MB, Zhao Y, et al. Prospective isolation and molecular characterization of hematopoietic stem cells with durable self-renewal potential. Blood 2009;113:6342–6350.
20. Benveniste P, Frelin C, Janmohamed S, Barbara M, Herrington R, Hyam D, Iscove NN. Intermediate-term hematopoietic stem cells with extended but time-limited reconstitution potential. Cell Stem Cell 2010;6:48–58.
21. Qian P, He XC, Paulson A, Li Z, Tao F, Perry JM, Guo F, Zhao M, Zhi L, Venkatraman A, et al. The Dlk1-Gtl2 locus preserves LT-HSC function by inhibiting the PI3K-mTOR pathway to restrict mitochondrial metabolism. Cell Stem Cell 2016;18:214–228.
22. Gekas C, Graf T. CD41 expression marks myeloid-biased adult hematopoietic stem cells and increases with age. Blood 2013;121:4463–4472.
23. Chen CZ, Li M, de Graaf D, Monti S, Gottgens B, Sanchez MJ, Lander ES, Golub TR, Green AR, Lodish HF. Identification of endoglin as a functional marker that defines long-term repopulating hematopoietic stem cells. Proc Natl Acad Sci U S A 2002;99:15468–15473.
24. Pronk CJH, Bryder D. Immunophenotypic identification of early myeloerythroid development. Methods Mol Biol 2018;1678:301–319.
25. Okada S, Nakauchi H, Nagayoshi K, Nishikawa S, Miura Y, Suda T. In vivo and in vitro stem cell function of c-kit- and Sca-1-positive murine hematopoietic cells. Blood 1992;80:3044–3050.
26. Spangrude GJ, Heimfeld S, Weissman IL. Purification and characterization of mouse hematopoietic stem cells. Science 1988;241:58–62.
27. Eich M, Trumpp A, Schmitt S. OMIP-059: Identification of mouse hematopoietic stem and progenitor cells with simultaneous detection of CD45.1/2 and controllable green fluorescent protein expression by a single staining panel. Cytometry Part A 2019;95A:1049–1052.
28. Bowie MB, Kent DG, Dykstra B, McKnight KD, McCaffrey L, Hoodless PA, Eaves CJ. Identification of a new intrinsically timed developmental checkpoint that reprograms key hematopoietic stem cell properties. Proc Natl Acad Sci U S A 2007; 104:5878–5882.
29. Bowie MB, McKnight KD, Kent DG, McCaffrey L, Hoodless PA, Eaves CJ. Hematopoietic stem cells proliferate until after birth and show a reversible phase-specific engraftment defect. J Clin Invest 2006;116:2808–2816.
30. de Haan G, Lazare SS. Aging of hematopoietic stem cells. Blood 2018;131:479–487.
31. Geiger H, Denkinger M, Schirmbeck R. Hematopoietic stem cell aging. Curr Opin Immunol 2014;29:86–92.
32. Yamamoto R, Wilkinson AC, Ooehara J, Lan X, Lai CY, Nakauchi Y, Pritchard JK, Nakauchi H. Large-scale clonal analysis resolves aging of the mouse hematopoietic stem cell compartment. Cell Stem Cell 2018;22: 600–607.e4.
33. Phelan JD, Shroyer NF, Cook T, Gebelein B, Grimes HL. Gfi1-cells and circuits: Unraveling transcriptional networks of development and disease. Curr Opin Hematol 2010;17:300–307.
34. Roederer M. Distributions of autofluorescence after compensation: Be panglossian, fret not. Cytometry Part A 2016;89A:398–402.
35. Lee JM, Govindarajah V, Goddard B, Hinge A, Muench DE, Filippi MD, Aronow B, Cancelas JA, Salomonis N, Grimes HL, et al. Obesity alters the long-term fitness of the hematopoietic stem cell compartment through modulation of Gfi1 expression. J Exp Med 2018;215:627–644.
36. Wilson NK, Kent DG, Buettner F, Shehata M, Macaulay IC, Calero-Nieto FJ, Sanchez Castillo M, Oedekoven CA, Diamanti E, Schulte R, et al. Combined single-cell functional and gene expression analysis resolves heterogeneity within stem cell populations. Cell Stem Cell 2015;16:712–724.
37. Osawa M, Hanada K, Hamada H, Nakauchi H. Long-term lymphohematopoietic reconstitution by a single CD34-low/negative hematopoietic stem cell. Science 1996; 273:242–245.
38. Gur-Cohen S, Itkin T, Chakrabarty S, Graf C, Kollet O, Ludin A, Golan K, Kalinkovich A, Ledergor G, Wong E, et al. PAR1 signaling regulates the retention and recruitment of EPCR-expressing bone marrow hematopoietic stem cells. Nat Med 2015;21:1307–1317.

ORIGINAL ARTICLE

MIFlowCyt

ISAC CYTOMETRY Journal of Quantitative Cell Science PART A

Flow cytometry: An accurate tool for screening P2RX7 modulators

Amélie Barczyk[1] | Hélène Bauderlique-Le Roy[2] | Nathalie Jouy[3] | Nicolas Renault[1] | Audrey Hottin[1] | Régis Millet[1] | Valérie Vouret-Craviari[4] | Sahil Adriouch[5] | Thierry Idziorek[3,6] | Xavier Dezitter[1]

[1]Univ. Lille, Inserm, CHU Lille, U1286 – Infinite – Institute for Translational Research in Inflammation, Lille, France

[2]Univ. Lille, UMS 2014-US 41 PLBS BICel, Flow Cytometry Core Facility, Institut Pasteur de Lille, Lille cedex, France

[3]Univ. Lille, UMS 2014-US 41 PLBS BICel, Flow Cytometry Core Facility, IRCL, 1 place de Verdun, Lille cedex, France

[4]University Cote d'Azur, Institute for Research on Cancer and Aging, IRCAN U1081 UMR CNRS 7284, Nice, France

[5]Normandie University, UNIROUEN, INSERM, U1234, Pathophysiology, Autoimmunity, Neuromuscular Diseases and Regenerative THERapies (PANTHER), Rouen, France

[6]Univ. Lille, CNRS, Inserm, CHU Lille, Institut de Recherche contre le Cancer de Lille, UMR9020 – UMR-S 1277 - Canther – Cancer Heterogeneity, Plasticity and Resistance to Therapies, Lille, France

Correspondence
Xavier Dezitter, Institut de Chimie Pharmaceutique Albert Lespagnol, Université de Lille, INSERM U1286 – Infinite – Institute for Translational Research in Inflammation, 3, rue du Professeur Laguesse BP 83, 59006 Lille, France.
Email: xavier.dezitter@univ-lille.fr

Funding information
Centre National de la Recherche Scientifique; Institut National de la Santé et de la Recherche Médicale; Institut National Du Cancer; University of Lille

Abstract

The P2X purinergic receptor 7 (P2RX7) is a poorly selective ATP-gated ion channel. Although P2RX7 binds ATP with relatively low affinity, prolonged activation can lead to nonselective membrane pore formation. Indeed, brief exposure to ATP triggers a rapid Ca^{2+} influx, whereas prolonged exposure to high ATP concentrations results in the passage of larger organic molecules. P2RX7 is involved in the physiopathology of a number of diseases and has notably emerged as a potential therapeutic target in inflammation, neuropathic pain, Alzheimer's disease, and cancer—prompting growing interest in the synthesis of novel P2RX7 modulators and the development of reliable, stringent screening methods. In the present study, we developed methods based on conventional flow cytometry, imaging flow cytometry and spectral flow cytometry and used them to measure P2RX7's activity upon activation by 3'-O-(4-benzoyl)benzoyl ATP. We also demonstrated the use of the highly sensitive DNA-intercalating dye TO-PRO-3 to determine P2RX7's large pore activity. The simultaneous quantification of calcium influx (Fluo-3 AM), large pore opening (TO-PRO-3), and viability (propidium iodide) is a very efficient method for low- to medium-throughput screening of P2RX7 modulators. Agonist and antagonist potencies can be accurately evaluated. Spectral cytometry notably enabled us to assay several biological activities while correcting for the intrinsic fluorescence of the screened compounds—otherwise a well-known limitation of fluorescence-based screening. Hence, spectral cytometry appears to be a useful, novel tool for drug candidate screening.

KEYWORDS
drug discovery, flow cytometry, imaging flow cytometry, P2RX7, screening, spectral cytometry

1 | INTRODUCTION

The P2X purinergic receptor 7 (P2RX7) is a poorly selective ATP-gated ion channel that binds ATP with relatively low affinity. In humans, P2RX7 is expressed in many cell types, including immune cells (macrophages and microglia) and cells in the central and peripheral nervous systems [1]. P2RX7 has an essential role in inflammation, innate immunity, tumor progression, neurodegenerative diseases, and several other diseases [1].

Brief exposure of P2RX7 to extracellular ATP induces rapid channel opening and thus Ca^{2+} and Na^{+} influx, and K^{+} efflux. In contrast,

Amélie Barczyk, Hélène Bauderlique-Le Roy, and Nathalie Jouy contributed equally to this work.

prolonged exposure to ATP leads to the formation of a poorly selective membrane pore that allows the passage of molecules of up to 900 Da in weight. For decades, two competing mechanistic hypotheses were considered with regard to the large pore opening: [2–4] the enlargement of the P2RX7 cation channel, and the recruitment of a partner protein (e.g., pannexin-1) [5]. It is now acknowledged that upon activation, P2RX7's ion channel becomes immediately permeable to large molecules. [6–10]

P2RX7 signalling affects major cell functions and cell fate and depends on the cellular context. In the setting of inflammation, P2RX7 activation triggers inflammasome assembly and release of pro-inflammatory cytokines (such as IL-1β and IL-18) [11,12]. In many cell subtypes (including tumor cell lines in vitro), P2RX7 acts as a cell death inducer by disrupting plasma membrane permeability [13]. In vivo, P2RX7's role in tumor progression and metastasis is more complex, and depends on (i) tumor microenvironment factors (e.g., the extracellular ATP concentration, or the type and abundance of ecto-ATPase), and (ii) the expression levels and functional status of the P2RX7 variants expressed at the surface of tumor cells [14–17]. Adding to this complexity, tonic low-level P2RX7 activation in cancer cells is associated with faster in vivo tumor growth; indeed, in some models, P2RX7 antagonists have antitumor effects [16,18]. In the mouse, however, P2RX7 knock-out, loss-of-function *P2RX7* gene polymorphisms, and pharmacological inhibition are associated with tumor progression, due to the impairment of antitumor immune responses [19–21]. The net effect of P2RX7 pharmacological modulation on tumor progression therefore appears to depend on the type of cancer and on the balance between direct pharmacological effects on cancer cells and impairment of the host immune system [22].

Despite the complexity of the purinergic pathways, decades of accumulated scientific evidence have prompted the scientific community and pharmaceutical companies to develop P2RX7 modulators as drug candidates in the treatment of cancer, inflammatory diseases, and other emerging clinical indications. These drug candidates range from small molecules to P2RX7-specific antibodies and nanobodies [23,24]. The reliable, stringent screening of drug candidates is therefore essential in this context. P2RX7 pharmacology has been intensely studied with electrophysiological methods (e.g., patch-clamp techniques) and microscopy- or microplate-based fluorescent dye assays. The P2RX7 ion channel has mainly been studied using electrophysiological techniques (whole-cell current clamping), but automated patch clamp is necessary for screening large series of compounds. P2RX7-mediated calcium influx has also been studied in microscopy- or microplate-based assays with fluorescent probes like Fluo-3 AM or Fluo-4 AM [4]. The opening of P2RX7 large pore is usually measured through the entry of high-molecular-weight cationic fluorescent dyes (such as ethidium [394 Da as ethidium bromide], propidium [668 Da as propidium iodide, PI], or YO-PRO-1 [629 Da as YOPRO-1 iodide]) or anionic fluorescent dyes (such as Lucifer yellow [457 Da as the lithium salt] or fluorescein [376 Da as the sodium salt]) [4]. These dye uptake assays are suitable for high-throughput screening.

Flow cytometry has already been used to separately measure calcium influx and dye uptake in independent experiments [25–28]. In the present study, we used flow cytometry to simultaneously assess Ca^{2+} influx, large pore opening, and cell viability upon activation of P2RX7 by 3'-O-(4-benzoyl)benzoyl ATP (BzATP). Flow cytometry has the advantage of excluding dead cells that interfere with the measurement of large pore opening. The simultaneous quantification of both calcium influx (high Ca^{2+}) and large pore opening proved to be an excellent method for compound screening and for measuring the potency (as the half maximal effective concentration EC_{50} or the half maximal inhibitory concentration IC_{50}) of both agonists and antagonists. Furthermore, we better defined the biological activity of compounds of interest by exploiting the advantageous properties of spectral cytometry.

2 | MATERIALS AND METHODS

2.1 | Reagents

BzATP was purchased from Sigma-Aldrich (St. Louis, MO). AZ11645373 was purchased from Tocris (Ellisville, MO). The fluorescent dyes Fluo-3 AM, YO-PRO-1, TO-PRO-3, PI, 7-AAD and Hoechst 33342 were purchased from Life Technologies (Carlsbad, CA). The synthesized compounds were prepared in DMSO.

2.2 | Cell culture

HEK-293 cells stably expressing human or mouse P2RX7 were established as described [29]. The cells were cultured in DMEM medium with Glutamax (Life Technologies), supplemented with 10% heat-inactivated foetal calf serum, 1000 UI/ml penicillin, 1000 µg/ml streptomycin and incubated at 37°C in 5% CO_2. Stable cell lines were grown in medium supplemented with 5 µg/ml blasticidin (Sigma-Aldrich), in order to select P2RX7-overexpressing cells.

2.3 | Fluorescence analysis using a plate reader

For intracellular calcium concentration measurement, the cells were harvested and loaded (10^6 cells/ml) with the calcium indicator Fluo-3 AM (500 nM) for 30 min in culture medium without foetal calf serum at 37°C. The cells were then centrifuged at 230*g* for 5 min and resuspended in sucrose buffer (20 mM HEPES, 300 mM sucrose, 5 mM KCl, 1 mM $MgCl_2$, 1 mM $CaCl_2$, 10 mM glucose, and pH 7.4) and placed in a 96 well plate. The cells were treated with BzATP and the fluorescence intensity was measured with a Varioskan Flash multimode reader (Thermo Fisher Scientific, Waltham, MA), with a 490 nm excitation wavelength and an emission at 530 nm.

For YO-PRO-1 uptake assay, the cells were harvested, centrifuged at 230*g* for 5 min and resuspended in sucrose buffer (20 mM HEPES, 300 mM sucrose, 5 mM KCl, 1 mM $MgCl_2$, 1 mM $CaCl_2$, 10 mM glucose, and pH 7.4) in the presence of YO-PRO-1 (1 µM) and placed in a 96 well plate. The cells were treated with BzATP and the

fluorescence intensity was measured with a Varioskan Flash multimode reader (Thermo Fisher Scientific), with a 470 nm excitation wavelength and an emission at 509 nm.

2.4 | Flow cytometry analysis

2.4.1 | Multiple staining with Fluo-3 AM, TO-PRO-3, and PI

Intracellular calcium concentration and large pore opening were assessed by flow cytometry analysis using, respectively, Fluo-3-AM fluorescent dye and the membrane impermeant DNA-intercalating dye TO-PRO-3 (Life Technologies). Briefly, the cells (10^6 cells/ml) were loaded with Fluo-3 AM (50 nM) for 30 min in culture medium without foetal calf serum at 37°C. The cells were then centrifuged at 230*g* for 5 min and resuspended in sucrose buffer (20 mM HEPES, 300 mM sucrose, 5 mM KCl, 1 mM $MgCl_2$, 1 mM $CaCl_2$, 10 mM glucose, and pH 7.4) containing TO-PRO-3 (10 nM) and PI (75 nM). The cells (10^5 in 200 µl) were treated with BzATP and/or different compounds for 1 h at room temperature and analysed using flow cytometry. In some experiments, the impermeant DNA-intercalating dye YO-PRO-1 was used at 10 nM instead of TO-PRO-3 (without Fluo-3 AM). We used a lower concentration of Fluo-3 AM in flow cytometry (50 nM) than in the microplate reader analysis (500 nM) because the former method is more sensitive. The concentration of 50 nM was sufficient and reduced the percentage compensation in the FL3 filter used to detect PI.

The staining index was defined as the difference between the positive staining and the (negative) background signal, divided by twice the standard deviation of the background signal. To estimate the staining indexes of the dyes without interfering with their ability to enter through P2RX7, unlabelled dead cells were taken as negative controls and labeled dead cells were taken as positive controls.

Staining index = $(MFI_{Positive\ cells} - MFI_{Negative\ cells})/(2 \times \text{standard deviation } MFI_{Negative\ cells})$ as previously described. [30]

2.4.2 | Conventional flow cytometry

Conventional cytometry was performed with a CyAn ADP LX9 flow cytometer running Summit analytical software (Beckman Coulter, Miami, FL). Fluo-3 AM and PI were excited by the blue laser (488 nm) and the emission fluorescences were acquired with FL1 (530/40 nm) and FL3 (613/20 nm) filters, respectively. TO-PRO-3 was excited by the red laser (633 nm) and TO-PRO-3 emission fluorescence was acquired with an FL8 (665/20 nm) filter. Highly PI-positive cells were considered as dead cells and gated out using Summit analysis software.

2.4.3 | Imaging flow cytometry

Imaging flow cytometry was performed on Imagestream^X MarkII imaging flow cytometer (AMNIS, Millipore, Seattle, WA). Twenty thousand cells were collected for each sample in INSPIRE acquisition software. Laser powers were adjusted as follows in order that the fluorophore intensities are in the detection range: 375 nm: 70 mW; 488 nm: 129 mW; 561 nm: 100 mW; 642 nm: 50 mW; 785 nm: 1.75 mW. Fluorescent signals were collected as follows. Brightfield images were measured in channels 1 (430–470 nm) and 9 (575–595 nm). Fluo-3 AM was excited with the 488 nm laser (129 mW) and fluorescence was measured in channel 2 (470–560 nm). PI was excited with the 561 nm laser (100 mW) and fluorescence was measured in channel 4 (595–660 nm). TO-PRO-3 was excited with the 642 nm laser (50 mW) and fluorescence was measured in channel 11 (660–720 nm). Hoechst 33342 was excited with the 375 nm laser (70 mW) and fluorescence was measured in channel 7 (430–505 nm). Side scatter was probed at 785 nm, and fluorescence was measured in channel 12 (720–800 nm). IDEAS analysis software was used for analysis. Highly PI-positive cells were considered as dead cells and gated out.

2.4.4 | Spectral cytometry

Spectral flow cytometry was performed with an SP6800 spectral cell analyser using SP6800 software (Sony Biotechnology, San Jose, CA). The SP6800 is equipped with 488, 405 and 638 nm lasers. It uses 10 consecutive prisms to spread the emitted fluorescence from individual cells and 32-channel photomultiplier tubes to measure the fluorescence spectrum from 420 nm to 800 nm. Full spectra of unstained cells (autofluorescence) or single-positive cells were analysed with 488, 405, and 638 nm laser excitations and used as references for the spectral unmixing algorithm based on the weighted least squares method (WLSM) [31,32]. The spectrum of the unstained cells was used as the universal negative reference. Based on each dye reference spectrum, the unmixing algorithm was used to calculate the fluorescence intensity of each dye in multistained samples. Ten thousand cells were analysed in each sample. Highly PI-positive cells were considered to be dead cells and were gated out using SP6800 analysis software.

2.4.5 | P2RX7 expression analysis

For P2RX7 expression, HEK-293 cells (10^6 cells/ ml) were saturated in PBS, 3% BSA at room temperature and stained with anti-human P2RX7 monoclonal antibody (cell supernatant) [33] and Alexa Fluor 488-conjugated anti-mouse IgG secondary antibody at room temperature for 30 min. The cells were then centrifuged at 230*g* for 5 min and resuspended in sucrose buffer (20 mM HEPES, 300 mM sucrose, 5 mM KCl, 1 mM $MgCl_2$, 1 mM $CaCl_2$, 10 mM glucose, pH 7.4) containing TO-PRO-3 (10 nM) and PI (75 nM). The cells (10^5 in 200 µl) were treated with BzATP for 1 h at room temperature and analysed using flow cytometry.

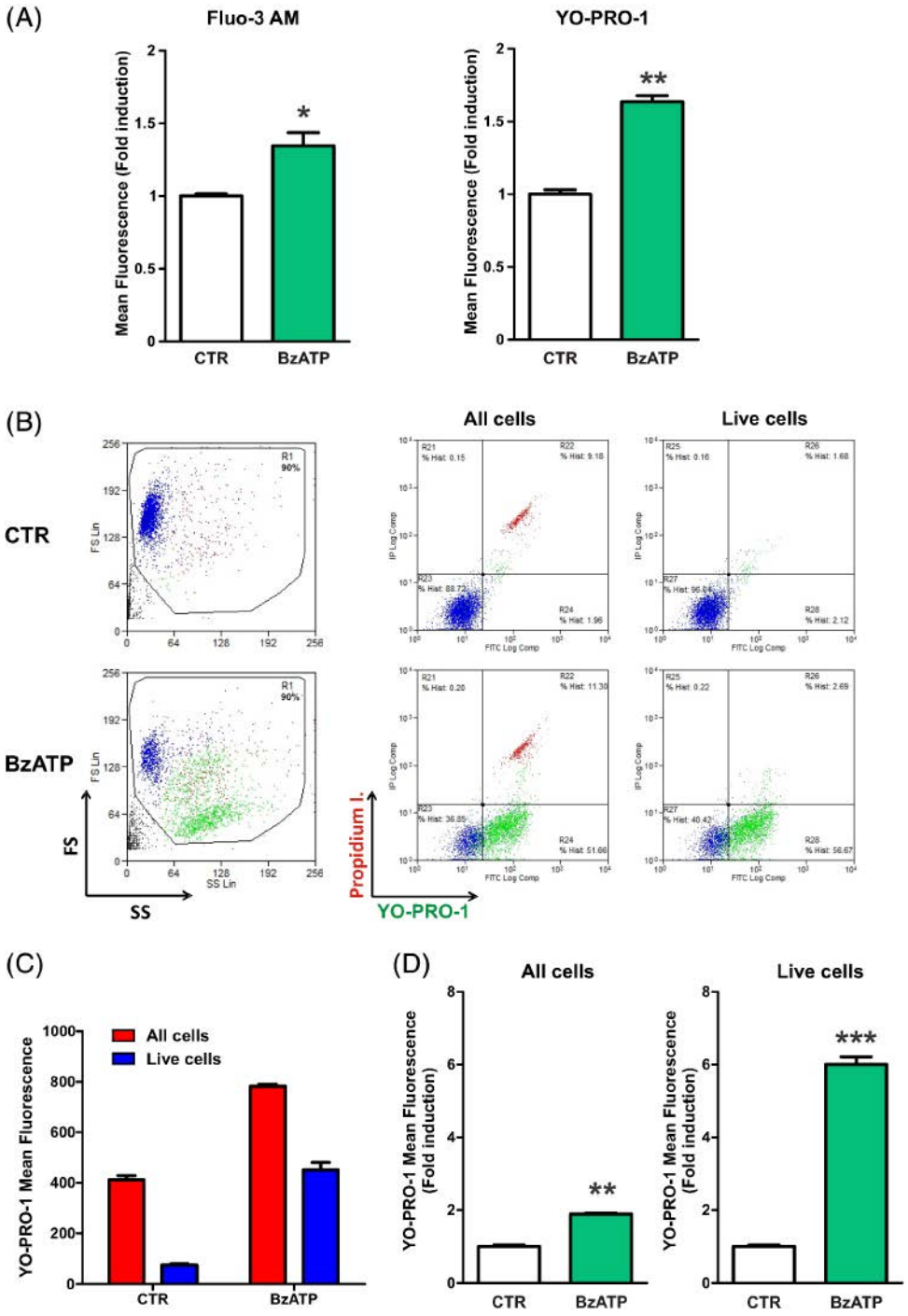

FIGURE 1 Determination of P2RX7 activity by the use of fluorescent dyes in a microplate assay or a flow cytometry assay. (A) HEK-293 cells overexpressing human P2RX7 were stained with the calcium indicator Fluo-3 AM (left panel) or incubated in the presence of the nonpermeant DNA-intercalating dye YO-PRO-1 (right panel) before addition of the P2RX7 agonist BzATP (100 μM) for 10 min (Fluo-3 AM, left panel) or 1 h (YO-PRO-1, right panel). Fluorescence was measured with the microplate reader VarioSkan and plotted as a fold induction relative to control cells. The results are representative of three independent experiments (*$p < 0.05$; **$p < 0.01$). (B) HEK-293 cells overexpressing human P2RX7 were incubated with the non-permeant DNA-intercalating dyes YO-PRO-1 (large pore opening) and PI (cell viability) before addition of the P2RX7 agonist BzATP (100 μM) for 1 h. The cells were then analysed using flow cytometry (with the CyAn cytometer from Beckman Coulter). Two-parameter plots of size versus structure parameters (FS/SS) and YO-PRO-1 versus PI fluorescence of nontreated cells (CTR) or cells treated with BzATP (100 μM) were created with Summit software. High PI (dead) cells were coloured in red and PI-negative (live) cells were colored in blue with Summit software. The cells presenting a size decrease in the presence of BzATP were arbitrary colored in green with Summit software. (C) Histograms represent YO-PRO-1 mean fluorescence in all cells or in live (PI-negative) cells in the presence or absence of BzATP from Figure 1 (B). (D) The YO-PRO-1 fluorescence was plotted as a fold induction relative to control cells in all cells and in live cells. The results are representative of three independent experiments (**$p < 0.01$; ***$p < 0.001$) [Color figure can be viewed at wileyonlinelibrary.com]

2.5 | Three-dimensional molecular models

Marvin software (version 17.29.0, http://www.chemaxon.com) was used for 3D conversion and conformer generation. Scatter plots were produced with DataWarrior (version 4.5) [34], and 3D representations were displayed using UCSF Chimera. [35]

2.6 | Statistical analysis

The results are expressed as the mean ± SEM of three separate replicate experiments. Levels of significance were evaluated using Student's *t*-test. The threshold for statistical significance was set to $p < 0.05$. All analyses were performed with GraphPad Prism 5 software (GraphPad Software, San Diego, CA).

3 | RESULTS

3.1 | Assessment of P2RX7's large pore activity in a flow cytometry assay

In order to measure the biological activity of molecules synthesized as potential P2RX7 modulators, we developed an assay in HEK-293 cells stably expressing human P2RX7. First, we used a microplate reader to assay the intracellular calcium concentration (using the calcium indicator Fluo-3 AM) and large pore opening (using YO-PRO-1). The cells were stimulated with the potent agonist BzATP in a sucrose buffer—a commonly used buffer for pharmacological studies of P2RX7 [25,36,37]. As expected, we observed increases in intracellular calcium content (Figure 1(A), left panel) and YO-PRO-1 uptake (Figure 1(A), right panel). Despite the statistical significance of the observed differences ($^{*}p < 0.05$, $^{**}p < 0.01$ in the figure), we further developed a flow cytometry assay in an attempt to increase the sensitivity of YO-PRO-1 dye measurement (Figure 1(B)). Two-parameter plots of forward scatter (FS) versus side scatter (SS) highlighted a single-cell population in control samples, and the appearance of a new cell population (characterized by cell shrinkage and increased granularity) in the presence of BzATP (the cells arbitrary colored in green). We then performed a YO-PRO-1 uptake assay in the presence of a low concentration (75 nM) of the cell viability marker propidium iodide. In control experiments (i.e., in the absence of a P2RX7 agonist), YO-PRO-1 versus PI two-parameter plots evidenced a cell population that incorporated large amounts of YO-PRO-1. PI staining indicated that these cells were dead; hence, YO-PRO-1-high cells not exposed to a P2RX7 agonist are necrotic cells with a disrupted plasma membrane (high YO-PRO-1/high PI; the red cells on the graph). In live (i.e., PI-negative) cells, the addition of BzATP induced cell shrinkage (the green cells in the FS/SS plot) and YO-PRO-1 uptake (attesting to large pore opening). It was therefore possible to discriminate between dead cells (the high YO-PRO-1/high PI red cells on the graph) and P2RX7-activated cells (the YO-PRO-1-positive/PI-negative, green cells on the graph) by using YO-PRO-1 and a low PI concentration. It is noteworthy that under our experimental conditions, a 1 h incubation with BzATP did not induce significant cell death. We next took advantage of flow cytometry's ability to gate out dead (PI-positive) cells that were strongly stained by YO-PRO-1 (i.e., independently of P2RX7 activation). By gating out dead cells, we removed the high background level of YO-PRO-1 staining (Figure 1(C)), enhanced the specificity of the signal upon BzATP treatment (Figure 1(D)), and increased both the sensitivity (a sixfold increase, relative to the control), statistical significance ($^{***}p < 0.001$), and reproducibility of the method for studying large pore opening versus a microplate assay (Figure 1(A), right panel).

3.2 | A flow cytometry assessment of P2RX7-mediated fluorescent dye uptake

In order to determine the most suitable dye for a flow cytometry assay, we compared the uptake of various fluorescent dyes after the addition of BzATP (Figure 2). HEK-293 cells overexpressing human P2RX7 were incubated in the presence of increasing concentrations of YO-PRO-1 (629 Da; 375 Da as a cation), PI (668 Da; 414 Da as a cation), and 7-aminoactinomycin D (7-AAD; 1270 Da, uncharged), together with BzATP (Figure 2(A) + Supporting Information Figure S1 for the histograms). We also assessed the uptake of the red fluorescent dye TO-PRO-3—a monomeric cyanine nucleic acid stain that is structurally similar to YO-PRO-1 and has much the same molecular weight (671 and 629 Da for TO-PRO-3 and YO-PRO-1, respectively; 417 Da as a cation for TO-PRO-3). As previously shown in Figure 1(B), YO-PRO-1 and TO-PRO-3 uptakes were measured in the presence of low concentrations of PI (75 nM). High YO-PRO-1/high TO-PRO-3/PI-positive cells (corresponding to dead cells) were gated out. In order to study BzATP-induced uptake of increasing concentrations of PI (1 nM to 1 μM) by live cells, we checked whether PI staining was associated with an increase in Fluo-3 AM staining (Supporting Information Figure S2). The high-molecular-weight dye 7-AAD was used as a negative control, since it does not enter cells through P2RX7. BzATP-induced TO-PRO-3 staining was observed in the presence of 1 nM TO-PRO-3, whereas YO-PRO-1 uptake was visible in the presence of concentrations above 10 nM (Figure 2(A) + Supporting Information Figure S1 for histograms). Propidium uptake was weak at 100 nM. Nevertheless, BzATP-induced PI staining in live cells was detected at concentrations above 1 μM, whereas 10 nM was sufficient to stain dead cells (Supporting Information Figure S2). We therefore chose to use a low concentration of PI, in order to selectively identify dead cells with little (if any) P2RX7-dependent uptake under our experimental conditions. TO-PRO-3 was therefore the most sensitive fluorescent dye for assessing large pore opening.

We also estimated each compound brightness by calculating the corresponding staining index [30]. Using this method, TO-PRO-3 appeared to be brighter than YO-PRO-1 in the low concentration range—explaining TO-PRO-3 higher sensitivity (Figure 2(B)). Above 100 nM, high PI brightness was effective for staining dead cells and the P2RX7-mediated uptake was weak. Given that the YO-PRO-1,

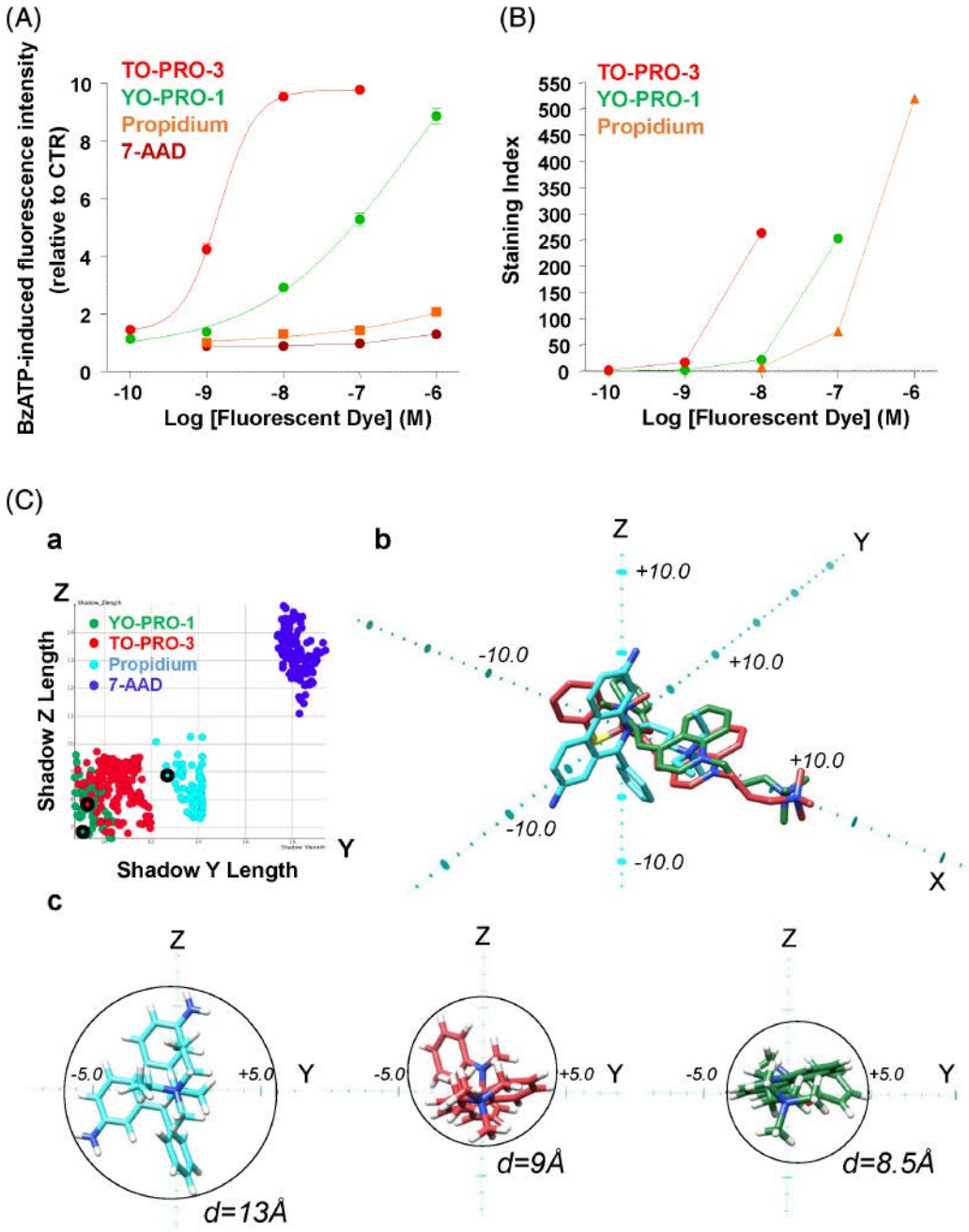

FIGURE 2 A flow cytometry assessment of P2RX7-mediated fluorescent dye uptake. (A) HEK-293 cells overexpressing human P2RX7 were incubated in the presence of increasing concentrations of the nonpermeant DNA-intercalating dyes YO-PRO-1, TO-PRO-3, propidium iodide and 7-AAD in the presence of the P2RX7 agonist BzATP (100 μM) for 1 h. The cells were then analysed using flow cytometry (with the CyAn cytometer). Dye fluorescence was plotted as a fold induction relative to control cells. (B) Line graph representing the staining index of the indicated dyes at different concentrations. Dead cells were taken as high-positive cells. The results are representative of three independent experiments. (C) Structural insights for pore permeation through human P2RX7. (a) According to the best-discriminating Y/Z area for each P2RX7 probe (see other X/Y and X/Z planes in supplemental information), relevant conformers can be viewed in three (b) and in two (the Y/Z plane) (c) dimensions in order to extrapolate the minimal diameter *d* for permeation through P2RX7 [Color figure can be viewed at wileyonlinelibrary.com]

TO-PRO-3 and propidium dications have similar molecular weights, one would expect them all to permeate through P2RX7 large pore in a similar way. We hypothesized that the enhanced uptakes of YO-PRO-1 and TO-PRO-3 were linked to their linear three-dimensional structure; in contrast, propidium broader three-dimensional structure might disfavor permeation through the pore (Supporting Information Figure S3). We therefore compared the shadow projections of all the possible structural conformations of 7-AAD, YO-PRO-1, TO-PRO-3 and propidium with our experimental results. This analysis confirmed that 7-AAD conformers have much greater dimensions than the other

molecules, which prevents this dye from passing through the pore. YO-PRO-1 and TO-PRO-3 conformers can be easily distinguished from propidium conformers in two intersecting planes (X/Y and Y/Z). Despite its equivalent molecular weight, propidium has at least one dimension greater than 13 Å in each intersecting plane. In contrast, YO-PRO-1 and TO-PRO-3 conformers have at least one dimension of between 7 and 9 Å in two intersecting planes; this might favor their permeation through P2RX7. According to the best-discriminating Y/Z area for each P2RX7 probe (Figure 2(C,a)), relevant conformers can be viewed in three dimensions (Figure 2(C,b)) and in two dimensions (the Y/Z plane, Figure 2(Cc)); this extrapolates the minimum diameter *d* for permeation through P2RX7. YO-PRO-1 (*d* = 8.5 Å) and TO-PRO-3 (*d* = 9 Å) are more elongated than propidium (*d* = 13 Å); this might facilitate the permeation of YO-PRO-1 and TO-PRO-3 through the receptor and thus explain the staining observed in the presence of BzATP. With regard to P2RX7-mediated uptake, the fluorescent dyes' molecular structures and dimensions therefore appear to be more important than their molecular weights.

3.3 | The kinetics of P2RX7 cation channel and large pore activities

In view of TO-PRO-3 high sensitivity and the overlapping emission wavelengths for the calcium indicator Fluo-3 AM and the commonly used YO-PRO-1 dye (526 and 509 nm, respectively), we chose to combine the red DNA-binding dye TO-PRO-3 (emission wavelength: 661 nm) with the green Fluo-3 AM dye in order to simultaneously assess P2RX7 calcium channel and large pore activities (Figure 3(A)). Simultaneous PI staining was also used to gate out dead cells. This kinetic study revealed that the BzATP-induced, rapid Ca^{2+} influx (observed after 1 min) in all cells was followed by the progressive appearance of two distinct cell populations over the next hour. In one cell population, the Ca^{2+} level returned to baseline. The second cell population slowly incorporated TO-PRO-3 dye—attesting to the opening of the large pore. After a 1-h incubation with BzATP, cells displaying Fluo-3 AM/TO-PRO-3 double-positive staining were clearly seen; this allowed a stringent evaluation of P2RX7 activation (49% of the cells). Staining with an anti-P2RX7 antibody demonstrated that BzATP-exposed, TO-PRO-3-positive cells expressed higher membrane levels of P2RX7 (Figure 3(B))—clearly linking receptor expression to large pore opening. Cell shrinkage and an increase in granularity appeared between 5 and 10 min after BzATP addition (Supporting Information Figure S4(A)). The cell shrinkage observed in the presence of BzATP in sucrose buffer might be linked to P2RX7-mediated K^+ depletion, [38] since it was prevented by reduction of the potassium electrochemical gradient (i.e., the use of sucrose buffer supplemented with 140 mM KCl) and induced by addition of the potassium ionophore nigericin (Supporting Information Figure S5). As mentioned above, cell viability did not change significantly during this 1 h period (Supporting Information Figure S4(B)). P2RX7's functional activities and the associated changes in cell morphology were confirmed by imaging flow cytometry (Supporting Information Figure S6). Treatment with BzATP was associated with the appearance of the Fluo-3 AM/TO-PRO-3 double-positive cell population and elevated granularity (dark field, side scatter [SS]). Bright-field images evidenced a lower cell size, blebbing, and greater granularity in the presence of BzATP, relative to control cells.

We used Fluo-3 AM/TO-PRO-3/PI triple staining to measure BzATP potency (i.e., the EC_{50}) on both human and mouse P2RX7 (Figure 3(C)). The mean ± SEM EC_{50} of BzATP in sucrose buffer was 31 ± 3 μM for human P2RX7 and 16 ± 2 μM for mouse P2RX7; these values are in line with the literature data. [39] Quantification of double-positive cells (with high Ca^{2+} influx and large pore opening) proved to be an excellent method for assaying a drug candidate's biological effects on P2XR7 variants that form large pores. [15] The method takes account of cell viability and is therefore suitable for measuring early and late P2RX7-mediated events in the same tube.

3.4 | Screening of potential P2RX7 antagonists

We used Fluo-3 AM/TO-PRO-3/PI triple staining to screen our newly synthesized compounds, two of which are referred to hereafter as compound A and compound B (Figure 4). BzATP-induced Fluo-3 AM/TO-PRO-3 double staining was inhibited by the reference antagonist AZ11645373 [40] and several new compounds, including compound A (Figure 4(A)). These compounds inhibited BzATP-induced morphological changes and did not induce cell death (Supporting Information Figure S7). Our results indicate that this method is very sensitive and allows the accurate measurement of the half maximal inhibitory concentration (IC_{50}) of P2RX7 antagonists (Figure 4(B), IC_{50} = 459 nM for compound A). The addition of compound B alone induced an increase in Fluo-3 AM fluorescence—suggesting that it is a calcium channel agonist (Figure 4(A)). After the further addition of BzATP, the cells did not incorporate TO-PRO-3 dye but were still positive for Fluo-3 AM. At first sight, therefore, compound B inhibited the large pore activity and stimulated calcium influx. However, comparison of compound-B-treated cells with non-treated cells in the absence of Fluo-3 AM and TO-PRO-3 indicated that compound B had intense intrinsic fluorescence (Figure 4(C)). This was detected in the FL1 channel (530 ± 30 nm) used to quantify Fluo-3 AM. Thus, compound B's green fluorescence interfered with calcium content measurement and prevented us from drawing any conclusions about its effect on P2RX7 calcium channel activity.

3.5 | A multiparameter spectral flow cytometry analysis of P2RX7 activity

In order to take account of compound B intrinsic fluorescence (Figure 4(A,C)), we performed experiments with a spectral flow cytometer (SP6800, Sony Biotechnology). In contrast to conventional flow cytometers (which detect the fluorochrome emission peak with dichroic mirrors and band-pass filters), spectral flow cytometry enables the whole emission fluorescence spectrum to be analysed

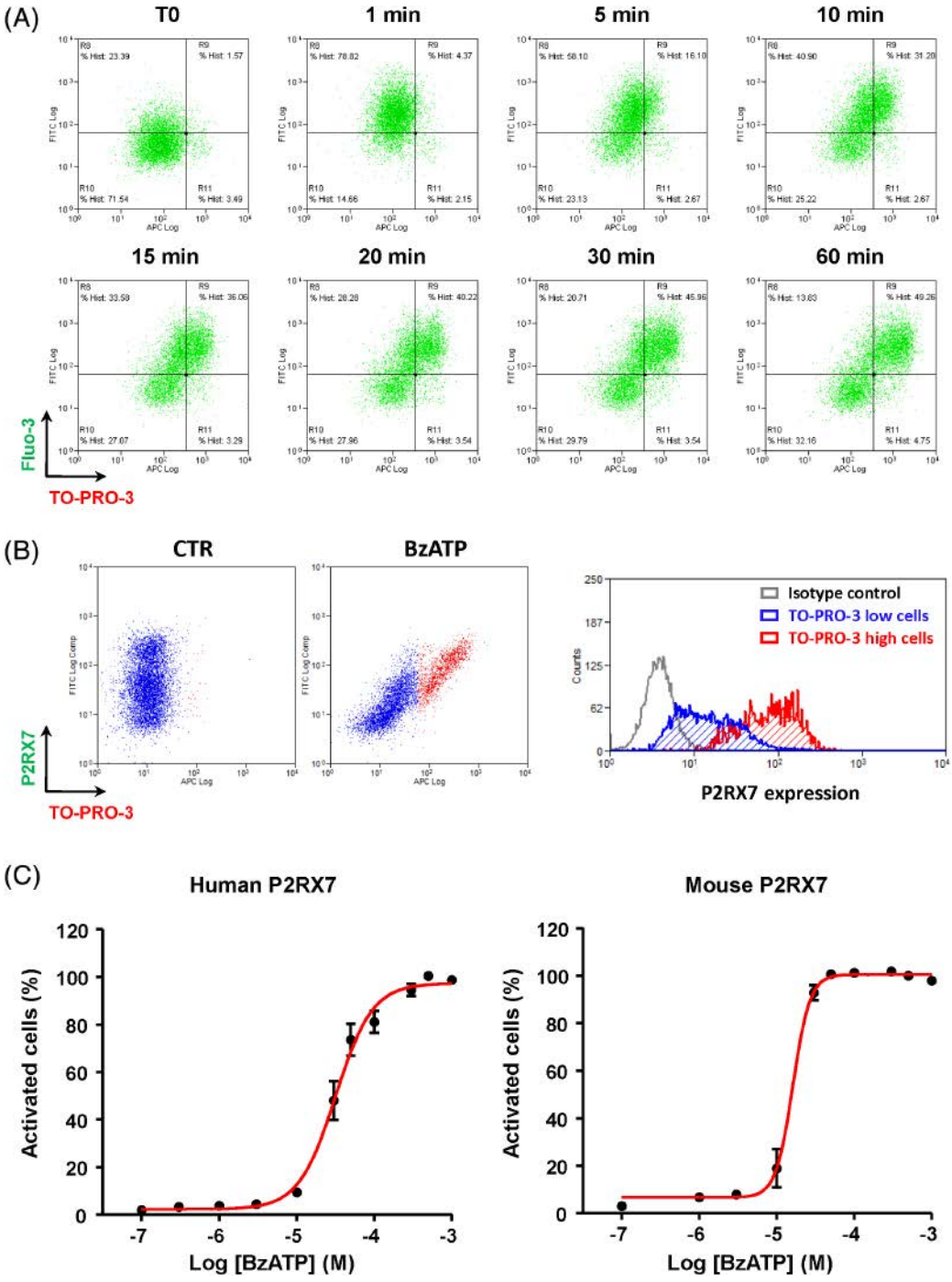

FIGURE 3 The kinetics of P2RX7 cation channel and large pore activities. (A) HEK-293 cells overexpressing human P2RX7 were stained with the calcium indicator Fluo-3 AM and then incubated with the nonpermeant DNA-intercalating dyes TO-PRO-3 (large pore opening) and propidium iodide (cell viability) before addition of the P2RX7 agonist BzATP (100 μM). The cells were then analysed at different time points using flow cytometry (with the CyAn cytometer). Two-parameter plots of Fluo-3 AM versus TO-PRO-3 fluorescence were created with Summit software. (B) HEK-293 cells overexpressing human P2RX7 were stained with anti-P2RX7 antibodies and incubated with TO-PRO-3 in the absence (CTR) or presence of BzATP (100 μM) for 1 h. The cells were then analysed using flow cytometry (with the CyAn cytometer). Two-parameter plots of P2RX7 expression versus TO-PRO-3 fluorescence (left panel) were created with Summit software. Overlays of P2RX7 staining in TO-PRO-3 low (blue) and TO-PRO-3 high (red) cells in the presence of BzATP are represented in the right panel. The results are representative of three independent experiments. (C) HEK-293 cells overexpressing human P2RX7 (left panel) and mouse P2RX7 (right panel) were stained with Fluo-3 AM and then incubated with TO-PRO-3 before addition of increasing concentrations of BzATP. The percentages of Fluo-3 AM/TO-PRO-3 double-positive cells are plotted for half maximal effective concentration (EC_{50}) calculation. The results are representative of three independent experiments [Color figure can be viewed at wileyonlinelibrary.com]

without the need for conventional compensation matrices [31]. Whereas a conventional cytometer's band-pass filters cannot distinguish between two spectrally adjacent fluorochromes, a spectral cytometer can perform a multicolor analysis with an unmixing algorithm [31,32]. Each spectrum derived from single-stained cells and the spectrum from unstained cells (autofluorescence) are considered as reference spectra for a spectral unmixing algorithm based on WLSM. Dye fluorescences from multistained samples are unmixed by the algorithm (using the spectra of unstained cells and single-stained cells as references), in order to mathematically separate and measure each fluorochrome's emission fluorescence intensity. We first determined the shape of the respective emission spectra of unstained HEK cells (autofluorescence), each individual dye, and compound B (Figure 5(A)) as references for the unmixing algorithm. The results of our spectral cytometry experiments confirmed that compound B fluorescence overlapped with Fluo-3 AM fluorescence at around 530 nm, after excitation with the 488 nm laser. However, compound B also displayed an intense fluorescence peak between 450 and 470 nm after excitation at 405 nm.

The spectra of multistained cells (Fluo-3 AM, PI and TO-PRO-3) were determined in the presence and absence of BzATP (Figure 5 (B)). BzATP induced the appearance of a Fluo-3-high cell population (indicated by the green arrow in the figure) and a TO-PRO-3 high cell population (indicated by the red arrow). After fluorescence unmixing, BzATP was found to induce the appearance of a population of small cells (arbitrarily marked in green in the figure; Supporting Information Figure S8 for FS/SS plots) that was positive for Fluo-3 AM and TO-PRO-3 (i.e., with large pore opening) (Figure 5(C)). We then assessed compound B effect on P2RX7 activity. First, we applied the unmixing algorithm for the Fluo-3 AM, TO-PRO-3 and PI fluorescence signals without considering compound B spectrum, as a comparison with conventional cytometry (Figure 5

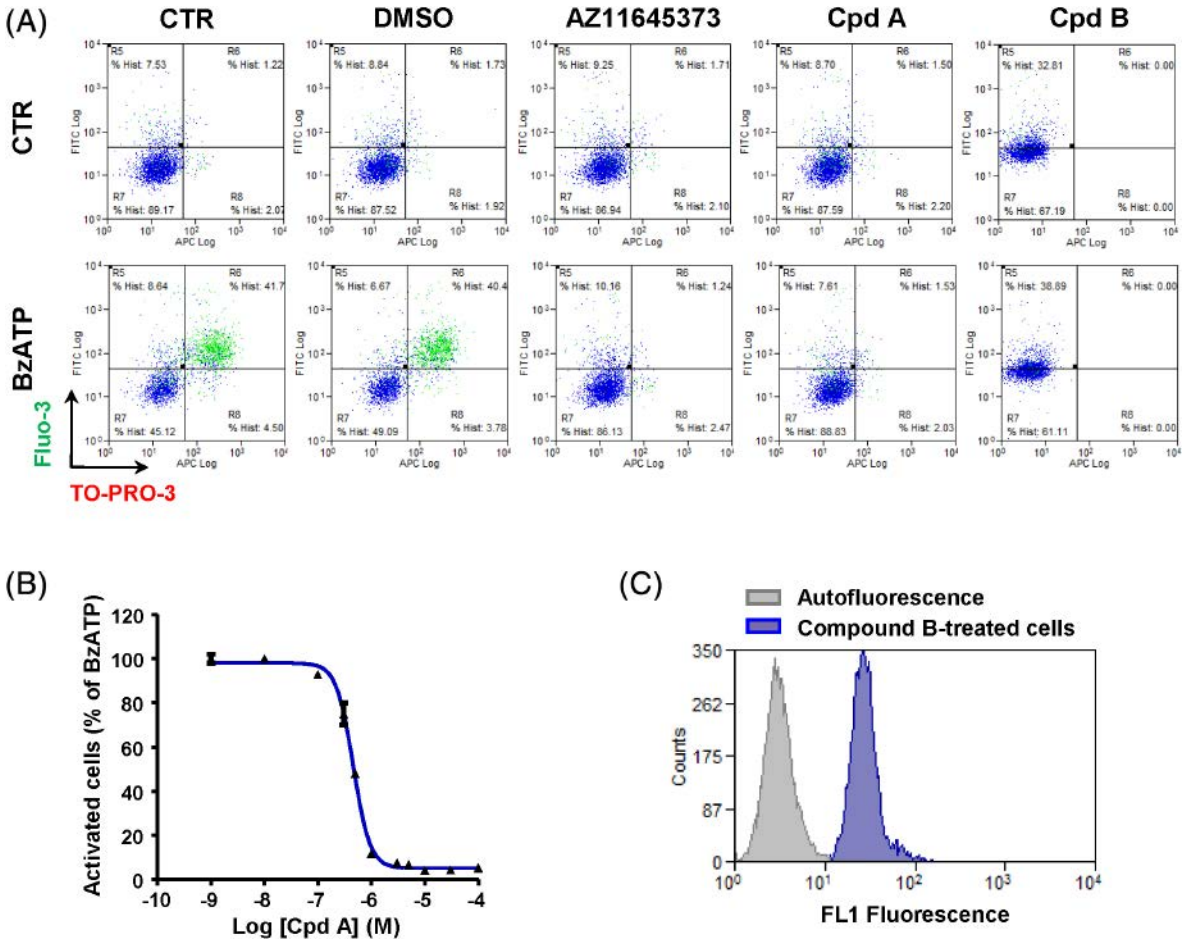

FIGURE 4 Screening of potential P2RX7 antagonists. (A) HEK-293 cells overexpressing human P2RX7 were stained with the calcium indicator Fluo-3 AM and then incubated with the non-permeant DNA-intercalating dyes TO-PRO-3 and propidium iodide in the presence of indicated molecules at 10^{-5} M for 15 min before addition of the P2RX7 agonist BzATP (100 μM) for 1 h. The cells were then analysed using flow cytometry (with the CyAn cytometer). Two-parameter plots of Fluo-3 AM versus TO-PRO-3 fluorescence were created with Summit software. (B) Percentages of Fluo-3 AM/TO-PRO-3 double-positive cells are plotted for calculation of half maximal inhibitory concentration (IC_{50}) of compound A in HEK-293 cells overexpressing human P2RX7. The results are representative of three independent experiments. (C) HEK-293 cells overexpressing human P2RX7 were incubated in the presence of compound B at 10^{-5} M for 1 h. The overlay of fluorescence intensity in FL1 band-pass filter (530 nm ± 30) of unstained cells versus compound-B-treated cells was created with Summit software [Color figure can be viewed at wileyonlinelibrary.com]

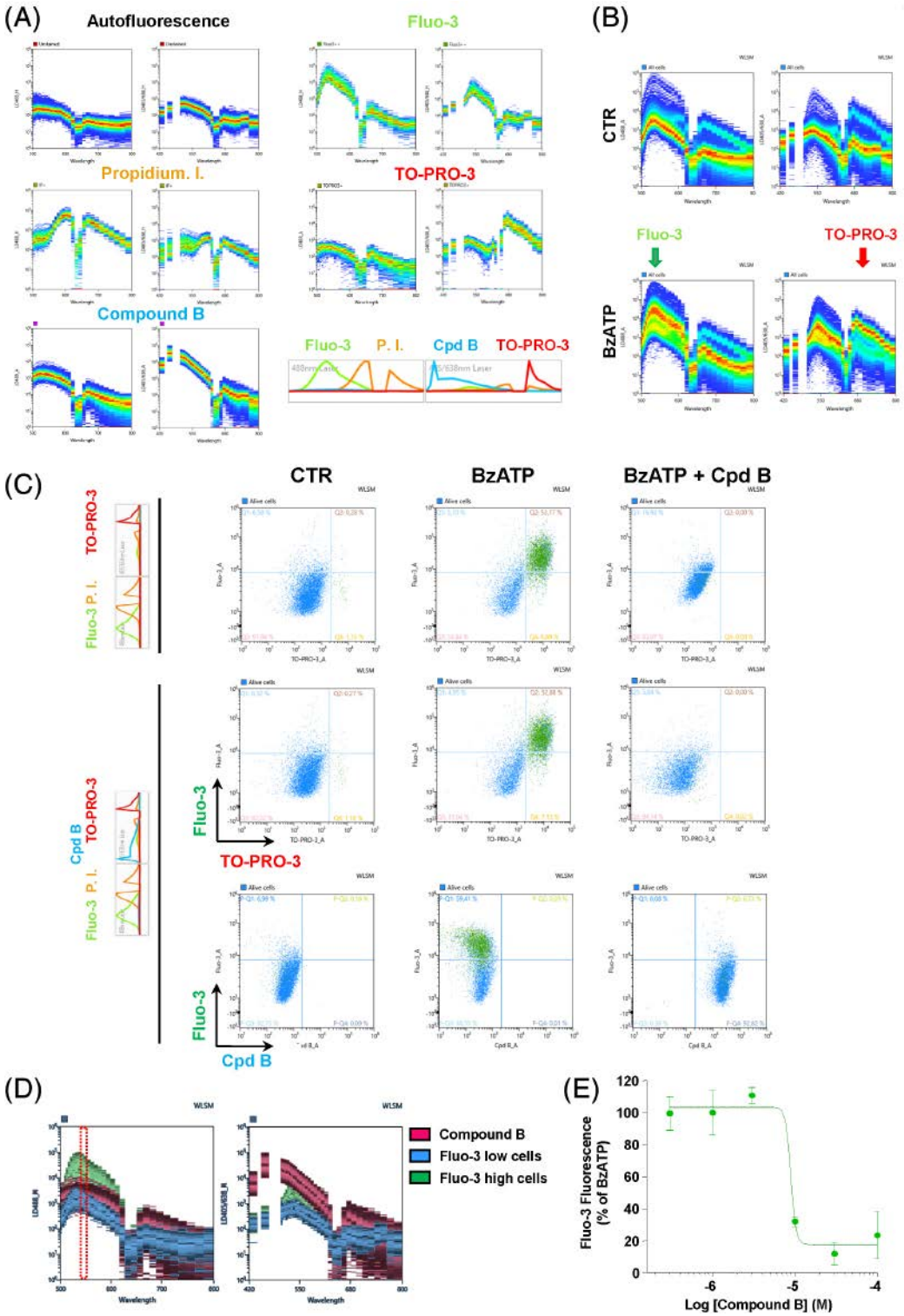

FIGURE 5 Legend on next page.

(C), upper panel). Compared with control cells, Fluo-3 AM fluorescence was elevated in the presence of compound B; this was due to spectral overlap between Fluo-3 AM and compound B (Figure 5(D)), as seen in the conventional cytometry experiments (Figure 4(A,C)). However, the addition of compound B's spectrum to the unmixing algorithm enabled us to dissociate Fluo-3 and compound B fluorescence emissions and therefore specifically detect both Fluo-3 AM and compound B (Figure 5(C), lower panels). Unmixing of compound

B's fluorescence highlighted a dose-dependent decrease in Fluo-3 AM intensity – indicating inhibition of the calcium influx by compound B (Figure 5(C,E)). Hence, in contrast to conventional flow cytometry, spectral flow cytometry takes account of a drug compound intrinsic fluorescence and enables the accurate measurement of fluorescent dyes with overlapping emission peaks. We therefore provided evidence to suggest that compound B antagonizes P2RX7 calcium channel activity (measured with Fluo-3 AM) and large pore activity (measured with TO-PRO-3).

4 | DISCUSSION

Fluorescence-based bioassays are now widely employed in the drug discovery process. The microplate assay has long been the preferred method, since it is suitable for high-throughput screening. However, microplate assay have several limitations, such as erroneous, sustained increases in fluorescence, low sensitivity (relative to fluorescence microscopy), and the lack of single-cell resolution [41]. The intrinsic fluorescence of compounds can also interfere with fluorescence-based bioassays.

Although a microplate assay can easily detect calcium influx and YO-PRO-1 uptake in HEK cells overexpressing P2RX7, flow cytometry assays are more sensitive and have greater statistical significance for the determination of large pore activity. In the present study, single-cell resolution was the prime benefit of our flow cytometry assay. Indeed, the combination of a low concentration of PI with DNA-intercalating dyes (YO-PRO-1 and TO-PRO-3) enabled us to gate out cells with a disrupted plasma membrane and thus reduce background fluorescence from accumulated DNA-intercalating dyes. This accuracy was associated with dramatically higher reproducibility, sensitivity and statistical significance. This was made possible by the absence of BzATP-induced cell death under our experimental conditions.

Although it is generally agreed that P2RX7 has a molecular weight cut-off of 900 Da, propidium (414 Da as a cation) can be used as a cell viability marker because it does not significantly permeate through the open P2RX7 pore [4,9,10]. In fact, P2RX7-mediated propidium uptake was very low at concentrations below 1 μM, in accordance with previous observations revealing human and murine lymphocytes allows ethidium but not propidium uptake [42,43]. Although PI has been already used as a fluorescent dye to study P2RX7 large pore activity, the reported experiments featured micromolar concentrations of propidium and high concentrations of BzATP [44]. Nevertheless, propidium brightness at lower concentrations made this dye a highly efficient stain for dead cells in our assay.

Our results demonstrated that the best permeant fluorescent dyes were TO-PRO-3 and YO-PRO-1. TO-PRO-3 was associated with more sensitivity—primarily because it is brighter (i.e., has a higher staining index) than YO-PRO-1. The permeation of large organic cations (such as *N*-methyl-D-glucamine) through the pore of ATP-gated P2X receptors was recently studied in molecular dynamics simulations. Entry was associated with the molecule's ability to adopt different molecular conformations and orientations, relative to the pore axis [6]. Similarly, TO-PRO-3 and YO-PRO-1 elongated molecular structures appear to facilitate pore entry. With regard to their three dimensional structures, YO-PRO-1 and TO-PRO-3 can adopt conformations with estimated maximum dimensions of 8.5 and 9 Å, respectively; by comparison, P2RX7 pore diameter may be as high as 8.5 Å [45]. Propidium's greater maximum dimension (13 Å) may explain its weak permeation through P2RX7. Hence, the fluorescent dyes' molecular size and shape appear to be more important than their molecular weight with regard to P2RX7-mediated uptake.

We combined the highly sensitive red fluorescent dye TO-PRO-3 with the calcium indicator Fluo-3 AM and the cell viability marker PI, in order to simultaneously assess P2RX7 calcium channel and large pore activities at different time points. The addition of BzATP led to rapid calcium influx (observed after 1 min), followed by a progressive

FIGURE 5 A multiparameter spectral flow cytometry analysis of P2RX7 activity. HEK-293 cells overexpressing human P2RX7 were stained with the calcium indicator Fluo-3 AM, the nonpermeant DNA-intercalating dyes TO-PRO-3 and PI before addition of compound B and/or the P2RX7 agonist BzATP (100 μM) for 1 h. The cells were then analysed by spectral flow cytometry using SP6800 (Sony Biotechnology). (A) Spectrum charts of unstained HEK-293 cells (autofluorescence) or single stained cells. The left panel is the spectrum chart of cells excited with a 488 nm laser and the right panel is the spectrum chart of cells excited with 405 and 638 nm lasers. Wavelengths from 420 nm to 800 nm are indicated in the x-axis and fluorescence intensities in the y-axis. Normalized intensity spectra of each fluorochrome used in the unmixing algorithm are indicated in the bottom right panel. (B) Spectra of the multistained HEK-293 cells (Fluo-3 AM, PI and TO-PRO-3) were determined in the absence or presence of BzATP. BzATP induced the appearance of a Fluo-3-high cell population (indicated by the green arrow) and a TO-PRO-3 high cell population (indicated by the red arrow). The unmixing algorithm determined in panel A was then applied to determine individual fluorochrome intensities (C). (C) Two-parameter plots of Fluo-3 AM versus TO-PRO-3 fluorescences of nontreated cells (CTR) or cells treated with BzATP (100 μM) with or without compound B at 10^{-5} M were created with the algorithm unmixing Fluo-3 AM, TO-PRO-3 and PI (upper panel). Two-parameter plots of Fluo-3 AM versus TO-PRO-3 and Fluo-3 AM versus compound B fluorescences of nontreated cells (CTR) or cells treated with BzATP (100 μM) with or without compound B at 10^{-5} M were created with the algorithm unmixing Fluo-3 AM, TO-PRO-3, PI and compound B (lower panels). (D) Overlay of spectrum charts of Fluo-3 AM single stained HEK-293 cells incubated in the presence of BzATP (Fluo-3 low and Fluo-3 high cells) and spectrum chart of HEK-293 cells incubated in the presence of compound B. Wavelengths from 420 nm to 800 nm are indicated in the x-axis and fluorescence intensities in the y-axis. The red dashed square represents the FL1 band-pass filter (530 nm ± 30) used in conventional cytometry. (E) Fluo-3 AM fluorescence intensities resulting from the algorithm unmixing Fluo-3 AM, TO-PRO-3, PI and compound B fluorescence, in the presence of increasing concentrations of compound B. The results are representative of three independent experiments [Color figure can be viewed at wileyonlinelibrary.com]

return to the basal level or by sustained uptake over the next hour. These transient versus sustained responses have been already observed in ATP-stimulated PC12 cells by using single-cell fluorescence microscopy; in contrast, a microplate assay only evidenced a sustained calcium increase as the average of the two types of response [41]. We found that sustained calcium influx was associated with progressive TO-PRO-3 uptake. The delay in fluorescent dye uptake (relative to rapid calcium influx) might correspond to the slower permeation of large cations through the pore and the progressive accumulation of these cations within the nucleus. Cells stained by TO-PRO-3 expressed higher membrane levels of P2RX7 than TO-PRO-3 negative cells did. A direct link between dye uptake activity and P2RX7 density has already been demonstrated in macrophages [46,47]. Pore formation may require a threshold number of agonist-occupied receptors or may be linked to P2RX7 clustering through the recruitment of additional P2RX7 subunits [4,9].

Double staining with Fluo-3 AM and TO-PRO-3 is a very efficient method for screening of P2RX7 modulators. It can be performed at different time points, in order to study early and late events. It can be useful for screening compounds before patch-clamp electrophysiology, more appropriate to study rapid events, on the second time scale, at the membrane level. Agonist and antagonist potencies (EC_{50} and IC_{50}) can also be accurately evaluated. Moreover, typical changes in cell morphology—such as cell shrinkage, increased granulosity, and (using imaging flow cytometry) membrane blebbing—are clearly apparent.

The intrinsic fluorescence of new chemical entities complicates the development of fluorescence-based bioassays [48], as evidenced by compound B's biological activity in conventional assays. We took advantage of the recently developed spectral cytometer to efficiently discriminate between fluorochromes with overlapping emission peaks. Spectral cytometry considered the cells' autofluorescence and compound B fluorescence as independent signals, as it does for other fluorescent probes. It was therefore possible to discriminate between Fluo-3 AM staining and compound B fluorescence; in contrast to conventional cytometry, this correction highlighted compound B antagonism of P2RX7 calcium channel activity.

Flow cytometry is an efficient tool for low- to medium-throughput screening of P2RX7 modulators, and spectral cytometry can be used to screen fluorescent compounds. Hence, this method has allowed the screening of several hundred compounds, the discovery of several P2RX7 antagonists (some of which have *in vivo* efficacy in an animal model of inflammatory bowel disease [49,50], and an analysis of the biological activity of cancer-related P2RX7 isoforms [51]. Spectral cytometry is a valuable new analytical tool for the fluorescence-based screening of drug candidates. It can potentially be adapted to all types of bioassay—irrespective of the fluorescence produced by the probes and/or the test compounds—and thus opens up new perspectives in drug discovery.

ACKNOWLEDGMENTS

The authors thank Claire Devos, Manon Devos, Laura Creusot, Audrey Vinchent, Betsy Crapet, Ludivine Lapèze, Jennifer Bultez and Yoan Laforgue for technical assistance during the compound screening process. The authors thank Emilie Floquet from Bio Imaging Center Lille Nord-de-France Flow Cytometry Core Facility for technical assistance. The authors gratefully thank Cédric Ait Mansour and Nicolas Montcuquet from Sony Biotechnology for fruitful discussions. The authors thank chemists from Hautes Etudes d'Ingénieur (HEI) (Germain Homerin, Davy Baudelet, Benoît Rigo, Alina Ghinet and Philippe Gautret) and from Institut de Chimie Pharmaceutique Albert Lespagnol (Lucas Lemaire and Frédérique Klupsch) for the synthesis of new chemical entities, Christophe Furman and Guillaume Ragé (binding core facility of the University of Lille) for complementary binding experiments, and Philippe Chavatte (molecular modelling core facility of the University of Lille). The authors thank David Fraser PhD (Biotech Communication SARL, Ploudalmézeau, France) for copy-editing assistance. The authors thank Institut National du Cancer (INCA), Institut National de la Santé et de la Recherche Médicale (INSERM), Centre National de la Recherche Scientifique (CNRS) and the University of Lille for financial support.

AUTHOR CONTRIBUTIONS

Amélie Barczyk: Data curation; formal analysis; methodology; writing-review and editing. **Hélène Bauderlique-Le Roy:** Data curation; formal analysis; methodology. **Nathalie Jouy:** Data curation; formal analysis; methodology. **Nicolas Renault:** Data curation; formal analysis; software. **Audrey Hottin:** Resources. **Régis Millet:** Funding acquisition; project administration; resources; writing-review and editing. **Valérie Vouret-Craviari:** Conceptualization; funding acquisition; project administration; writing-review and editing. **Sahil Adriouch:** Conceptualization; funding acquisition; project administration; resources; writing-review and editing. **Thierry Idziorek:** Resources; validation; writing-review and editing. **Xavier Dezitter:** Conceptualization; data curation; formal analysis; methodology; supervision; writing-original draft; writing-review and editing.

CONFLICT OF INTEREST

The authors declare no conflict of interest.

ORCID

Xavier Dezitter https://orcid.org/0000-0001-6932-6947

REFERENCES

1. Burnstock G, Knight GE. The potential of P2X7 receptors as a therapeutic target, including inflammation and tumour progression. *Purinergic Signal*. 2018;14:1–18.
2. Pelegrin P. Many ways to dilate the P2X7 receptor pore. *Br J Pharmacol*. 2011;163:908–11.
3. Alves LA, Melo Reis RA, de Souza CA, de Freitas MS, Teixeira PC, Neto Moreira FD, et al. The P2X7 receptor: shifting from a low- to a high-conductance channel - an enigmatic phenomenon? *Biochimica et Biophysica Acta*. 2014;1838:2578–87.
4. Di Virgilio F, Schmalzing G, Markwardt F. The elusive P2X7 macropore. *Trends in Cell Biology*. 2018;28:392–404.
5. Pelegrin P, Surprenant A. Pannexin-1 mediates large pore formation and interleukin-1beta release by the ATP-gated P2X7 receptor. *EMBO J*. 2006;25:5071–82.

6. Harkat M, Peverini L, Cerdan AH, Dunning K, Beudez J, Martz A, et al. On the permeation of large organic cations through the pore of ATP-gated P2X receptors. *Proc Natl Acad Sci USA*. 2017;114:E3786–95.
7. Pippel A, Stolz M, Woltersdorf R, Kless A, Schmalzing G, Markwardt F. Localization of the gate and selectivity filter of the full-length P2X7 receptor. *Proc Natl Acad Sci USA*. 2017;114:E2156–65.
8. Li M, Toombes GE, Silberberg SD, Swartz KJ. Physical basis of apparent pore dilation of ATP-activated P2X receptor channels. *Nat Neurosci*. 2015;18:1577–83.
9. Di Virgilio F, Giuliani AL, Vultaggio-Poma V, Falzoni S, Sarti AC. Non-nucleotide agonists triggering P2X7 receptor activation and pore formation. *Front Pharmacol*. 2018;9:39.
10. Peverini L, Beudez J, Dunning K, Chataigneau T, Grutter T. New insights into permeation of large cations through ATP-gated P2X receptors. *Front Mol Neurosci*. 2018;11:265.
11. Pelegrin P, Surprenant A. The P2X(7) receptor-pannexin connection to dye uptake and IL-1beta release. *Purinergic Signal*. 2009;5:129–37.
12. Adinolfi E, Giuliani AL, De Marchi E, Pegoraro A, Orioli E, Di Virgilio F. The P2X7 receptor: a main player in inflammation. *Biochemical Pharmacol*. 2018;151:234–44.
13. Di Virgilio F, Chiozzi P, Falzoni S, Ferrari D, Sanz JM, Venketaraman V, et al. Cytolytic P2X purinoceptors. *Cell Death Differ*. 1998;5:191–9.
14. Di Virgilio F. Purines, purinergic receptors, and cancer. *Cancer Res*. 2012;72:5441–7.
15. Benzaquen J, Heeke S, Janho Dit HS, Douguet L, Marquette CH, Hofman P, et al. Alternative splicing of P2RX7 pre-messenger RNA in health and diseases: Myth or reality? *Biomed J*. 2019;42:141–54.
16. Ulrich H, Ratajczak MZ, Schneider G, Adinolfi E, Orioli E, Ferrazoli EG, et al. Purine signaling contributes to neuroblastoma metastasis. *Front Pharmacol*. 2018;9:500.
17. Arnaud-Sampaio VF, Rabelo ILA, Ulrich H, Lameu C. The P2X7 receptor in the maintenance of cancer stem cells, chemoresistance and metastasis. *Stem Cell Rev Rep*. 2020;16:288–300.
18. Adinolfi E, Raffaghello L, Giuliani AL, Cavazzini L, Capece M, Chiozzi P, et al. Expression of P2X7 receptor increases in vivo tumor growth. *Cancer Res*. 2012;72:2957–69.
19. Adinolfi E, Capece M, Franceschini A, Falzoni S, Giuliani AL, Rotondo A, et al. Accelerated tumor progression in mice lacking the ATP receptor P2X7. *Cancer Research*. 2015;75:635–44.
20. Ghiringhelli F, Apetoh L, Tesniere A, Aymeric L, Ma Y, Ortiz C, et al. Activation of the NLRP3 inflammasome in dendritic cells induces IL-1beta-dependent adaptive immunity against tumors. *Nat Med*. 2009;15:1170–8.
21. Hofman P, Cherfils-Vicini J, Bazin M, Ilie M, Juhel T, Hebuterne X, et al. Genetic and pharmacological inactivation of the purinergic P2RX7 receptor dampens inflammation but increases tumor incidence in a mouse model of colitis-associated cancer. *Cancer Res*. 2015;75:835–45.
22. Di Virgilio F. P2RX7: a receptor with a split personality in inflammation and cancer. *Mol Cell Oncol*. 2016;3:e1010937.
23. Baudelet D, Lipka E, Millet R, Ghinet A. Involvement of the P2X7 purinergic receptor in inflammation: an update of antagonists series since 2009 and their promising therapeutic potential. *Curr Med Chem*. 2015;22:713–29.
24. Koch-Nolte F, Eichhoff A, Pinto-Espinoza C, Schwarz N, Schafer T, Menzel S, et al. Novel biologics targeting the P2X7 ion channel. *Curr Opin Pharmacol*. 2019;47:110–8.
25. Jursik C, Sluyter R, Georgiou JG, Fuller SJ, Wiley JS, Gu BJ. A quantitative method for routine measurement of cell surface P2X7 receptor function in leucocyte subsets by two-colour time-resolved flow cytometry. *J Immunol Methods*. 2007;325:67–77.
26. Korpi-Steiner NL, Sheerar D, Puffer EB, Urben C, Boyd J, Guadarrama A, et al. Standardized method to minimize variability in a functional P2X(7) flow cytometric assay for a multi-center clinical trial. *Cytom B Clin Cytom*. 2008;74:319–29.
27. Adriouch S, Dox C, Welge V, Seman M, Koch-Nolte F, Haag F. Cutting edge: a natural P451L mutation in the cytoplasmic domain impairs the function of the mouse P2X7 receptor. *J Immunol*. 2002;169:4108–12.
28. Adriouch S, Scheuplein F, Bähring R, Seman M, Boyer O, Koch-Nolte F, et al. Characterisation of the R276A gain-of-function mutation in the ectodomain of murine P2X7. *Purinergic Signal*. 2009;5:151–61.
29. Adriouch S, Dubberke G, Diessenbacher P, Rassendren F, Seman M, Haag F, et al. Probing the expression and function of the P2X7 purinoceptor with antibodies raised by genetic immunization. *Cell Immunol*. 2005;236:72–7.
30. Maecker HT, Frey T, Nomura LE, Trotter J. Selecting fluorochrome conjugates for maximum sensitivity. *Cytom Part A*. 2004;62:169–73.
31. Futamura K, Sekino M, Hata A, Ikebuchi R, Nakanishi Y, Egawa G, et al. Novel full-spectral flow cytometry with multiple spectrally-adjacent fluorescent proteins and fluorochromes and visualization of in vivo cellular movement. *Cytom Part A*. 2015;87:830–42.
32. Schmutz S, Valente M, Cumano A, Novault S. Spectral cytometry has unique properties allowing multicolor analysis of cell suspensions isolated from solid tissues. *PLoS One*. 2016;11:e0159961.
33. Buell G, Chessell IP, Michel AD, Collo G, Salazzo M, Herren S, et al. Blockade of human P2X7 receptor function with a monoclonal antibody. *Blood*. 1998;92:3521–8.
34. Sander T, Freyss J, von Korff M, Rufener C. DataWarrior: an open-source program for chemistry aware data visualization and analysis. *J Chem Inf Model*. 2015;55:460–73.
35. Pettersen EF, Goddard TD, Huang CC, Couch GS, Greenblatt DM, Meng EC, et al. UCSF chimera--a visualization system for exploratory research and analysis. *J Comput Chem*. 2004;25:1605–12.
36. Michel AD, Kaur R, Chessell IP, Humphrey PP. Antagonist effects on human P2X(7) receptor-mediated cellular accumulation of YO-PRO-1. *Br J Pharmacol*. 2000;130:513–20.
37. Hibell AD, Thompson KM, Xing M, Humphrey PP, Michel AD. Complexities of measuring antagonist potency at P2X(7) receptor orthologs. *J Pharmacol Exp Ther*. 2001;296:947–57.
38. Bortner CD, Hughes FM, Cidlowski JA. A primary role for K+ and Na+ efflux in the activation of apoptosis. *J Biol Chem*. 1997;272:32436–42.
39. Donnelly-Roberts DL, Namovic MT, Han P, Jarvis MF. Mammalian P2X7 receptor pharmacology: comparison of recombinant mouse, rat and human P2X7 receptors. *Br J Pharmacol*. 2009;157:1203–14.
40. Stokes L, Jiang LH, Alcaraz L, Bent J, Bowers K, Fagura M, et al. Characterization of a selective and potent antagonist of human P2X (7) receptors, AZ11645373. *Br J Pharmacol*. 2006;149:880–7.
41. Heusinkveld HJ, Westerink RH. Caveats and limitations of plate reader-based high-throughput kinetic measurements of intracellular calcium levels. *Toxicol Appl Pharmacol*. 2011;255:1–8.
42. Wiley JS, Chen R, Jamieson GP. The ATP4- receptor-Operated Channel (P2Z class) of human lymphocytes allows Ba2+ and ethidium+ uptake: inhibition of fluxes by Suramin. *Archiv Biochem Biophys*. 1993;305:54–60.
43. Chused TM, Apasov S, Sitkovsky M, Murine T. Lymphocytes modulate activity of an ATP-activated P2Z-type purinoceptor during differentiation. *J Immunol*. 1996;157:1371–80.
44. Sun C, Heid ME, Keyel PA, Salter RD. The second transmembrane domain of P2X7 contributes to dilated pore formation. *PLoS One*. 2013;8:e61886.
45. Riedel T, Schmalzing G, Markwardt F. Influence of extracellular monovalent cations on pore and gating properties of P2X7 receptor-operated single-channel currents. *Biophys J*. 2007;93:846–58.
46. Gudipaty L, Humphreys BD, Buell G, Dubyak GR. Regulation of P2X (7) nucleotide receptor function in human monocytes by extracellular

ions and receptor density. *Am J Physiol Cell Physiol*. 2001;280: C943–53.
47. Humphreys BD, Dubyak GR. Modulation of P2X7 nucleotide receptor expression by pro- and anti-inflammatory stimuli in THP-1 monocytes. *J Leukoc Biol*. 1998;64:265–73.
48. Simeonov A, Davis MI. Interference with fluorescence and absorbance. *Assay guidance manual [Internet]*. Bethesda, MD: Eli Lilly & Company and the National Center for Advancing Translational Sciences; 2004.
49. Homerin G, Lipka E, Rigo B, Millet R, Dezitter X, Furman C, et al. Discovery of highly functionalized scaffolds: pyrroloimidazolediones as P2X7 receptor antagonists. *Tetrahedron*. 2017;73:5327–36.
50. Homerin G, Jawhara S, Dezitter X, Baudelet D, Dufrénoy P, Rigo B, et al. Pyroglutamide-based P2X7 receptor antagonists targeting inflammatory bowel disease. *J Med Chem*. 2020;63: 2074–94.
51. Benzaquen J, Dit Hreich SJ, Heeke S, Juhel T, Lalvee S, Bauwens S, et al. P2RX7B is a new theranostic marker for lung adenocarcinoma patients. *Theranostics*. 2020;10:10849–60.

SUPPORTING INFORMATION

Additional supporting information may be found online in the Supporting Information section at the end of this article.

How to cite this article: Barczyk A, Bauderlique-Le Roy H, Jouy N, et al. Flow cytometry: An accurate tool for screening P2RX7 modulators. *Cytometry*. 2021;99:793–806. https://doi.org/10.1002/cyto.a.24287